**Title**
A MEMS Thin Film AlN Supercritical Carbon Dioxide Valve

**Author**
Chen, Ya-Mei

**Publication Date**
2011

# A MEMS Thin Film AlN Supercritical Carbon Dioxide Valve

By

Ya-Mei Chen

A dissertation submitted in partial satisfaction of the

requirements for the degree of

Doctor of Philosophy

in

Engineering - Mechanical Engineering

in the

Graduate Division

of the

University of California, Berkeley

Committee in charge:

Professor Albet Pisano, Chair
Professor Liwei Lin
Professor Tsu-Jae King Liu
Professor Tarek Zohdi

Spring 2011

A MEMS Thin Film AlN Supercritical Carbon Dioxide Valve

Ya-Mei Chen

# Abstrat

# A MEMS Thin Film AlN Supercritical Carbon Dioxide Valve

by

Ya-Mei Chen

Doctorate of Philosophy in Engineering – Mechanical Engineering

Univeristy of California, Berkeley

Professor Albert Pisano, Chair

In this thesis, a new piezoelectric valve system with bi-chevron aluminum nitride (AlN) actuator is described. The intended application of the new piezoelectric valve is for the advanced printing technology with supercritical carbon dioxide as the solvent. With supercritical carbon dioxide as the solvent, the ink dissolved will start to nucleate with a micronozzle and generate extremely small and uniform ink particles due to rapid expansion of supercritical solution (RESS). Therefore, the resolution of the printing can be improved and induce a much better printing quality.

To successfully operate this new printing technology, the operation pressure of this valve system should be as high as 30 MPa. This operation pressure is much higher than what the current piezoelectric MEMS valve can offer. Aluminum nitride is chosen as the piezoelectric material over lead zirconate titanate (PZT) because the depolarization of PZT due to compressive stresses limits the operating pressure to less than 5 MPa. In order to meet high pressure requirements, thin-film AlN is selected because it doesn't experience compressive stress depolarization and is IC compatible. The piezoelectric valve system is designed with bi-chevron shape not only to amplify the generated stroke but also to reduce undesired out-of-plane motion. This amplification mechanism is achieved by the cantilever beam structure without increasing the size of the valve system significantly. In the bi-chevron, the use of piezoelectrics with matched sets of actuator arms enables a push-pull actuation in both directions and also reduces out-of-plane buckling.

To verify the working function of the bi-chevron actuator, a pre-prototype device is introduced and fabricated. And the result from the static testing of the pre-prototype device is compared with the finite element simulation and the theoretical analysis. The result shows a good fitting between finite element simulation and the pre-prototype device measurement (maximum error is about 17%). However, the error between the theoretical analysis and finite element simulation is significant due to the particle top/bottom electrode coverage. This is because partial-coverage results in a nonuniform electrical field along the width of the AlN beam and simultaneously reduces the generated stroke and the generated force. For the dynamic performance, an alternating current (AC) is used to actuate the pre-prototype device rather than direct current (DC). It is because AC actuating voltage gives the dynamic response of the

pre-prototype device and then indicates the resonant frequency of the pre-prototype devices which corresponds to the operation speed while DC actuating voltage has no effect on the dynamic performance at all. The result of the dynamic performance shows that the prototype device will give 1.5 µm in-plane generated stroke with acceptable out-of-plane generated stroke when the device is actuated in 60 kHz with 10 V actuating voltage. The pre-prototype device has 1100 µm long, 10 µm wide, and 2° angle AlN beams.

In addition to the pre-prototype device, the prototype device is fabricated for the supercritical carbon dioxide valve system. The difference between prototype devices and supercritical carbon dioxide devices is that supercritical carbon dioxide devices have been sealed with a cap. That means the prototype devices can become goal devices, supercritical carbon dioxide valves, after sealing the device with a cap. This prototype device uses a SOI wafer with bi-chevron AlN actuator to control the flow of the supercritical carbon dioxide valve. This is prototype device is also evaluated and the result verify that this fabrication process is correct.

# Dedication

To my family who really support me while I am facing any difficulty.

# Table of Contents

# List of Figures

# List of Tables

# Nomenclature

| | |
|---|---|
| $\Delta T$ | Elongation or shrink in the thickness direction and this thickness direction is the same direction as the polarization of the piezoelectric material |
| $\Delta L$ | Elongation or shrink in the length direction when the thickness direction is the same direction as the polarization of the piezoelectric material |
| $\Delta W$ | Elongation or shrink in the width direction when the thickness direction is the same direction as the polarization of the piezoelectric material |
| $\Delta X$ | Relative movement of two corners due to the shear deformation when the thickness direction is the same direction as the polarization of the piezoelectric material |
| T | Original thickness of the piezoelectric material |
| L | Original length of the piezoelectric material |
| W | Original width of the piezoelectric material |
| $d_{31}$ | A element of the piezoelectric strain matrix that represents the influence the applied electric field in the polarization/thickness direction on the normal strain change in the width and length direction |
| $d_{33}$ | A element of the piezoelectric strain matrix that represents the influence the applied electric field in the polarization/thickness direction on the normal strain change in the thickness direction |
| $d_{51}$ | A element of the piezoelectric strain matrix that represents the influence the applied electric field in the polarization/thickness direction on the shear strain change |
| V | Applied voltage on the piezoelectric material |
| $\Delta y$ | Generated stroke with the stroke amplified mechanism for a piezoelectric actuator |
| $E_3$ | Applied electrical field in the thickness direction when the thickness direction is the same direction as the polarization of the piezoelectric material |
| F | Force is generated in the piezoelectric material due to applied electric field when the thickness direction is the same direction as the polarization of the piezoelectric material |
| P | Generated force of a piezoelectric actuator that is transformed to the moving direction because of the amplification mechanism. |
| A | Cross section of the piezoelectric material |
| $S_{11}$ | Stress on the cross section of the piezoelectric material |
| $e_{31}$. | A element of the piezoelectric stress matrix that represents the influence the applied electric field in the polarization/thickness direction on the normal strain change in the width and |

|  |  |
|---|---|
|  | length direction |
| $E_B$ | Break down electric field of the piezoelectric material |
| $\Delta y/L$ | Normalized generated stroke of the piezoelectric actuator |
| $P/F$ | Normalized generated force of the piezoelectric actuator |
| $f$ | 1st in plane resonant frequency in solid mechanics |
| $E$ | Young’s modulus of object |
| $\rho$ | Density of the object |
| $I$ | Moment of the inertia of the object |
| $\pi$ | A mathematical constant whose value is the ratio of any Euclidean plane circle's circumference to its diameter |
| $\Delta G$ | Movement of the device calculated from Vernier Scale |
| $\Delta d_1$ | Gap between the electrodes for the fixed end in the Vernier Scale |
| $\Delta d_2$ | Gap between the electrodes for the free end in the Vernier Scale |
| $N$ | Number of the aligned electrode after movement |
| $M$ | Number of the aligned electrode before movement |
| $W'$ | Width of the actual piezoelectric device due to the applied electric field |
| $F'$ | Beam force of the actual piezoelectric device due to applied electric field |
| $\Delta L'$ | Elongation of the actual piezoelectric device due to applied electric field |
| $f_d$ | Frequency shift due to Doppler effect |
| $V_{object}$ | Velocity of an object |
| $\lambda$ | Wavelength of laser light |
| $f_o$ | Frequency of the light coming from the laser source |
| $S_{object}$ | Displacement of an object |

# Chapter 1 Introduction

The long term goal of this research is to develop a microfabricated valve to control to control the flow of supercritical carbon dioxide that is used in an advanced printing. In this chapter, the background of this research will be discussed, including the overview, motivation, and achievements. First, we will talk about the new supercritical carbon dioxide valve design. In this part, the uniqueness and goal of this new supercritical carbon dioxide will be discussed. Second, we will move to the motivation of this research and discuss the advantages of supercritical carbon dioxide printing technology. In the end, the achievement of this project will be summarized and discussed.

## 1.1 Overview: Supercritical Carbon Dioxide Valve

A supercritical carbon dioxide valve system for supercritical carbon dioxide printing technology is introduced and developed in this research (as shown in Fig. 1). To successfully operate the carbon dioxide flow in supercritical state, this new valve system is designed to work against pressures as high as 30MPa. Compared with other types of microvalves, this supercritical carbon dioxide is designed to be actuated piezoelectrically because of excellent typical characteristics of piezoelectric microvalves: high operation pressure, high temperature stability, high operation frequency, wide range operation temperature, and low power consumption.

The highest operation pressure of current piezoelectric microvalve design is limited by compressive stress depolarization that happens to lead zirconate titanate ($Pb[Zr_xTi_{1-x}]O_3$, $0 \leq x \leq 1$) when it is operating under high pressure. To really achieve high operation pressure, aluminum nitride (AlN) is introduced to the supercritical carbon dioxide valve system since AlN doesn't exhibit compressive stress depolarization. With AlN as the piezoelectric material for the supercritical carbon dioxide, we also can achieve higher operation pressure, higher temperature stability, and IC compatible at the same.

Beyond the to usage of a new piezoelectric material for the supercritical carbon dioxide valve, a new actuator design, bi-chevron actuator, is introduced to achieve the open/close mechanism of the valve system. This bi-chevron actuator design uses vertically and horizontally symmetric AlN beams to reduce the undesired out-of-plane motion and then have better control on the fluid to avoid the block problem. The bi-chevron actuator design actuating bi-directionally and can amplify the generated piezoelectric stroke internally with the cantilever beam structure so as to achieve large valve plug motion. Compared with external stroke amplification mechanism, the size of the supercritical carbon dioxide valve with this internal stroke amplification mechanism (bi-chevron AlN actuator design) can be achieve small volume and there in compatible with printing technology.

A model of the electro-mechanical performance of the valve was derived from first principles. In addition, this theoretical analysis was compared to results derived from finite element simulation, ANSYS. The influence of the geometry of the devices on the performance is evaluated statically and dynamically to seek for a deep understanding of the system and a further optimization of the system.

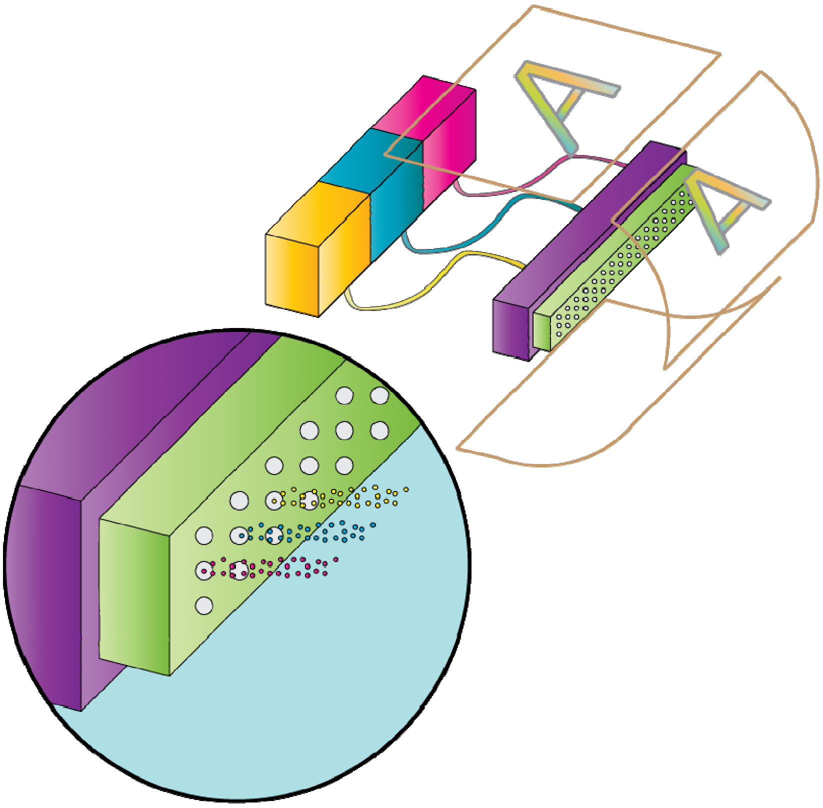

Fig. 1. Sketch of supercritical carbon dioxide printing technology.

In this research, to realize this supercritical carbon dioxide design, a new fabrication process is developed with semiconductor fabrication process. Devices from this new fabrication process have been tested with experiment setups to verify the static performance and dynamic performance. And the results of the devices measurement will be compared with theoretical analysis and finite element simulation to prove our design idea.

## 1.2 Motivation: Supercritical Carbon Dioxide for Advanced Printing Technology

Supercritical carbon dioxide is a fluid state of carbon-dioxide when the temperature and pressure of the carbon dioxide is higher than critical point (31.1 C and 72.9 atm). The pressure-temperature diagram for carbon-dioxide is shown in Fig. 2 and the region of supercritical carbon dioxide is labeled in this figure. When the carbon dioxide is in a supercritical state, the carbon dioxide will have liquid-like solubilities and gas-like diffusivities and viscosity. In addition, when the state of carbon dioxide is close the critical point, any small change in the temperature and pressure will cause in a large change of viscosity and density of the carbon-dioxide [1]. For many organic compounds, supercritical carbon dioxide is an excellent nonpolar solvent and can be used to replace organic solvent.

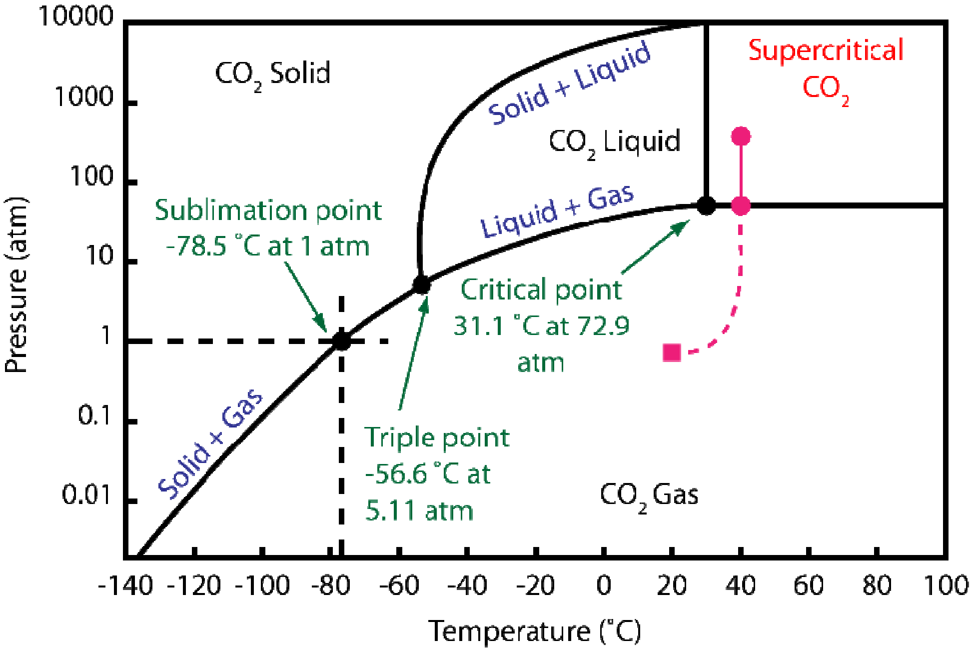

**Fig. 2. Pressure-temperature phase diagram for carbon dioxide. The red line in this figure points out the change of temperature and pressure of the supercritical carbon dioxide due to rapid expansion of supercritical carbon-dioxide when it goes through a nozzle.**

At Kodak, a new printing technology with supercritical carbon dioxide as solvent for ink has been developed. The ink dissolved in the super in the supercritical carbon dioxide will start to nucleate and generate ink particles when the fluid goes through a Rapid Expansion of Supercritical Solution (RESS) process over a nozzle (as shown in Fig. 3) [2]. In the RESS process, the pressure and the temperature of the supercritical carbon dioxide will start to drop to room temperature (27 C) and room pressure (1 atm). At that time, very high supersaturations are reached immediately and then cause the dissolved ink to nucleate with small ink particles size and narrow size distribution. The new printing technology can generate much more uniform and much smaller ink particles with RESS (as shown in Fig. 4) than can be achieved in common ink jet technologies.

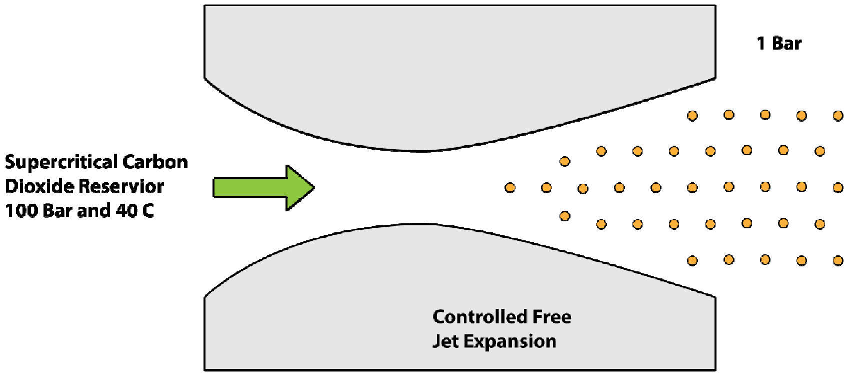

Fig. 3. Sketch of rapid expansion of supercritical solution (RESS) with a nozzle design.

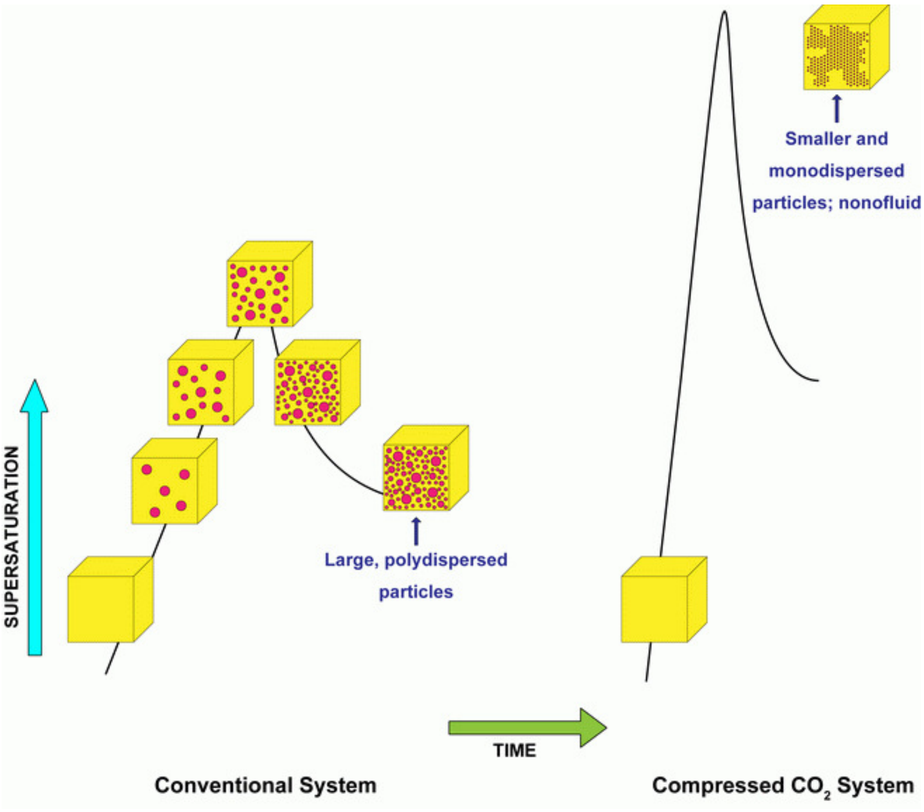

Fig. 4. Illustration of the significant difference in precipitation kinetics between traditional liquid and compressed (supercritical) fluid system [3].

In order to evaluate the quality of the ink particles, a setup as shown in Fig. 5 [4] [5] is used to generate the ink particle with RESS process. In this setup, the RESS process happens in a micronozzle since the micronozzle will replace the expansive chamber. The trace of the ink particles that are generated with this system is as shown in Fig. 6. And the experiment data shows that the ink particles generated from this new printing technology has a size that is smaller than 10 nm in diameter [4]. This size is thousand times smaller than the ink dye with 10 µm in diameter from the traditional technology (as shown in Fig. 7). With such kind of small ink particle size, the resolution of the new printing technology will be much better than the current printing technology.

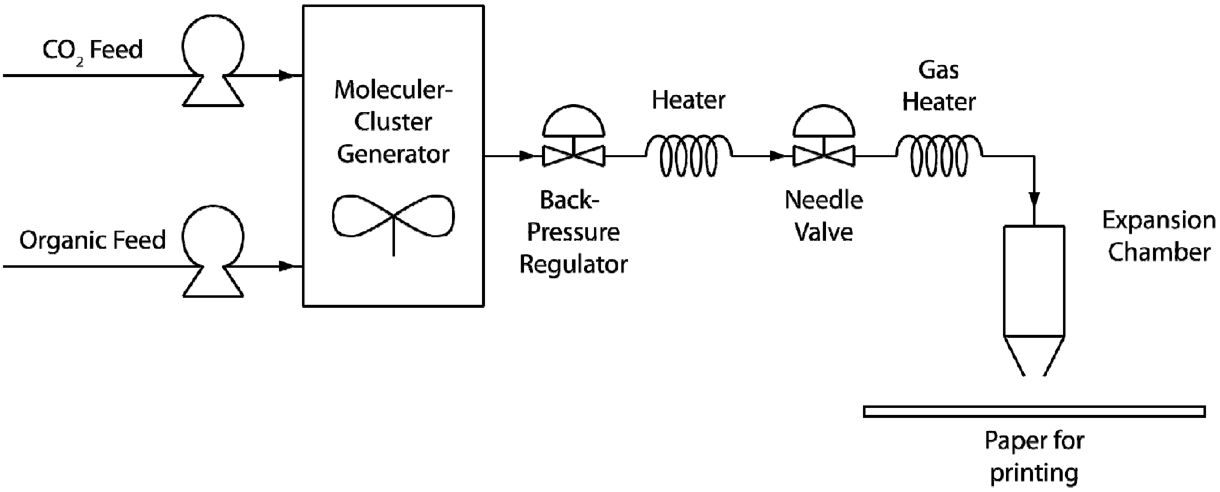

**Fig. 5. Setup of printing technology with supercritical carbon dioxide as the solvent [4].**

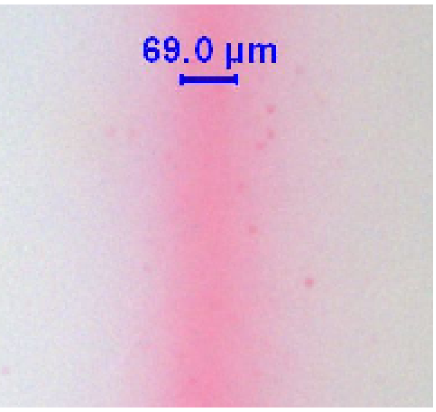

**Fig. 6. Trace of ink particles with a MEMS nozzle made by J. Heppener. These ink particles are generated by the printing system with supercritical carbon dioxide as solvent.**

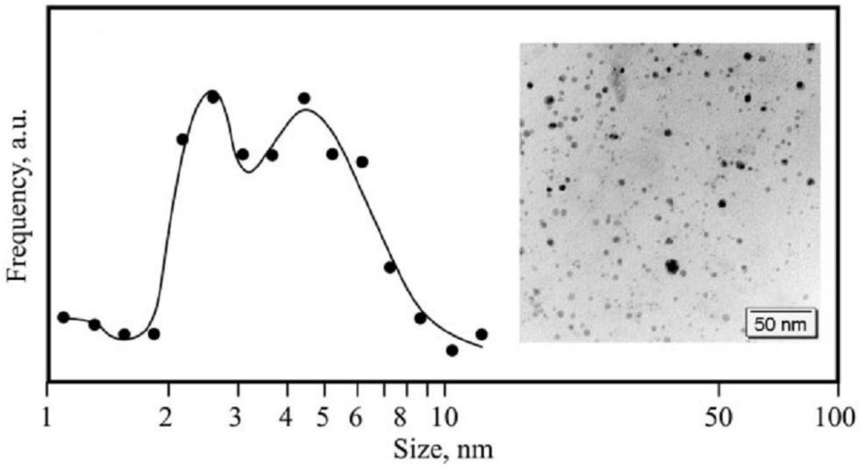

**Fig. 7. Distribution of the size of ink particles from the supercritical carbon dioxide printing technology [4].**

In addition to better resolution, there are some other advantages of this new printing technology compared with the current printing technology. The summary of the advantages of Kodak printing technology with supercritical carbon dioxide are:

1. *Cheap and easy to get*: Around 0.0039% of the atmosphere is comprised by carbon dioxide and there is no need to purchase chemicals to make the solvent for this new printing technology since we can get the material of the solvent from air. After collecting carbon dioxide from the air, it will be transformed to supercritical carbon dioxide with the supercritical extraction process. Compared with the current printing technology, this supercritical carbon dioxide is cheap and easy to get.
2. *Green solvent for ink:* In this new printing technology, supercritical carbon dioxide is used as the solvent for the ink. Carbon dioxide is nontoxic for the environment and can be considered as a green solvent compared with the solvent used in the current printing technology.
3. *Generate high density, uniform, and small ink particles and get better performance than dye ink:* When the supercritical carbon dioxide with the dissolved ink goes through a rapid expansion of supercritical solution, the dissolved ink will start to nucleate and then generate ink particles. This process is very fast and then can generate extremely small and uniform ink particles for the printer.
4. *Get dry ink and then no smudge problem*: When the supercritical carbon with the dissolved ink goes through a rapid expansion, the dissolved ink will start to nucleate and then generate ink particles. At the time, the solvent, supercritical carbon dioxide, will become carbon dioxide gas due the change of the temperature and pressure and then become part of the air after it exits the system. So only the dry ink particles will hit the printing paper and then there is no smudge problem for the printing.

## 1.3 Achievements of this thesis

In this research, a supercritical carbon dioxide valve system is introduced to the new printing technology developed by Kodak. A clear approach is developed and verified to bring the supercritical carbon dioxide vavle system to commercialization in the future. To summary, this thesis has the following achievements for the supercritical carbon dioxide valve system:

- Introduced a piezoelectric microvalve with bi-chevron AlN actuators for supercritical CO2 advanced printing technology.
- Analyzed the device with theoretical analysis and finite element simulation to evaluate the influence of geometry parameters on static and dynamic performance.
- Developed a new fabrication process to realize the design idea of the goal devices.
- Fabricated and characterized the devices and setup experiment to evaluate the static performance and dynamic performance of the devices.

The detail of the operation and characterization of supercritical carbon dioxide valve will be discussed in detail in the following sections.

# Chapter 2 Supercritical Carbon Dioxide Valve for Advanced Printing Technology

## 2.1 MEMS Valves

To apply this new supercritical carbon-dioxide into printing technology, a valve with small valve volume, low power consumption, high temperature stability, high working pressure, and high operation frequency is needed. Here, micro electromechanical system (MEMS) technology is applied for the development of supercritical carbon dioxide valve since MEMS devices have smaller volume and can be integrated with IC circuit. And it has more possibility to meet the requirements of the valve for this new printing technology. In MEMS, there are four main different microvalves (as shown in Fig. 8) [6]: electromagnetic microvalve (Fig. 8 (A)), electrostatic microvalve (Fig. 8 (B)), thermal microvalve (Fig. 8 (C)), and piezoelectric microvalve (Fig. 8 (D)). The detail of these MEMS valve will be discussed in the following.

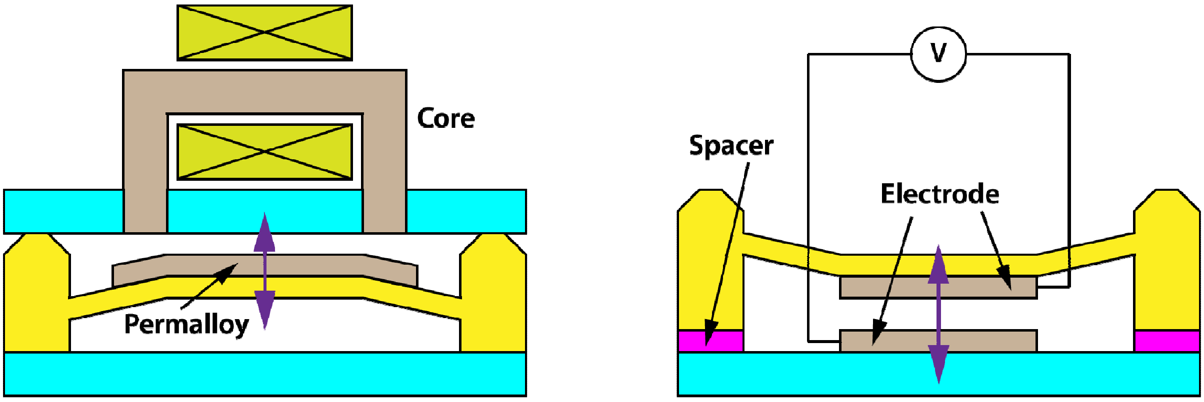

(A) Electromagnetic MEMS Valve (B) Electrostatic MEMS Valve

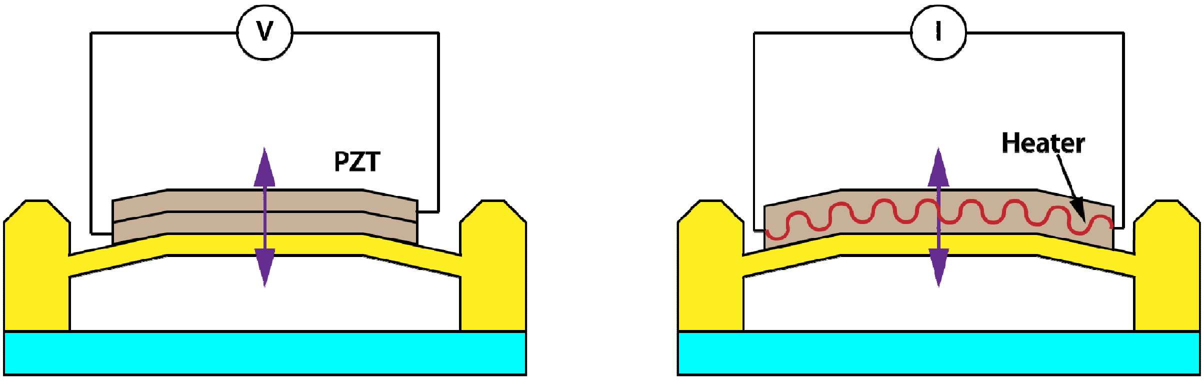

(C) Piezoelectric MEMS Valve (D) Thermal MEMS Valve

**Fig. 8. Illustrations of actuation principles of MEMS valves: (A) electromagnetic MEMS valve, (B) electrostatic MEMS valve, (C) piezoelectric MEMS valve, and (D) thermal MEMS valve.**

### 2.1.1 Electromagnetic MEMS Valve

The first MEMS electromagnetic valve is introduced by Terry *et al*. in 1979 [7]. This valve is designed for gas chromatographic (GC) air analyzer application (as shown in Fig. 9 and Fig. 10). It is a normal closed valve with a solenoid-actuated diaphragm. It consists an etched silicon seat with orifice, a nickel diaphragm, and a solenoid actuator/plunger assembly (as shown in Fig. 9). The most popular material for electromagnetic MEMS valves are NiFe [8-11]. Sadler *et al*. makes Ni/Fe and Si Membrane works together to achieve a normally closed valve. The detail of Sadler's design [10] is as shown in Fig. 11 and Fig. 12.

Electromagnetic microvalves can generate high force and large stroke with low power consumption since it is actuated by electromagnetic force. It is really good to operate under high pressure. However, its size is large compared with other kind of MEMS valve. So this large size limits its application on printing technology since smaller size of the valve system is desired in printing technology.

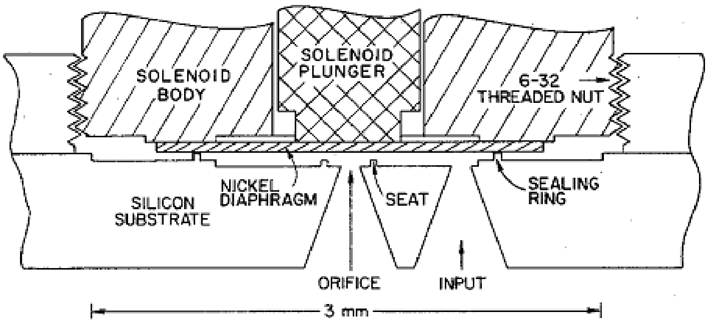

**Fig. 9. Cross section of the first MEMS electromagnetic valve. It is vertical scale is exaggerated for clarity [7].**

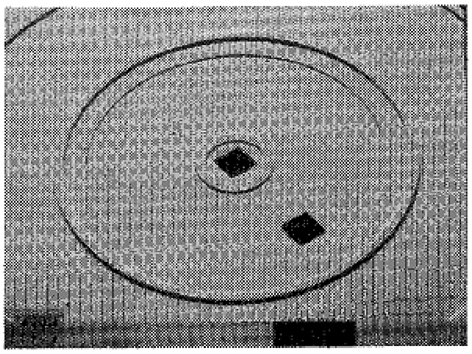

**Fig. 10. SEMS photography of etched miniature valve of the first MEMS electromagnetic valve [7].**

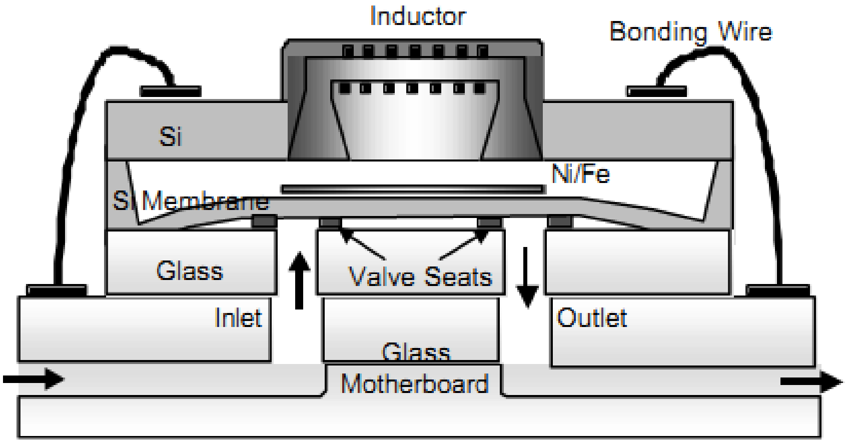

**Fig. 11. Normally closed magnetic microvalve show with both fluidic and electrical connections made to as glass motherboard [10].**

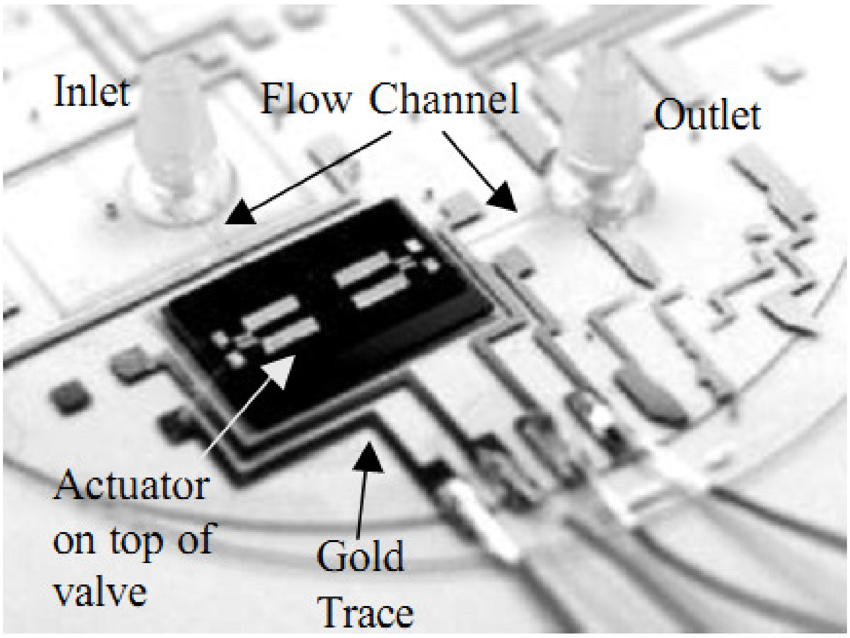

**Fig. 12. Photography of assembled microvalve by Sadler *et al*. Valves. and actuators are attached to the glass motherboard which routes electrical and fluidic connections [10].**

### 2.1.2 Electrostatic MEMS Valve

Electrostatic MEMS valve use electrostatic force to move a membrane or a rigid body to achieve the open and close function [12-21]. Electrostatic MEMS valve can operate at high frequency with low power consumption. Its volume is much smaller than an electromagnetic valve and it gives the acceptable stroke for valve application. Because of these advantages, electrostatic MEMS valves are very popular for gas flow control. Yang *et al*. introduced a design for gas fuel delivery application (as shown in Fig. 13). This work is successfully integrated with combustor, exhaust, turbine, and compressor to become a microengine (as shown in Fig. 14 and Fig. 15). However, it is rarely used to control fluid due to electrolysis of liquids at high voltage. In addition, it can’t be used for conductive fluid since conductive fluidic will influence the electric field that actuates the system.

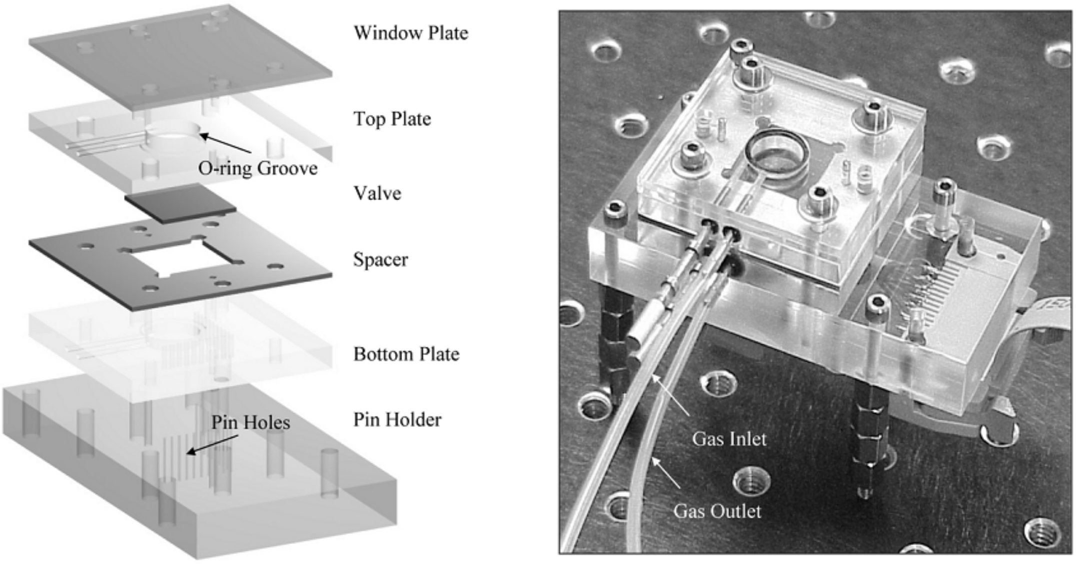

(A) Schematic assembly (B) Photography of test package

**Fig. 13. Package assembly for electrostatic microvalve testing by Yang *et al*. [20].**

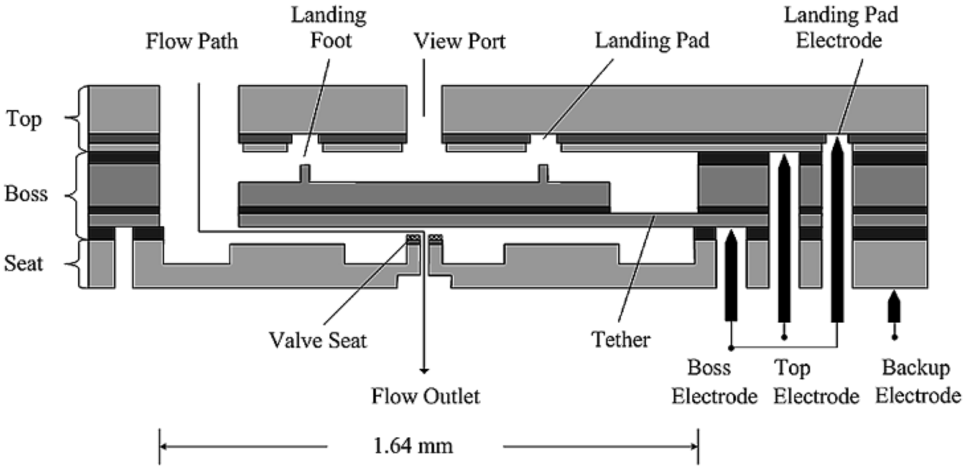

Fig. 14. Two-dimensional cross-sectional schematic of the fuel electrostatic microvalve [20].

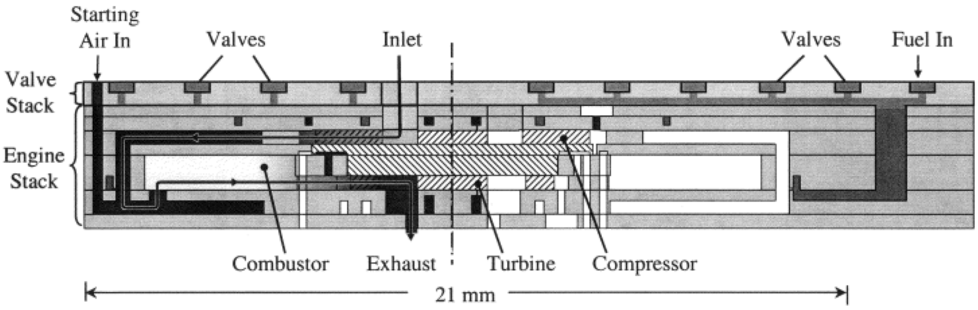

Fig. 15. Cross section of the microengine with integrated electrostatic microvalve array [20].

### 2.1.3 Thermal MEMS Valve

Compared with other MEMS valves, a thermal MEMS valve [22-36] can generate both large stroke and large force. However, there are many drawbacks for the usage of thermal MEMS valve. Since the heating effect actuates thermal MEMS valves, it always consumes more power and operates at a lower frequency that is limited by the cooling and heating. In addition to these disadvantages, its operation temperature is limited, too. Regardless of these limitations, many thermal MEMS valve designs are introduced for high force valve application. As shown in Fig. 16, Kim *et al*. introduces a normally-opened thermal MEMS valve that use PDMS (polydimethylsiloxane) as the main material of the valve and ITO (Indium tin oxide) as the heater. The picture of this design with inlet and outlet are as shown in Fig. 17.

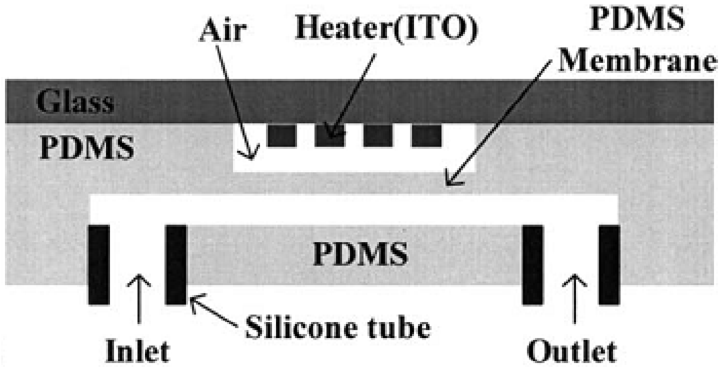

(A) Cross section view of the thermal microvalve

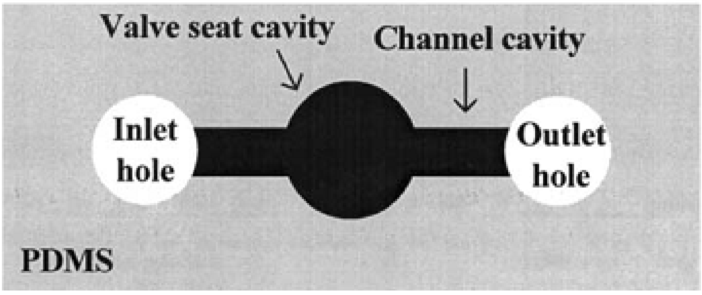

(B) The cavity of PDMS replica of the microvalve

**Fig. 16. Sketch of the thermal microvalve by Kim *et al*. [32].**

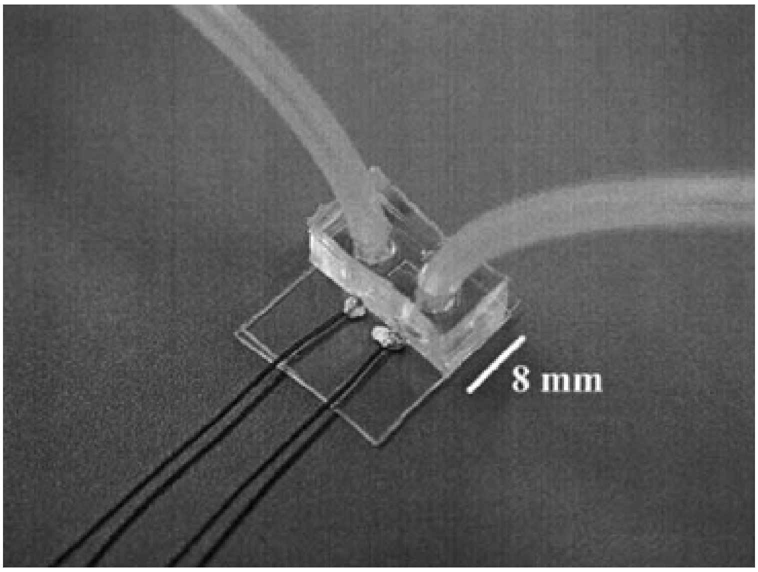

Fig. 17. Photograph of the fabricated thermal MEMS valve by Kim *et al*. [32].

### 2.1.4 Piezoelectric MEMS Valve

The last type of MEM valve is piezoelectric MEMS valve [37-55]. This kind of valve uses electric voltage to control the open/close of the valve with piezoelectric effect [57]. Compared with the other MEMS valves, piezoelectric MEMS valve has low power consumption, high working frequency, good temperature stability, and high operation pressure. Such kinds of advantages make piezoelectric MEMS valves very popular and become widely used in MEMS valve. However, the piezoelectric MEMS valve always generates less generated stroke compared with the other type of MEMS valve. To improve this drawback, an external or internal stroke amplification mechanism is very common in a piezoelectric MEMS valve design to achieve the goal generated stroke. The most stroke amplification mechanism is achieved by hydraulic (external) [39, 40] or mechanical (internal) [50]. Robert *et al.* [40] introduced a design that hydraulically amplifies the stroke to achieve a movement up to 16.5 μm (as shown in Fig. 18). However, this device will have out-of-plane flow and leads to difficulty on controlling the flow. In addition, the hydraulic amplification chamber increases the size significantly since it will introduce a hydraulic chamber into the system. Compared with this hydraulically amplified design, a mechanically amplified design induced by Zhao *et al.* [50] (as shown in Fig. 19) can keep the size small and achieve stroke amplification with bimorph design. So in order to keep the volume of the piezoelectric valve as small as possible, a mechanical stroke amplified should be used while developing a piezoelectric valve system.

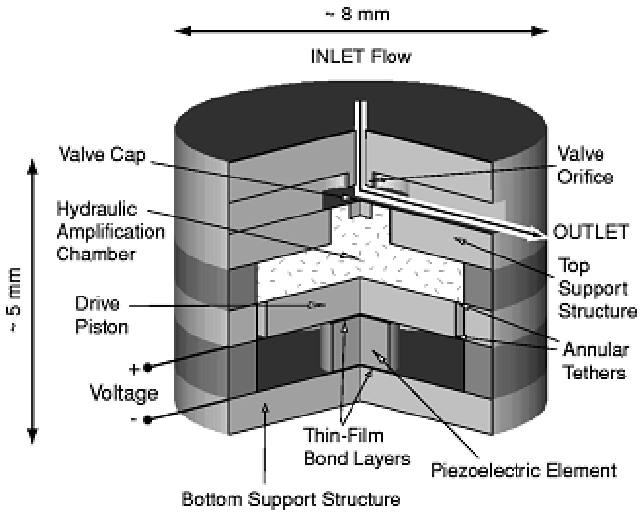

**Fig. 18. Schematic of the piezoelectrically driven hydraulic amplification microvalve by Roberts *et al.* [40].**

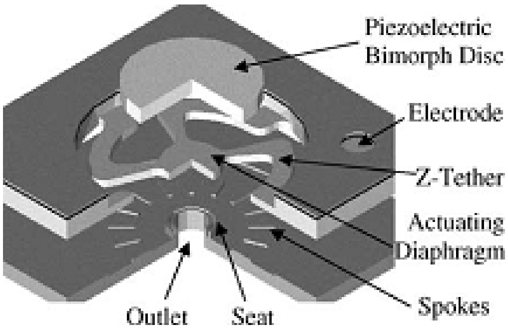

**Fig. 19. Schematic of the piezoelectrically driven mechanical amplification microvalve by Zhao *et al*. [50].**

The benefits and handicaps for these four different kinds of MEMS valve have been discussed in the previous sections. Based these discussions, piezoelectric valves are selected to be the candidate of supercritical carbon dioxide valve since it meets the design requirements for the new printing technology: small volume, high operation frequency, low power consumption, high working pressure, and high temperature stability. And while developing a supercritical carbon dioxide for this new printing technology, a mechanically stroke amplification mechanism will be used in order to gain the desired stroke and keep the volume small at the same time.

## 2.2 Supercritical Carbon Dioxide Valve

Here, since the highest operation pressure of current MEMS piezoelectric valve is less than 5 MPa [48], we design a new supercritical carbon dioxide valve with bi-chevron AlN actuator (as shown in Fig. 20) that meets the requirements of the new supercritical carbon dioxide printing technology. This device has an entrance on the top of the whole system for the supercritical carbon dioxide (as shown in Fig. 20). Before the supercritical carbon dioxide gets into the microchannels and then the nozzles, this supercritical carbon dioxide will be delivered into the carbon dioxide supply at first (as shown in Fig. 20). In the nozzle part, the rapid expansion of supercritical carbon dioxide solution will happen and then generate the extremely small and uniform ink particles. In this valve system, there is a cap will cover the top of the whole system for sealing propose. The actuation mechanism of this supercritical carbon dioxide valve design is achieved by a bi-chevron aluminum-nitride (AlN) actuator. And AlN is a piezoelectric material for the actuation to induce open/close mechanism.

This SCV is designed to have half open and half close mechanism. That means this valve is neither fully open nor fully closed when no electrical voltage is applied (as shown in Fig. 21) to actuate the valve system (the equilibrium point). At the equilibrium point, the fluid can flow through valve if there is any supercritical carbon dioxide exists in the carbon dioxide supply. However, we can control, open or close, the outside carbon dioxide supply source to really turn off the flow at the equilibrium point. While we would like to open the SCV, we can apply an electrical field to push the bi-chevron AlN actuators to move backward and then the fluid can flow through the microchannel to the nozzle (as shown in Fig. 22). With this design, the microchannel will be cleaned when high pressure fluid goes through. Therefore, there will be no block problem because the particles accumulate in the microchannel will be brought by the high pressure fluidic while it goes through the valve. When we would like to close the SCV, we can apply a electrical field to push the bi-chevron actuators to move forward and then the fluid can't flow through the microchannel to the nozzle (as shown in Fig. 23) since there is no path for the fluidic to get to the nozzle.

In Fig. 21, Fig. 22, and Fig. 23, the supercritical carbon dioxide will flow through the valve system from the top, bottom, and side channel. The flow going through the valve system from the top of the plug is labeled as $Q_{top}$. $Q_{top}$ can be reduced by decreasing the distance between the cap and the top of the plug. And the flow going through the valve system from the bottom of the plug is labeled as $Q_{bottom}$. $Q_{bottom}$ can be reduced by decreasing the oxide the distance between the silicon substrate and the bottom of the plug. In the fabrication process for the supercritical carbon dioxide valve, a silicon-on-isolator (SOI) wafer with less oxide thickness will be chosen since that will induce less distance between the bottom of the plug and the silicon substrate. $Q_{top}$ and $Q_{bottom}$ will contribute the leakage of the valve system and should be reduced. And $Q_{side}$ means the flow going through the system with the side channel. For $Q_{side}$, it should be increased as much as possible since it contributes to the flow rate of the valve system without increasing the leakage.

If we combine carbon supply, microchannels, SCVs, and nozzles into the same system, we will get a SCV system (as shown in Fig. 24and Fig. 25) for the supercritical carbon dioxide printing technology. With this combination of the carbon dioxide supply, microchannels, SCVs, and nozzles, we can let the whole SCV system to achieve the following requirements for supercritical carbon dioxide printing technology:

1. *170 μm nozzle-to-nozzle spacing (150 dot per inch (dpi))*: The nozzle to nozzle spacing is designed to be 170 μm. This means this device can achieve the 150 dpi requirement for printing technology.

2. *10 mg/sec carbon dioxide flow rate for each nozzle*: The whole system is designed to have 10 mg/sec carbon dioxide flow rate. With this flow rate, there will be sufficient supercritical carbon dioxide flow to generate the desired ink particles for the printing.
3. *Minimum out-of-plane generated stroke of the actuator due to symmetric design*: The bi-chevron AlN actuator design is symmetric vertically and horizontally. With this bi-direction symmetric design, the out-of-plane generated stroke of the bi-chevron actuator design is minimized.
4. *Operation under 30 MPa*: Unlike the previous MEMS piezoelectric valve designs, this new MEMS piezoelectric valve can operated at a pressure higher than 5 MPa. The new MEMS piezoelectric valve design developed by this work can work under a pressure as high as 30 MPa.
5. *Sufficient sealing force and it can be increased by adding more AlN beams*: The maximum sealing force of the SCV design is determined by the number of the AlN beams in the bi-chevron AlN actuator design. If more sealing force is needed, the number of AlN beams in the bi-chevron AlN actuator design can be increased to achieve this goal.
6. *Easy to extend by simply repeating*: The design of the SCV system doesn't have complex design and geometry and can be extended by repeating the designs in a row. So it is easy to get more exits for the ink particles in a row by simply repeating the SCV designs.

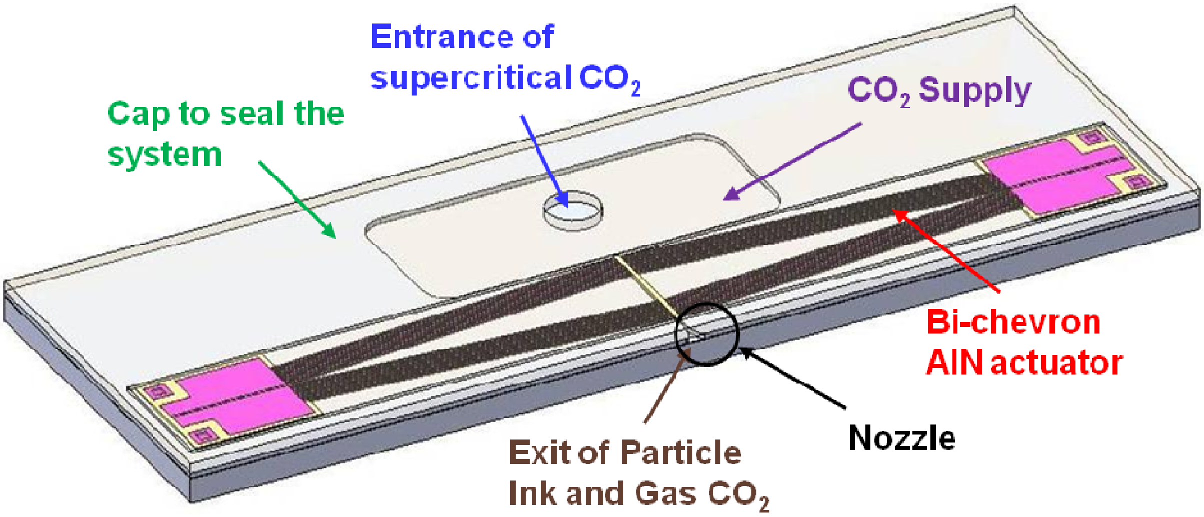

**Fig. 20. Sketch of a single SCV design with cap, entrance of supercritical carbon dioxide, carbon dioxide supply, microvalves, and bi-chevron AlN actuator.**

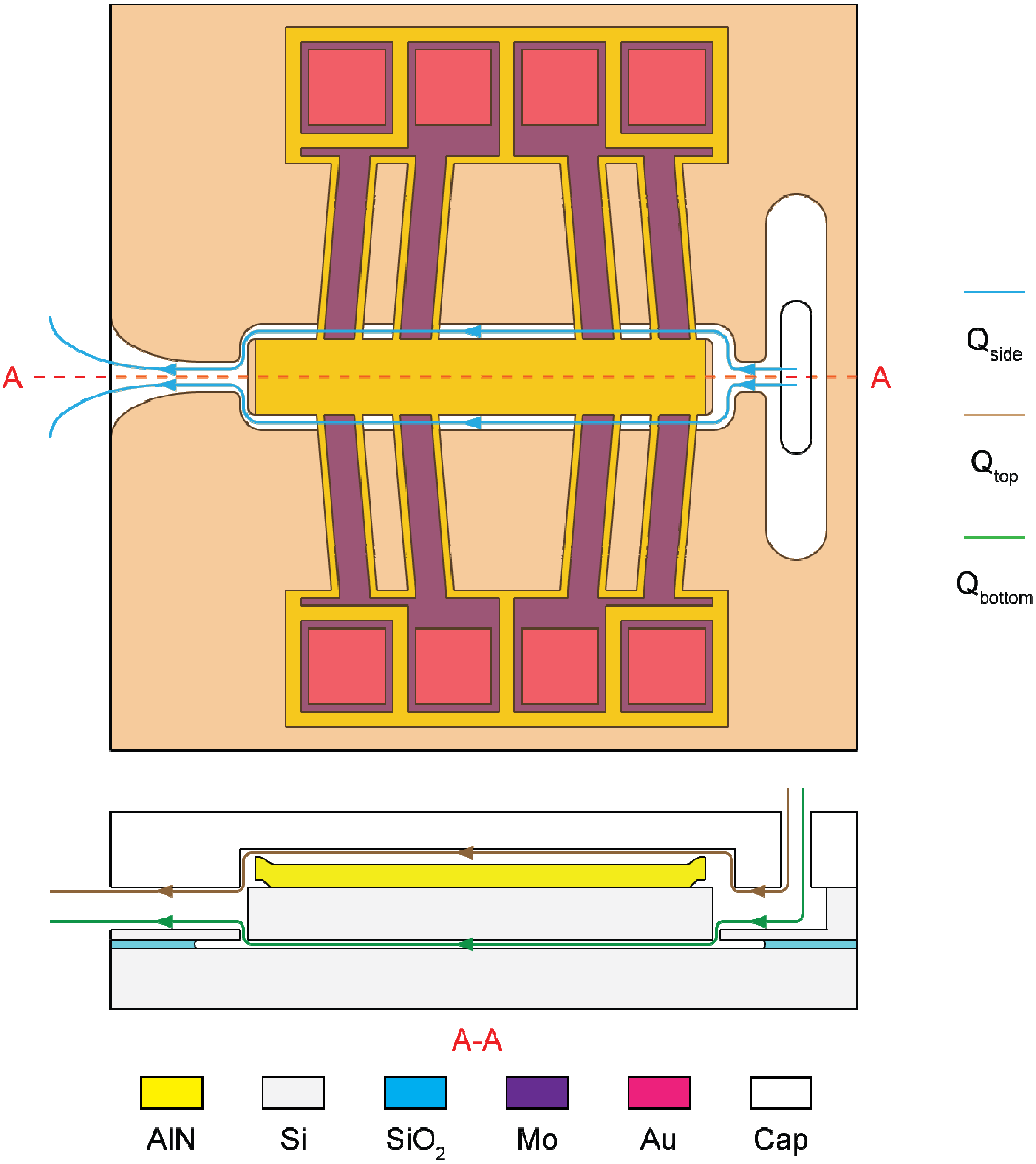

**Fig. 21. Sketch of SCV and flow of supercritical carbon-dioxide device when no electrical field is applied. $Q_{top}$ is the flow going through the valve system from the top of the plug. $Q_{bottom}$ is the flow going through the valve system from the bottom of the plug. $Q_{side}$ is the flow going through the valve system with the side channel.**

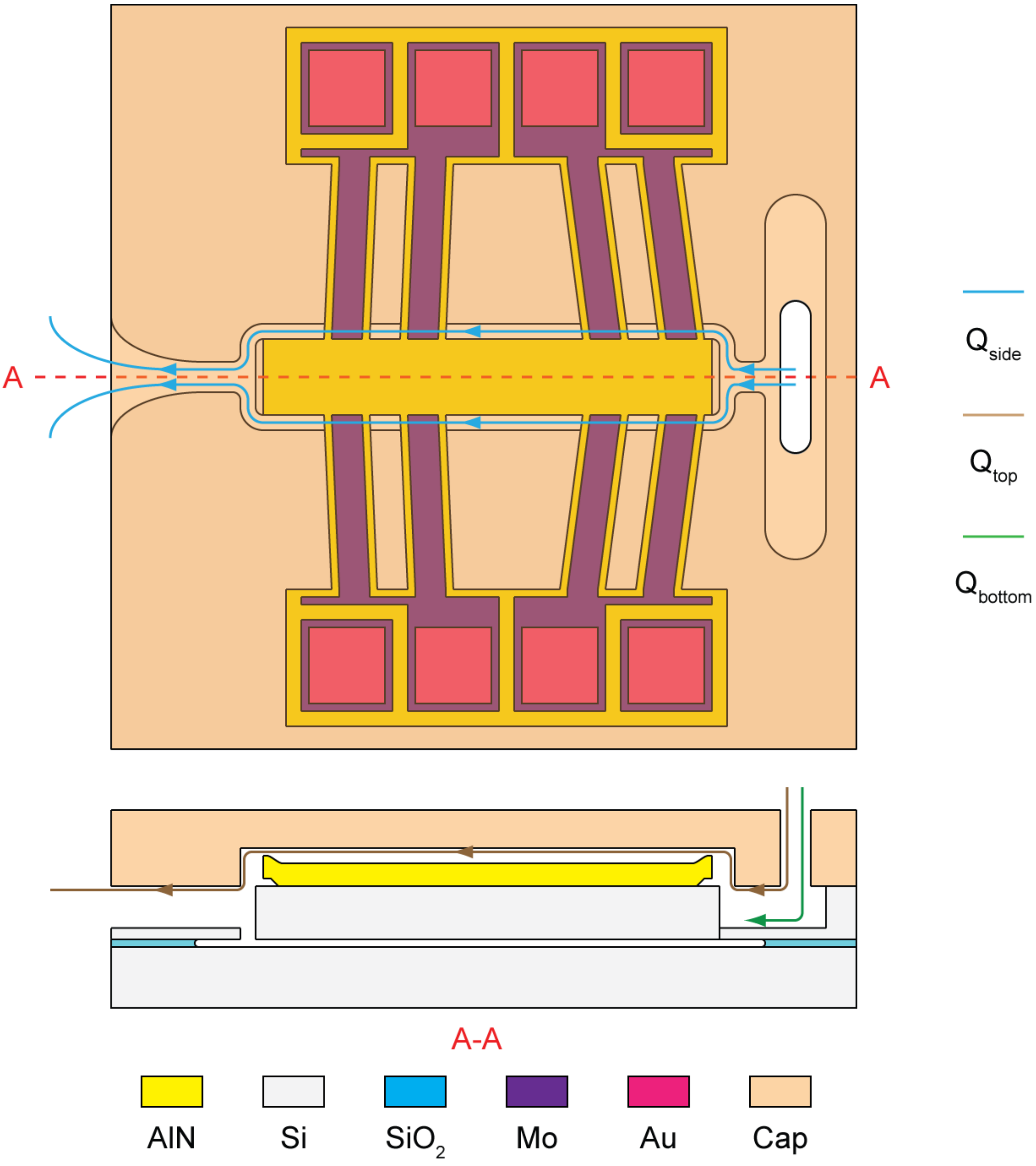

Fig. 22. Sketch of SCV and flow of supercritical carbon-dioxide device when the electrical field is applied to open the valve. $Q_{top}$ is the flow going through the valve system from the top of the plug. $Q_{bottom}$ is the flow going through the valve system from the bottom of the plug. $Q_{side}$ is the flow going through the valve system with the side channel.

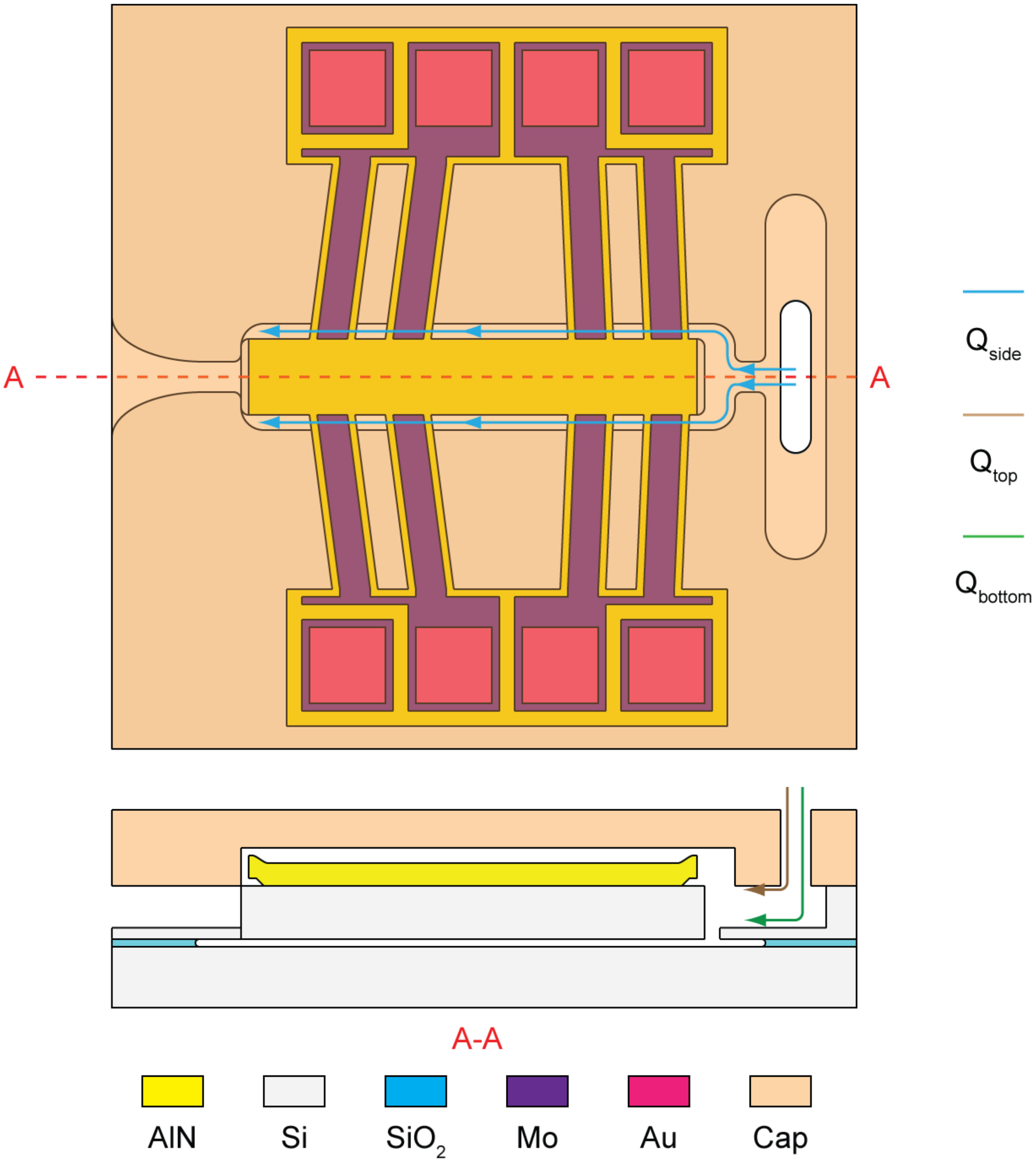

**Fig. 23. Sketch of SCV and flow of supercritical carbon-dioxide device when the electrical field is applied to close the valve. $Q_{top}$ is the flow going through the valve system from the top of the plug. $Q_{bottom}$ is the flow going through the valve system from the bottom of the plug. $Q_{side}$ is the flow going through the valve system with the side channel.**

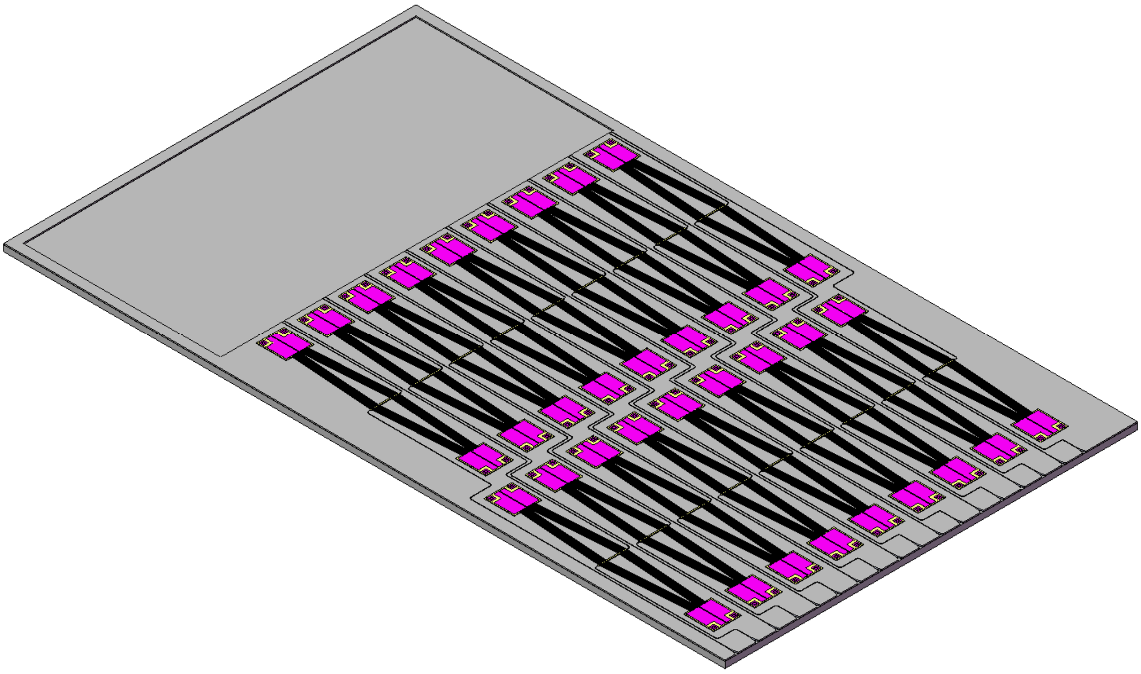

Fig. 24. Sketch of the SCV system without sealing cap.

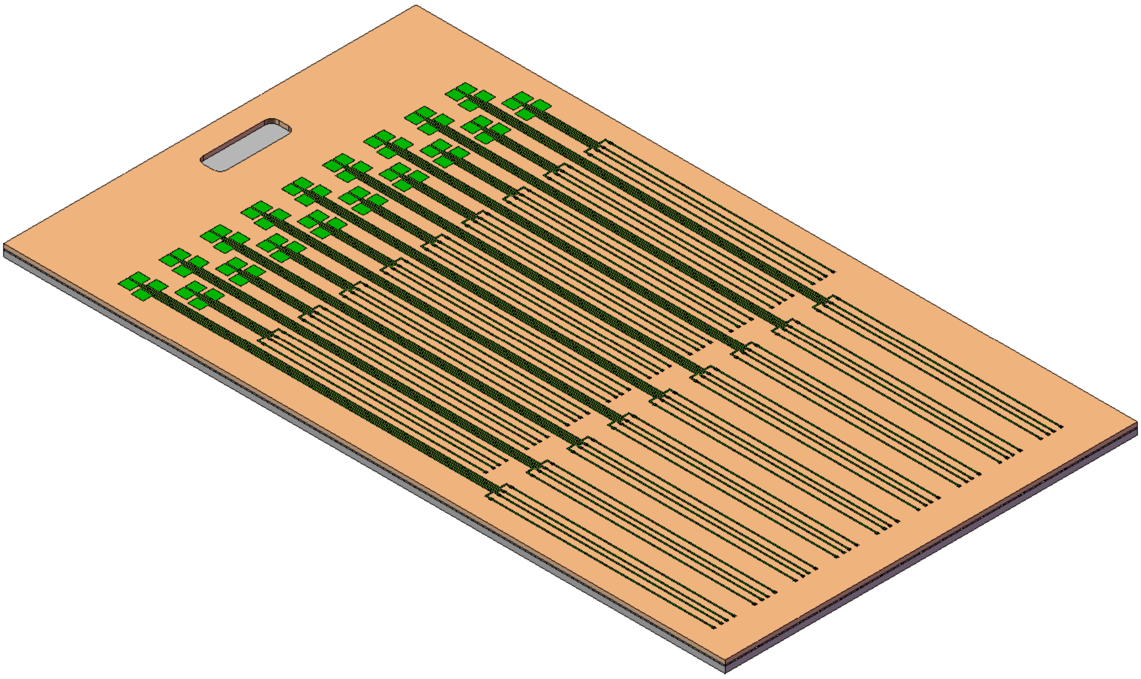

Fig. 25. Sketch of the SCV system with sealing cap.

# Chapter 3 AlN Bi-Chevron Actuator for Supercritical Carbon Dioxide Valve (SCV) Design

## 3.1 Piezoelectric Material for Actuator Application with Stroke Amplification Mechanism

When a piezoelectric material responds to an applied voltage by a change of its shape, it is demonstrating the “inverse piezoelectric effect”. When a piezoelectric material converts mechanical energy to electrical energy, it is demonstrating the “direct piezoelectric effect”. Based on this, for piezoelectric actuators, an electrical energy will be applied on the piezoelectric material to generate a mechanical energy to produce stroke or force to achieve certain purpose. The single-layer piezoelectric actuator can be achieved by transverse mode (as shown in Fig. 26), parallel mode (as shown in Fig. 27), or shear mode (Fig. 28). In Fig. 26, Fig. 27, and Fig. 28, the piezoelectric is free to shrink or expand since there is no opposite force to constrain the deformation. The stroke generated by these different modes of piezoelectric is governed by the following equations:

1. *Parallel mode piezoelectric actuator*: The generated stroke (parallel expansion) can be expressed by the following Equation (3.1)

$$\frac{\Delta T}{T} = E_3 d_{33} = \frac{V}{T} d_{33} \tag{3.1}$$

2. *Transverse mode piezoelectric actuator*: The generated stroke (transverse expansion) can be expressed by the following Equation (3.2)

$$\frac{\Delta L}{L} = \frac{\Delta W}{W} = E_3 d_{31} = \frac{V d_{31}}{T} \tag{3.2}$$

3. *Shear mode piezoelectric actuator*: The generated stroke (movement of the edge) can be expressed by the following Equation (3.3)

$$\Delta X = V d_{15} \tag{3.3}$$

where $\Delta T$ is the elongation or shrink in the thickness direction (the same direction as the polarization), $\Delta L$ the elongation or shrink in the length direction, $\Delta W$ the elongation or shrink in the width direction, $\Delta X$ the relative movement of two corners due to the shear deformation, T is the thickness, L is the length, W is the width, $d_{31}$ is one element of the piezoelectric strain matrix that represents the influence the applied electric field in the polarization/thickness direction on the normal strain change in the width and length direction, $d_{33}$ is one element of the piezoelectric strain matrix that represents the influence the applied electric field in the polarization/thickness direction on the normal strain change in the thickness direction, $d_{51}$ is one element of the piezoelectric strain matrix that represents the influence the applied electric field in the polarization/thickness direction on the shear strain change, and V is the applied voltage on the piezoelectric material. So far, these three different piezoelectric actuator modes have been widely used in the actuator application. And for bi-layer piezoelectric actuator and other kind of piezoelectric actuators, they will use these three piezoelectric modes with some modification to achieve more generated stroke or generated force [58-60].

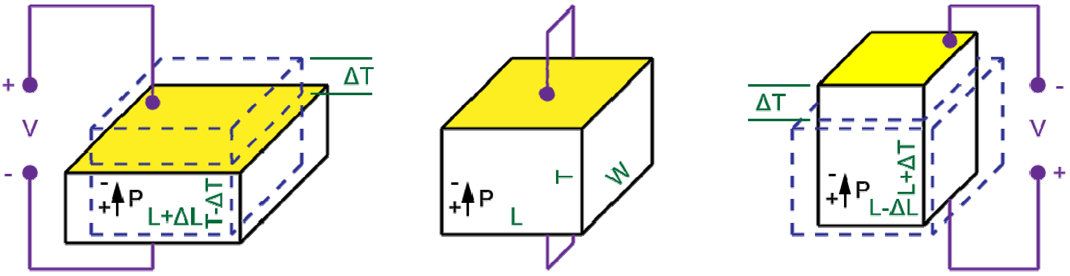

**Fig. 26. Parallel mode piezoelectric actuator where P indicates the polarization the piezoelectric material.**

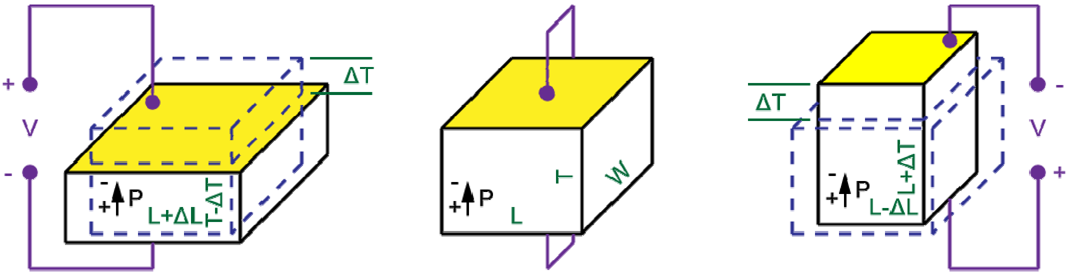

**Fig. 27. Transverse mode piezoelectric actuator where P indicates the polarization the piezoelectric material.**

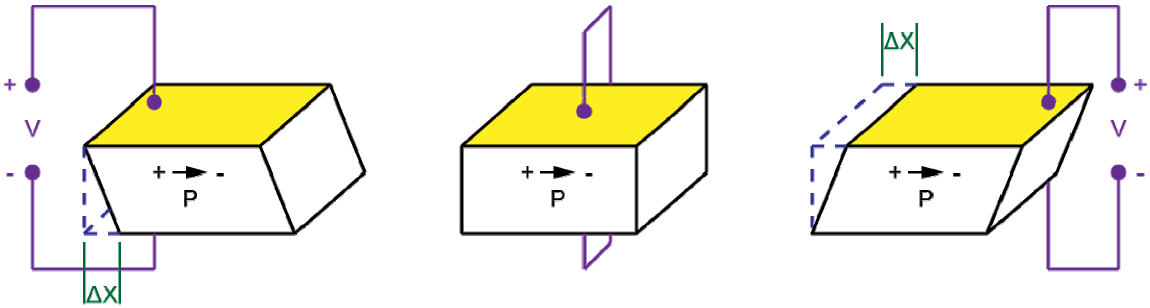

**Fig. 28. Shear mode piezoelectric actuator where P indicates the polarization the piezoelectric material.**

However, the generated stroke of piezoelectric actuator is too small. In order to achieve the desired generated stroke, usually a stroke amplification mechanism is needed. This stroke amplification mechanical can be achieved by an external [61] system or by an internal [62-91] system. This external system can be hydraulic [61]. However, an external stroke amplification mechanism is rarely used since it will increase the volume of the system significantly and add the difficulty to the fabrication process of the device. Due to this reason, an internal stroke amplification system is more popular than an external stroke amplification mechanism. This internal system can be achieved by bimorph system [62-69] (as shown in Fig. 29), buckle beam [70] (as shown in Fig. 30), cantilever beam [71-80] (as shown in Fig. 31), rainbow structure [81-83] (as shown in Fig. 32), or stacked structure [84-91] (as shown in Fig. 33).

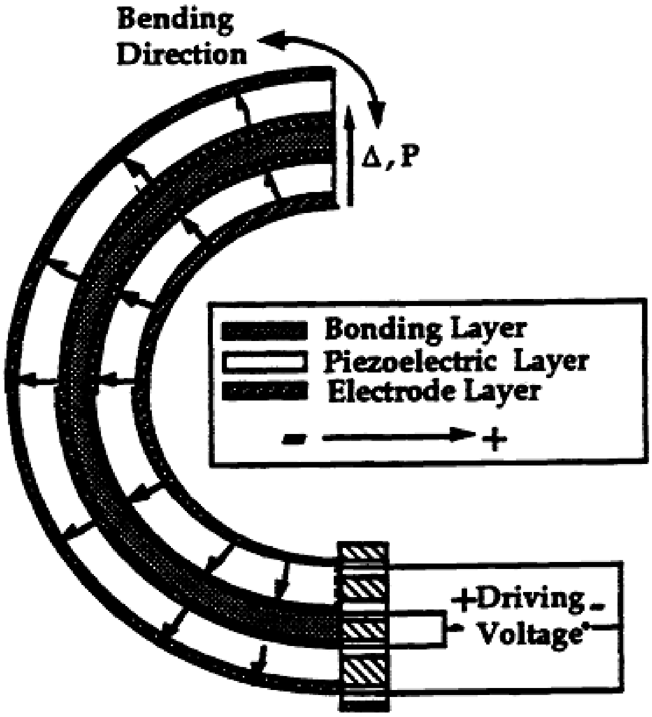

**Fig. 29. Sketch of C-block actuator and showing material layers design arrows indicating the poling direction by Brei *et al.* [62].**

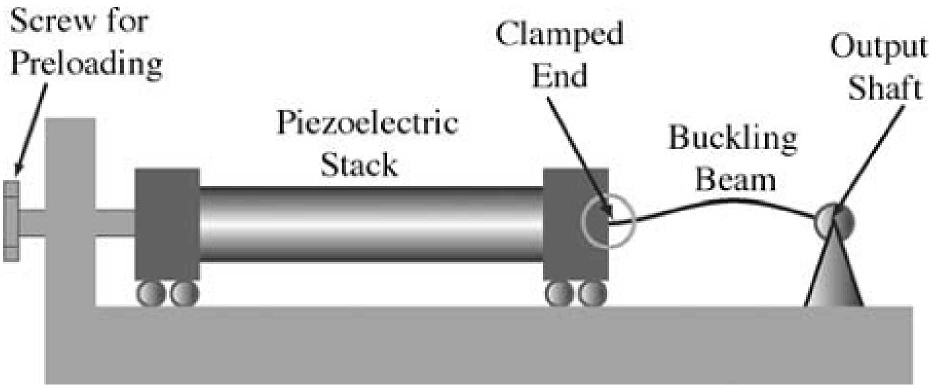

**Fig. 30. Sketch of buckling beam motion amplifier by Jiang *et al*. [70].**

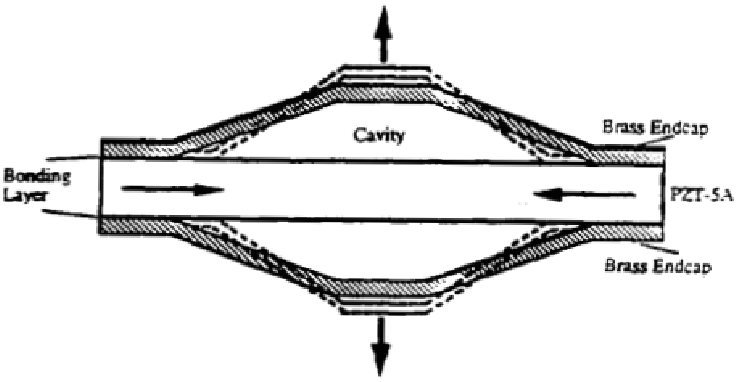

**Fig. 31. Sketch of the cymbal transducer by Dogan *et al*. [71].**

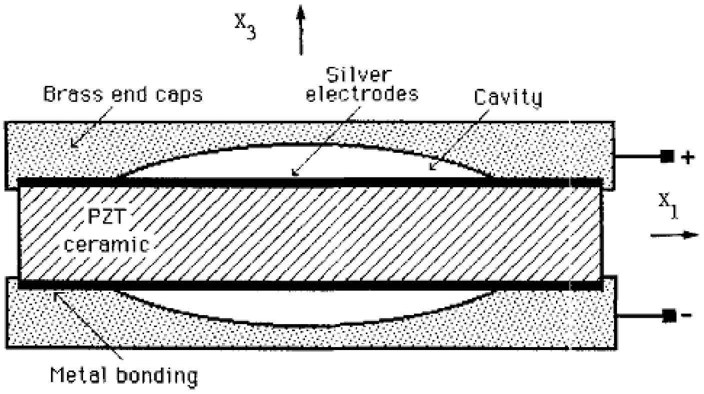

**Fig. 32. Sketch of composite Moonie actuator by Sugawara *et al*. [81].**

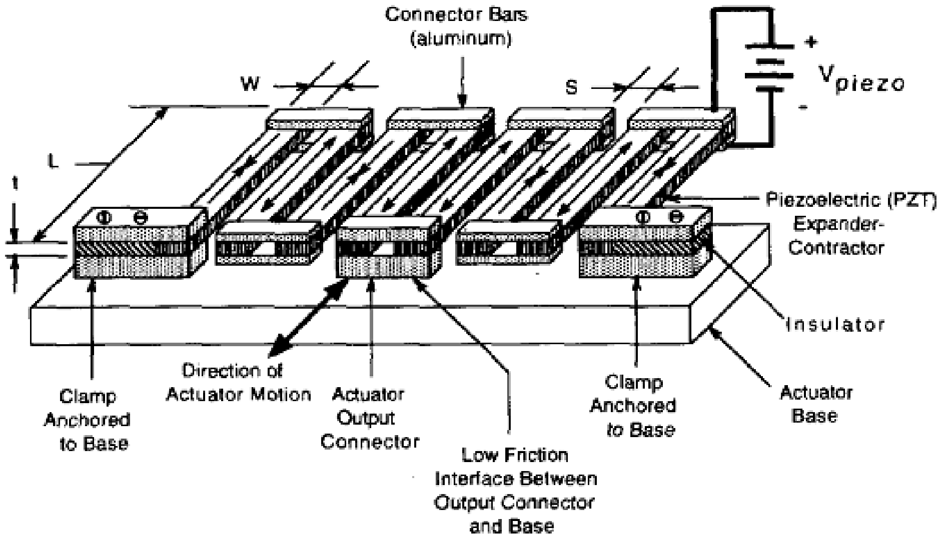

**Fig. 33. Sketch of the meader-line actuator by Robbins *et al.* [84]. The meander line is supported at its clamped ends and in the middle where the actuator output connector slides on the actuator base. All of the piezoelectric bars are connected electrically in parallel by the conducting (aluminum) connector bars.**

Compared with other piezoelectric material, lead zirconate titanate (PZT) is most popular material for piezoelectric actuator applications and has been widely used. However, lead zirconate titanate ((Pb[ZrxTi$_{1\text{-}x}$]O$_3$, $0<x<1$) or PZT) has the following disadvantages:

1. *Not integrated circuit (IC) compatible*: Lead (Pb) is avoided to be used in current semiconductor fabrication process since it is toxic. That is why PZT is not IC compatible since it contains Pb.
2. *External strong field and high temperature for PZT polarization process*: For PZT material, it is not polarized while just getting deposited. And an external strong electric field and high temperature process is needed to force the PZT material gets polarization [92-94]. This external strong electric field and high temperature process may damage the IC underneath.
3. *Compressive-stress depolarization*: PZT material always suffers a decrease of piezoelectric coefficient while working under high pressure (compressive stress) [95-98]. This limited the maximum operation pressure of the piezoelectric valve with PZT can work.

Due to these results, PZT is not chosen as the piezoelectric material for the supercritical carbon dioxide valve design. For the supercritical carbon dioxide valve, we introduce AlN as the piezoelectric material. Aluminum-nitride (AlN) is a wurtzite phase (w-AlN) material with a wide band gap (6.2 eV) and is widely used in MEMS now, especially for deep ultraviolet optoelectronics and radio frequency (RF) filter applications. The details of AlN material properties are given in Appendix B. AlN is a hard piezoelectric material and is capable of generating relatively large forces during actuation. Sputtered AlN is deposited as intrinsically piezoelectric and then it requires no poling. And AlN can withstand high compressive stress without compressive-stress depolarization. In addition, AlN is compatible with CMOS, which allows integration of piezoelectric devices with control circuitry. Last, AlN has higher Young's modulus than the other piezoelectric materials and then can produce higher wave speed which will generate higher frequency for higher working speed.

The breakdown electric field ($E_B$), of piezoelectric material is the other important limitation for the operation and should be considered carefully before the operation. The breakdown electric field is the maximum electric field that the piezoelectric material can sustain without causing any damage to the device. To avoid any possible damages coming from the exceed applied electric field, our design will be operated under a electric field that is half of the breakdown electric field. For AlN, its breakdown electric field is 1400 kV/cm. So for 1 μm thick AlN film, the maximum voltage difference can be applied on the AlN film is 140 V. And for 3 μm thick AlN film, the maximum voltage difference can be applied on the AlN film should be 420 V. This rule about the maximum applied electric field will be followed when the actuator design is operated for the desired working function.

## 3.2 Operation of Bi-Chevron Actuator

Here we introduce a new actuator design, bi-chevron AlN actuator, with generated stroke amplification mechanism for the supercritical carbon-dioxide valve (SCV). The sketch of this bi-chevron AlN actuator design is as shown in Fig. 34. This bi-chevron AlN actuator design is a modification of the chevron thermal actuator design described by Sinclair *et al.* [99] (as shown in Fig. 35). This thermal actuator design can generate high generated force and amplify the generated stroke with the chevron structure. However, due to the work function of thermal actuator, this chevron thermal actuator can only move in "uni-direction" and unwanted out-of-plane stroke will be generated at the same time. In order to improve this design, we introduce a "bi-directional AlN chevron actuator" (bi-chevron AlN actuator, as shown in Fig. 34) which can generate bi-directional movement and reduce out-of-plane generated stroke at the same time.

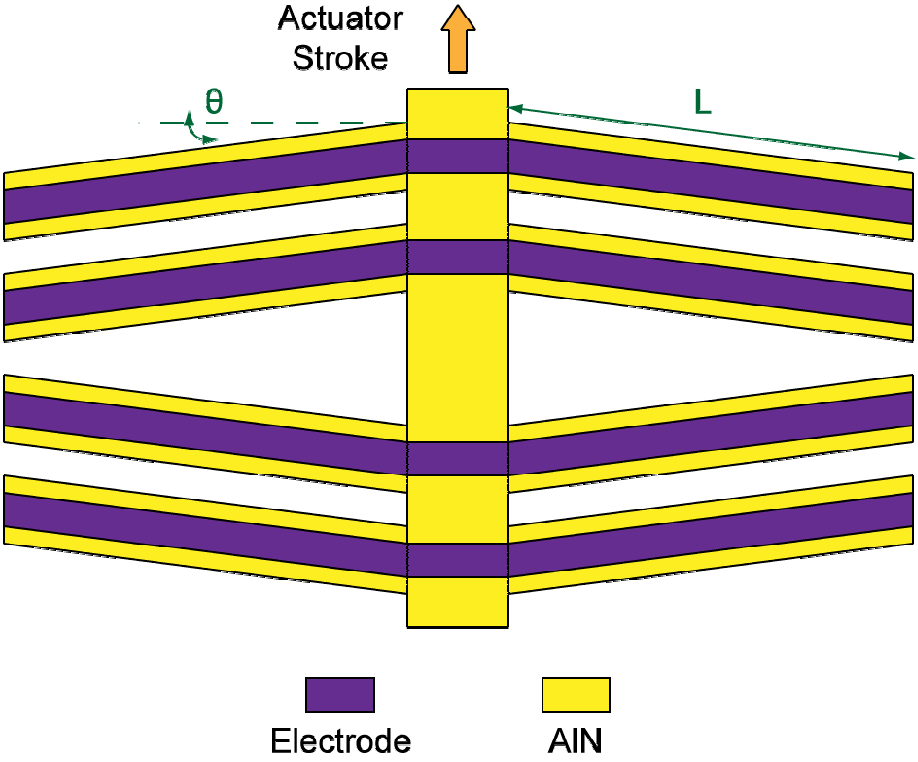

Fig. 34.  Bi-chevron AlN actuator design.

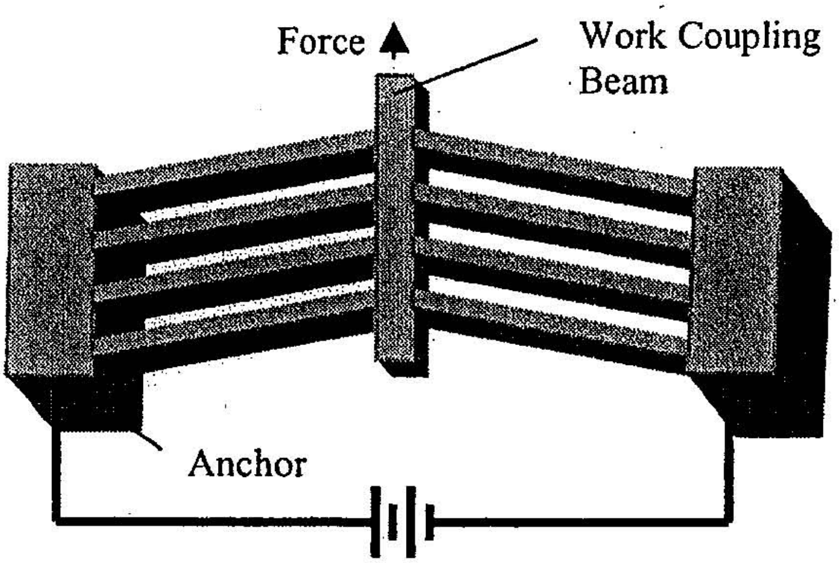

Fig. 35.  Chevron thermal actuator [99].

This bi-chevron actuator is made of piezoelectric material, AlN, and has equal pairs of piezoelectric AlN beams in both right side and left side. And for each side, there is the same number of piezoelectric beams in upper pair and lower pair. When we apply a negative electrical field to the polarization to the upper pair piezoelectric beams (A-A cross-section in Fig. 36) and a positive electrical field to the polarization to the lower pair piezoelectric beams (B-B cross-section, as shown in Fig. 36), this will make the upper pair piezoelectric beams start to expand (A-A cross-section, as shown in Fig. 36) and the lower pair piezoelectric beams start to shrink (B-B cross-section, as shown in Fig. 36). And this combination of the push (by the upper pair AlN beams) mechanism and the pull (by the lower pair AlN beams) mechanism will force the actuator to move forward (as shown in Fig. 36). At this time, the upper pair piezoelectric beams expand and tend to have some out-of-plane stroke. However, the lower pair piezoelectric beams want to shrink and constrain this out-of-plane stroke. So with this symmetric design of upper pair and lower pair piezoelectric beams, the out-of-plane generated stroke is decreased compared to a traditional chevron design.

When we would like to move the actuator backward, a positive electrical field will be applied to the polarization to the upper pair piezoelectric beams and a negative electrical field will be applied to the polarization to the upper pair piezoelectric beams (as shown in Fig. 37). And then the upper pair piezoelectric beams start to shrink (A-A cross-section, as shown in Fig. 37) and the lower pair piezoelectric beams start to expand (B-B cross-section, as shown in Fig. 37). And then this push (by the lower pair AlN beams) and pull (by the upper pair AlN beams) mechanism will force the actuator to move down. That means that we can control the movement of the bi-chevron AlN actuator by altering the electrical field to achieve the bi-directional movement and this design gives us more freedom of movement. In addition, the generated force of the bi-chevron AlN actuator can be increased by adding more AlN beams into the system. If less generated force and less volume of the system are needed, we also can decrease the number of AlN beams to achieve these requirements.

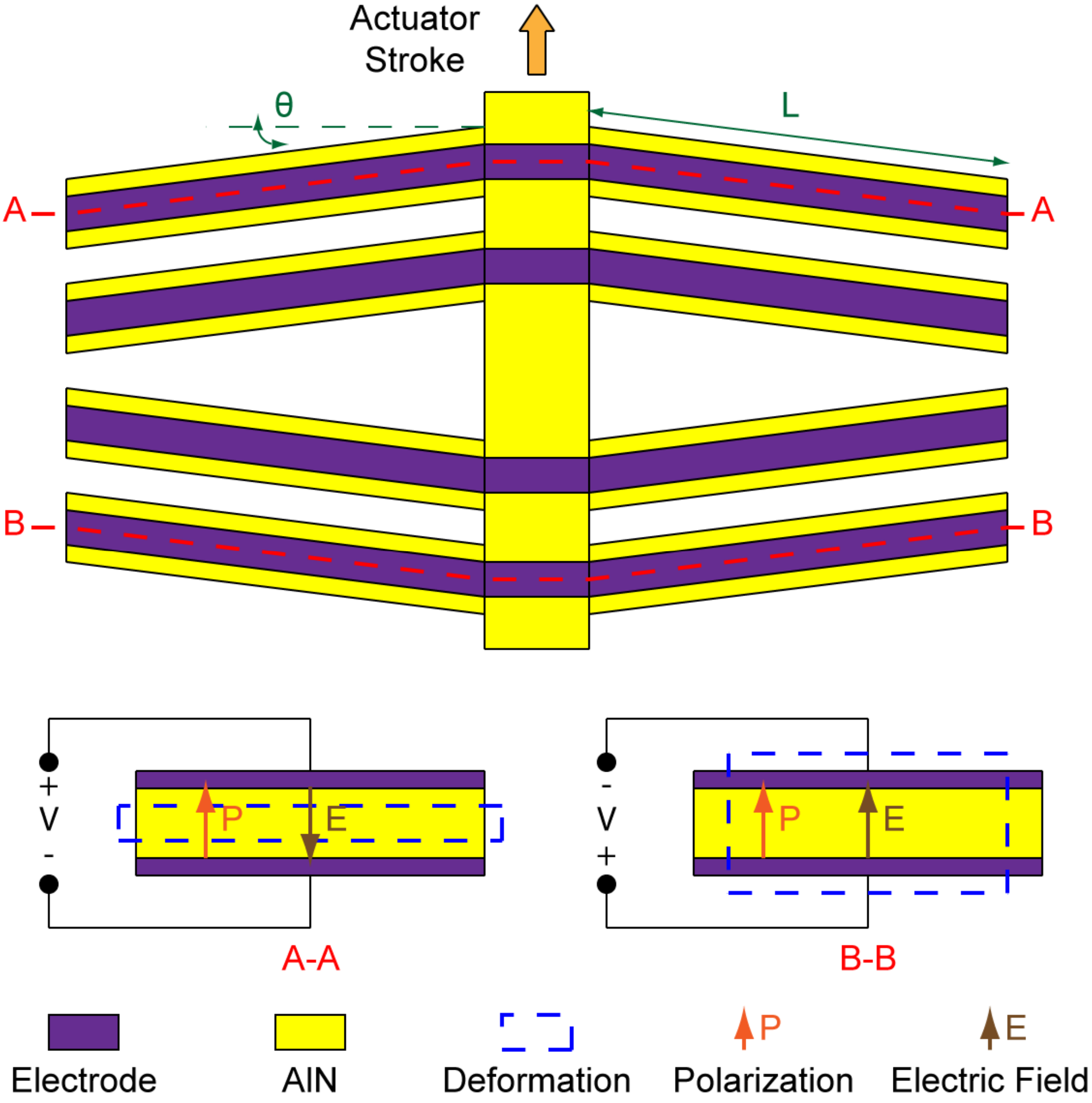

Fig. 36. Sketch of the bi-Direction chevron AlN actuator for moving forward.

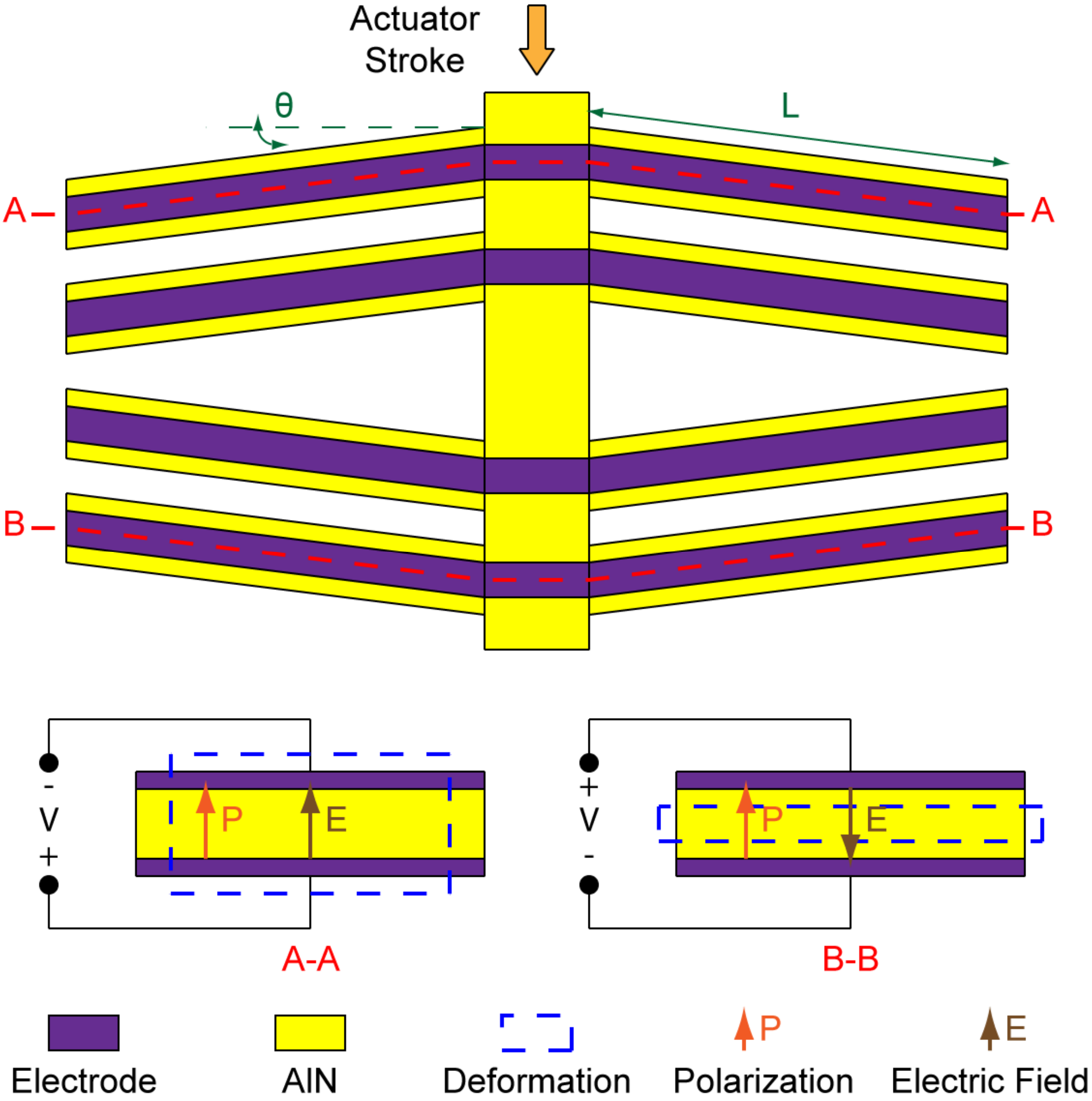

Fig. 37. Sketch of the bi-Direction chevron AlN actuator for moving backward.

## 3.3 Theoretical Analysis for Bi-Chevron AlN Actuator Design

In order to estimate the generated stroke and generated force of the bi-chevron AlN actuator, a simplified model for the bi-chevron AlN actuator is introduced and this simplified model is as shown in Fig. 38. This simplified model can be used to estimate the operation of an expansive AlN beam in the bi-chevron AlN actuator due to the applied electrical field that is in the opposite direction of the polarization of AlN film. Once this simple mechanical model is defined, the following equation can be used to calculate the generated stroke (Δy):

$$\Delta y = L \times \left[-sin\theta + \sqrt{\left(1+\frac{\Delta L}{L}\right)^2 - (cos\theta)^2}\right] \tag{3.4}$$

where Δy is the generated stroke with the stroke amplified mechanism, ΔL is the length expansion of the AlN beam due the applied electric field, L is the original length of the AlN beam without applied electrical field, and θ is the initial angle of the actuator beam without applied electrical field. From Equation (3.2), we know the expansion of AlN beam is a function of actuating voltage (V) and applied electrical field ($E_3$) in the polarization direction:

$$\frac{\Delta L}{L} = \frac{\Delta W}{W} = \frac{Vd_{31}}{T} = E_3 d_{31} \tag{3.2}$$

Equation (3.4) and Equation (3.2) can be combined to get the following equation (3.5) to show the relationship between the generated stroke (Δy) and the applied electrical field ($E_3$)

$$\Delta y = L \times \left[-sin\theta + \sqrt{(1+E_3 d_{31})^2 - (cos\theta)^2}\right] \tag{3.5}$$

And the stroke amplification can be represented as the following equation:

$$\frac{\Delta y}{\Delta L} = \frac{L}{\Delta L} \times \left[-sin\theta + \sqrt{\left(1+\frac{\Delta L}{L}\right)^2 - (cos\theta)^2}\right] \tag{3.6}$$

Equation (3.6) can be combined with Equation (3.2)

$$\frac{\Delta y}{\Delta L} = \frac{1}{E_3 d_{31}} \times \left[-sin\theta + \sqrt{(1+E_3 d_{31})^2 - (cos\theta)^2}\right] \tag{3.7}$$

From Equation (3.7), we find out the stroke amplification is independent of the geometry of the AlN. It is only relative to the applied electrical field ($E_3$), the material properties of AlN ($d_{31}$), and the AlN beam angle (θ).

And from the simplified model, the generated force, P, can be calculated with the following equation:

$$P = Fsin\theta \tag{3.8}$$

where F is the force that the piezoelectric beam generates in the beam length direction and P is the generated force coming from transformation of the beam force, F, to the moving direction because of the amplification mechanism. The actuating beam force, F, is a function of the area of the cross section (A) and the normal stress ($S_{11}$) on the cross section and is shown in the following equation:

$$F = A \times S_{11} = (W \times T) \times (E_3 \times e_{31}) \tag{3.9}$$

where the normal stress ($S_{11}$) is the function of the applied electric field ($E_3$) and the piezoelectric stress coefficient ($e_{31}$). Equation (3.8) and equation (3.9) can be combined to get the following Equation (3.10) to describe the relationship between generated force (P) and applied electrical field ($E_3$)

$$P = (W \times T) \times (E_3 \times e_{31}) \times sin\theta \tag{3.10}$$

Equation (3.5) and equation (3.10) are the governing equations for the operation of a single AlN beam in the bi-chevron AlN actuator design. We find out Equation (3.5) and Equation (3.10) are both function of beam angle (θ). In order to evaluate how beam angle (θ) influences the generated stroke (Δy) and the generated force (P), we will introduce two performance parameter, normalized generated stroke (Δy/L) and normalized generated force (P/F), and they are defined as the following equations:

$$\frac{\Delta y}{L} = -sin\theta + \sqrt{(1 + E_3 d_{31})^2 - (cos\theta)^2} \tag{3.11}$$

And

$$\frac{P}{F} = sin\theta \tag{3.12}$$

With these two equations above, we can plot normalized generated stroke (Δy/L) and the normalized generated force (P/F) as function as the beam angle (θ) (as shown in Fig. 39). In Fig. 39, the applied electrical field ($E_3$) is half of the breakdown electrical field ($E_B$). The piezoelectric material used in this theoretical analysis is AlN and its material properties are as shown in Appendix B. From Fig. 39, it shows that the generated stroke will decrease and the generated force will increase when the beam angle is increasing. Thus, there is a trade-off between generated stroke and generated force since they are both function of beam angle. If more generated force is needed, more AlN beams can be added into our design without significantly diminishing the generated stroke. For the generated stroke amplification, we can use Equation (3.7) to calculate the value and the plot is shown in Fig. 40. From Fig. 40, we know the generated stroke is amplified at least 5 times with the bi-chevron design.

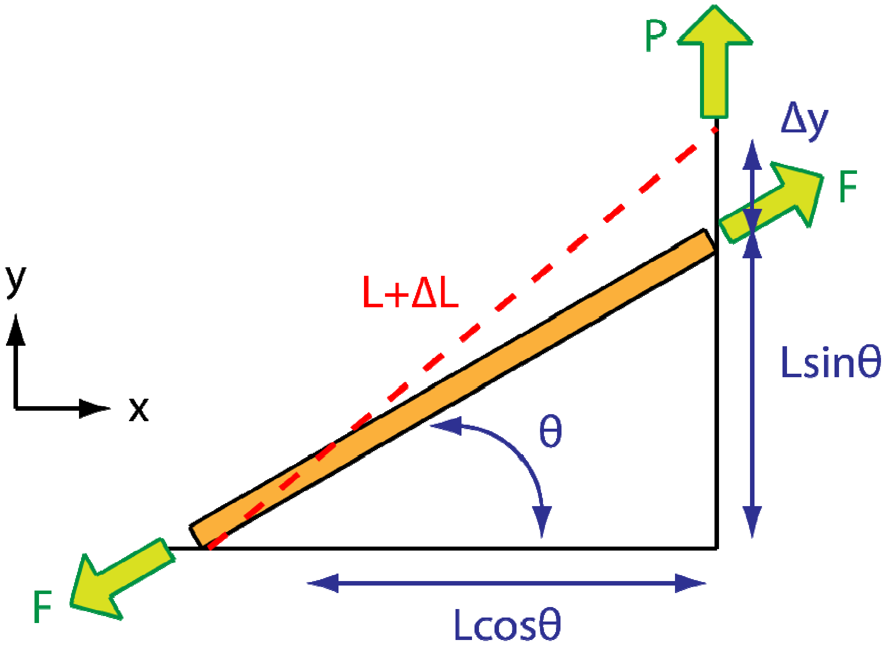

Fig. 38.  Simplified model for the bi-chevron actuator design.

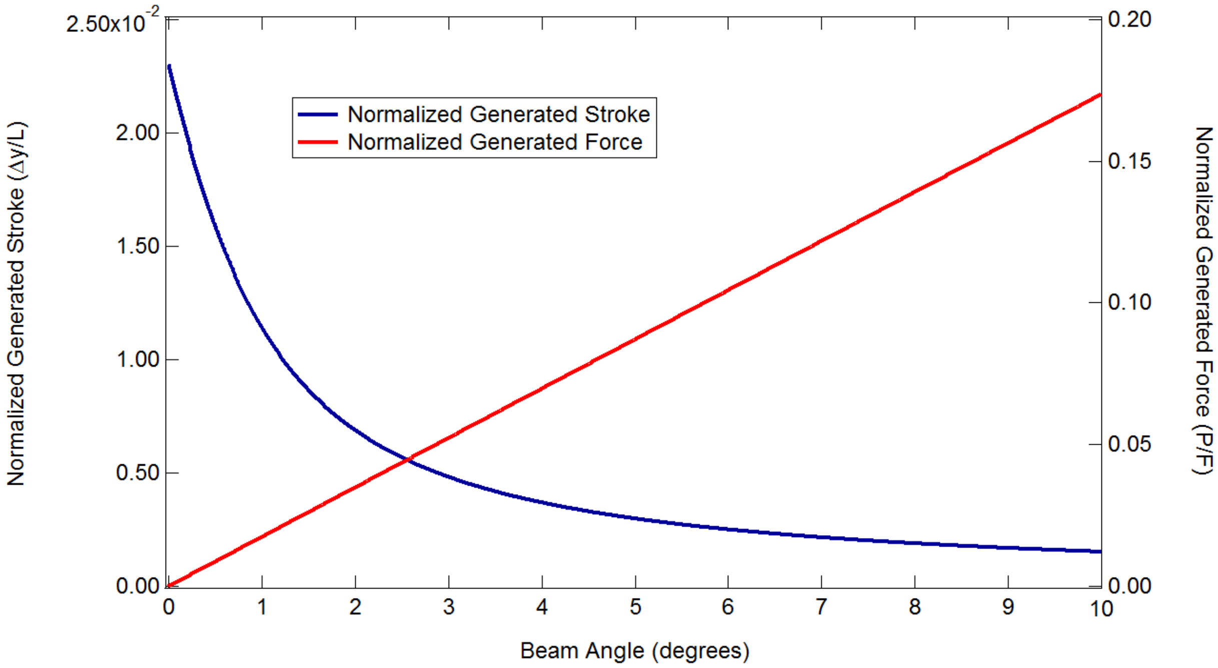

Fig. 39.  Normalized generated stroke and normalized generated force as a function of piezoelectric beam angle.

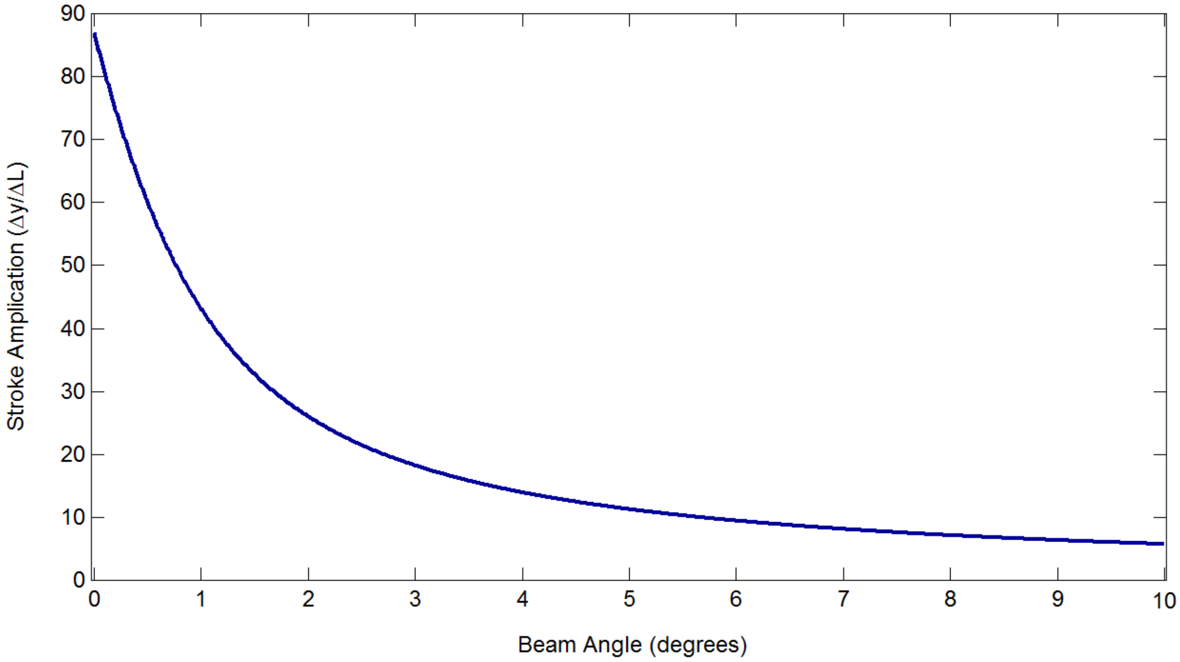

**Fig. 40. Generated stroke amplification as a function of piezoelectric beam angle.**

To get acceptable generated stroke and generated force from the bi-chevron AlN actuator at the same time, we need to choose a value of the beam angle that can achieve these requirements. From Fig. 39 and Fig. 40, we choose 4° to become the beam angle since it can gives generated stroke about 15 times without losing too much generated force. This beam angle will be used for the design of the goal device, supercritical carbon dioxide valve (SCV).

## 3.4 Generated Stroke Simulation for Bi-Chevron AlN Actuator Design with ANSYS

Here, we will use finite-element-method (FEM) to simulate the operation of this bi-chevron AlN actuator design. The software that we use for this FEM simulation is ANSYS with the element Solid 5. Solid 5 is an element that is compatible for the static and dynamic simulation for piezoelectric material. The bi-chevron AlN actuator in the FEM simulation has 8 AlN beams in the each pair (Fig. 41 and Fig. 42). In the following FEM simulation, we will change the length of AlN beams, the width of the AlN beams, the thickness of AlN beams, and the beam angle of the AlN beams to evaluate influence of the geometry on the performance of bi-chevron AlN actuators.

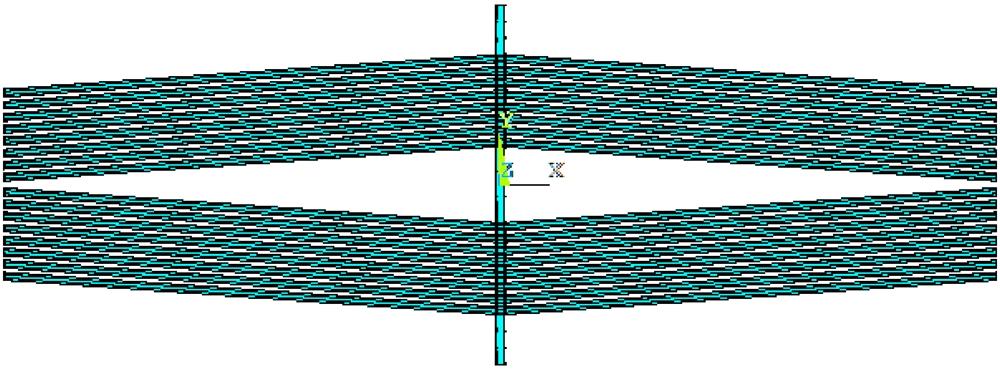

**Fig. 41. Top view of FEM mode for bi-chevron actuator simulation. There are 8 AlN beams in each pair AlN beams.**

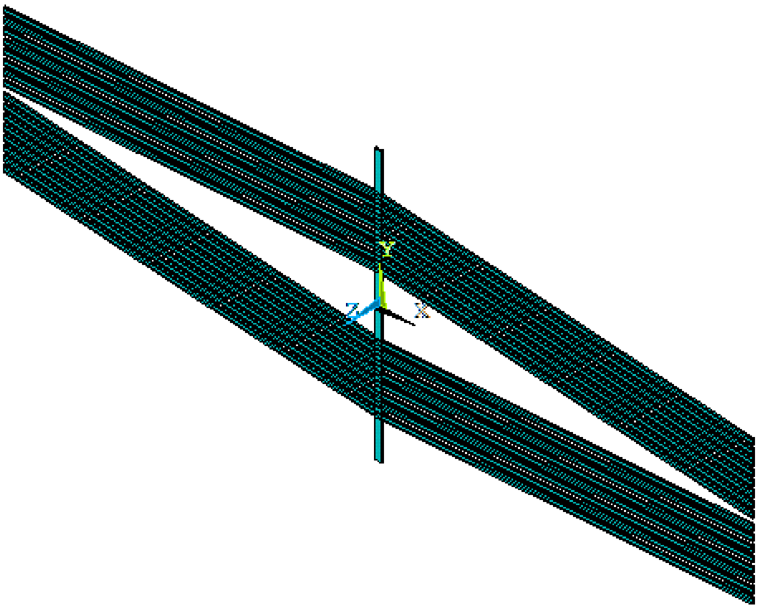

**Fig. 42. Isotropic view of FEM mode for bi-chevron actuator simulation.**

In addition to the influence of geometry, we also consider the effect the coverage of top and bottom electrode. In the fabrication process, we can have the self-alignment bottom electrode (as shown in Fig. 43 (A)) and non-self-alignment bottom electrode (as shown in as shown in Fig. 43 (A)). In the simulation, the gap between the edge of top/bottom electrode and AlN is 3 µm. The fabrication process of devices with non-self-alignment bottom electrodes is to pattern the bottom electrode first, deposit AlN next, and then pattern the AlN in the end. For the device with self-alignment bottom electrodes, the bottom electrode and AlN will be pattern in the same time.

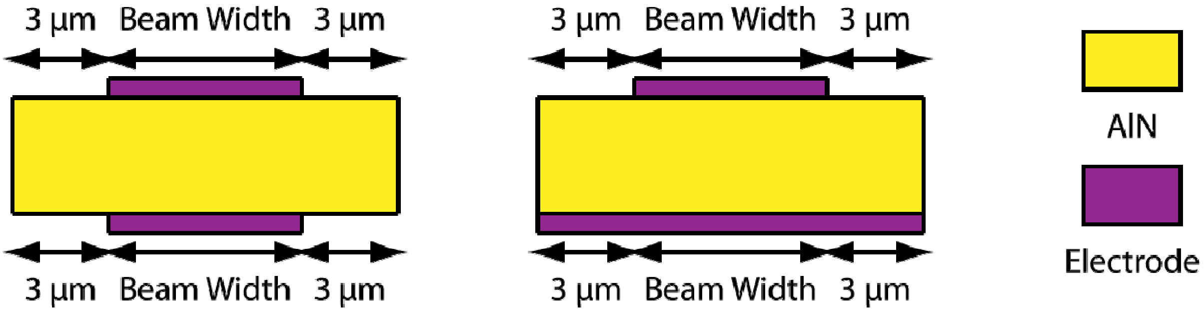

(A) Non-self-alignment bottom electrode

(B) Self-alignment bottom electrode

**Fig. 43. Cross section of non-self-alignment bottom electrode and self-alignment bottom electrode.**

The generated stroke of devices with non-self-alignment bottom electrode for 500 µm long AlN beam, 700 µm long AlN beam, 900 µm long AlN beam, and 1100 µm long AlN beam with different beam width, different beam angle, and different beam thickness is as shown in Fig. 44, Fig. 45, Fig. 46, and Fig. 47. In these figures, the applied electrical field is kept at 100 volt/µm for all devices. From Fig. 44, Fig. 45, Fig. 46, and Fig. 47, we can observe the influence of AlN beam length, AlN beam width, AlN beam angle, and AlN beam thickness on generated stroke and the influence of these geometry parameter are summarized as following:

A. The AlN beam angle will influence the generated stroke. Generated stroke will decrease when AlN beam angle increases. This is the same as what is predicated in Equation (3.5).
B. The AlN beam length will influence the generated stroke. Generated stroke will increase when AlN beam length increases. This is the same as what is predicated in Equation (3.5).
C. The AlN beam width will influence the generated stroke. When the width of the AlN beam is increasing, the generated stroke will increase.
D. The AlN beam thickness will have small influence on the generated stroke.

For the device with self-alignment bottom electrode, the generated stroke of devices for 500 µm long AlN beam, 700 µm long AlN beam, 900 µm long AlN beam, and 1100 µm long AlN beam with different beam width, different beam angle, and different beam thickness is as shown in Fig.

48, Fig. 49, Fig. 50, and Fig. 51. From Fig. 48, Fig. 49, Fig. 50, and Fig. 51, we can find the same characteristics of the influence of AlN beam length/width/angle/thickness on generated stroke for device with non-self-alignment bottom electrode as for device with self-alignment bottom electrodes.

To estimate the influence of non-self-alignment bottom electrode and of self-alignment bottom electrode, the generated stroke of device with these two different bottom electrodes can be put in the same plot (as show in Fig. 52). From Fig. 52, we can know the generated stroke of devices with self-alignment bottom electrode is more than the generated stroke of devices with non-self-alignment bottom electrode. This is because the devices with non-self-alignment bottom electrode will result in a less uniform electrical field along the width of the AlN beam and simultaneously reduce the generated stroke.

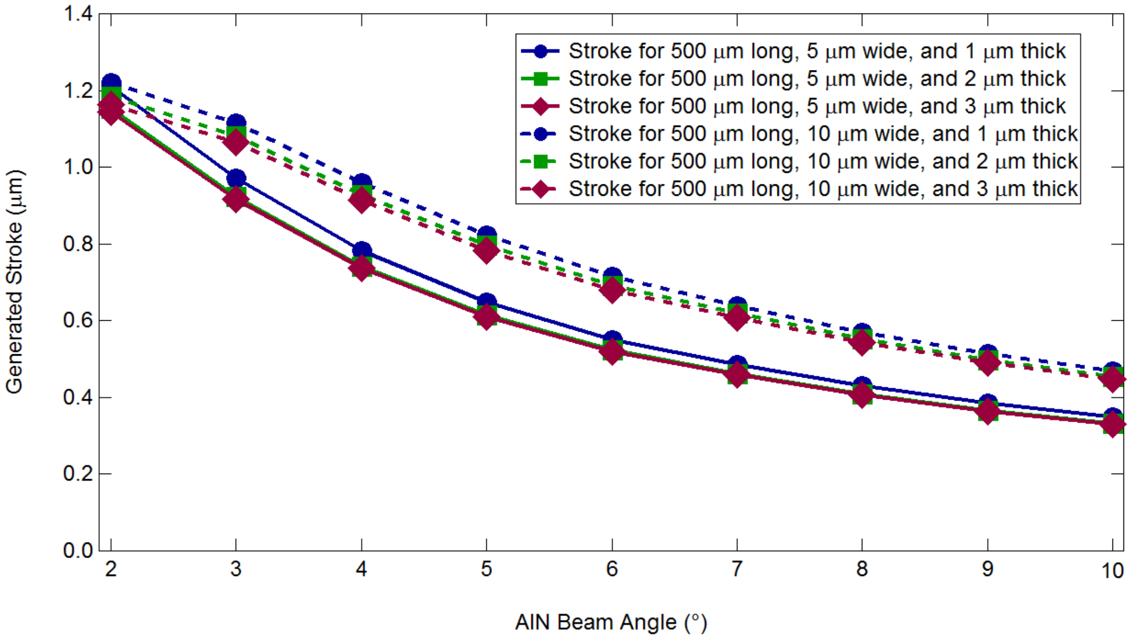

**Fig. 44. Generated stroke of non-self-alignment bottom electrode for 500 µm long AlN beam with different beam width and different beam angle.**

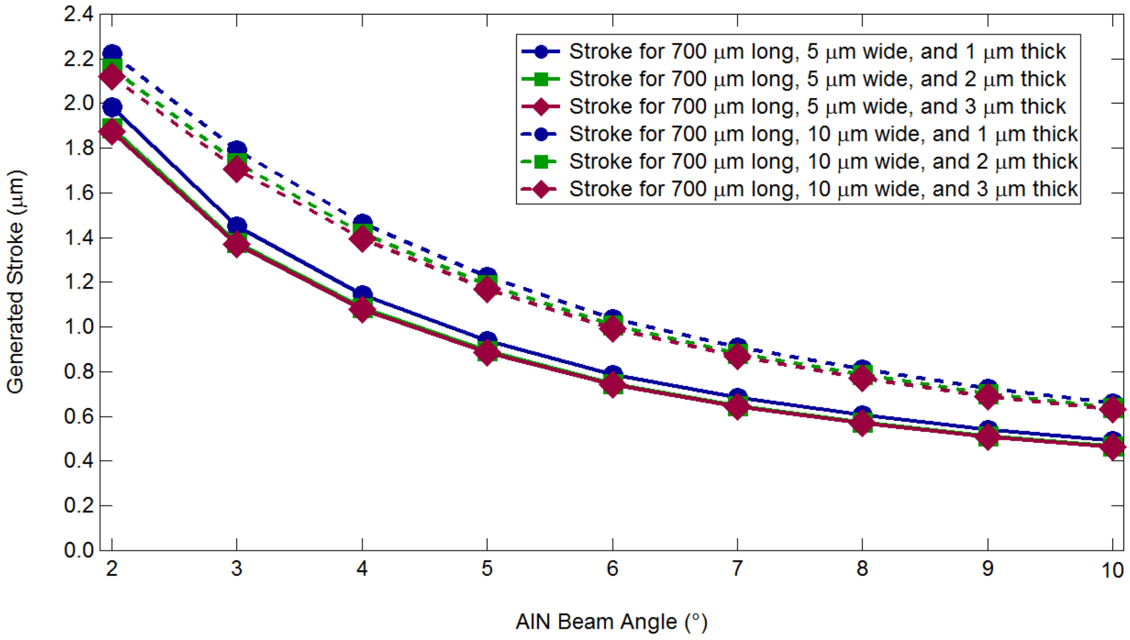

**Fig. 45. Generated stroke of non-self-alignment bottom electrode for 700 µm long AlN beam with different beam width and different beam angle.**

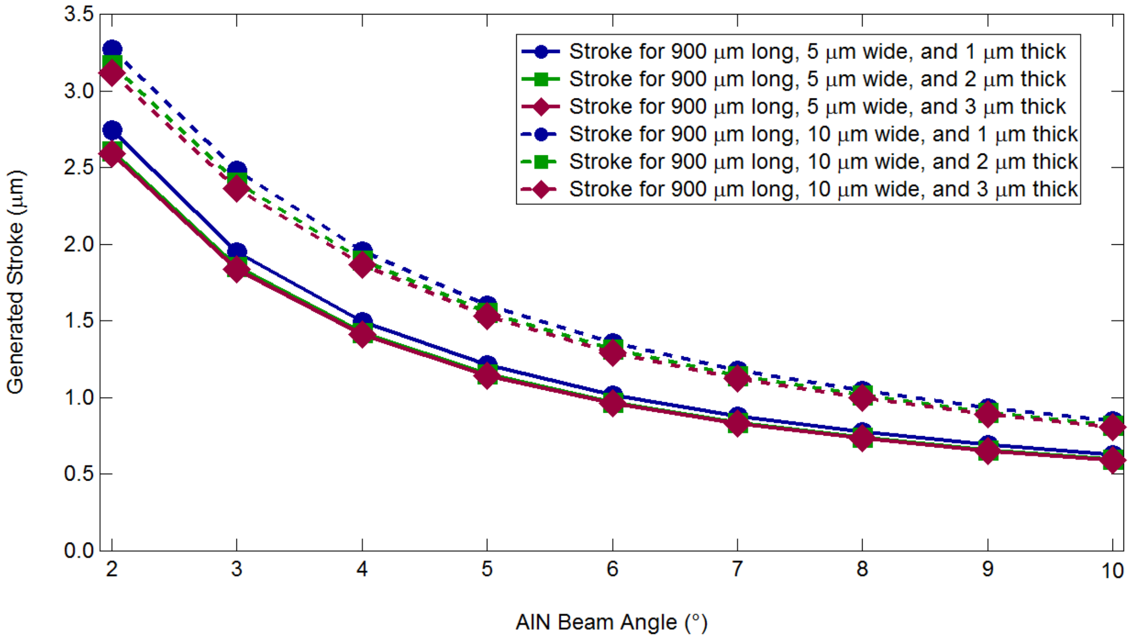

**Fig. 46. Generated stroke of non-self-alignment bottom electrode for 900 µm long AlN beam with different beam width and different beam angle.**

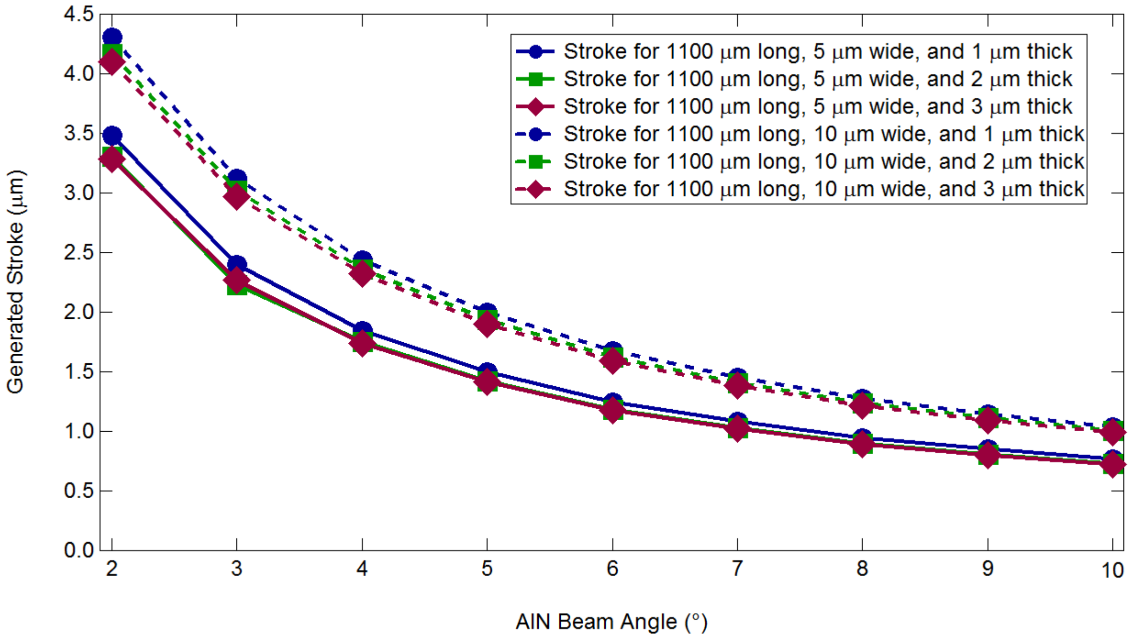

Fig. 47. Generated stroke of non-self-alignment bottom electrode for 1100 µm long AlN beam with different beam width and different beam angle.

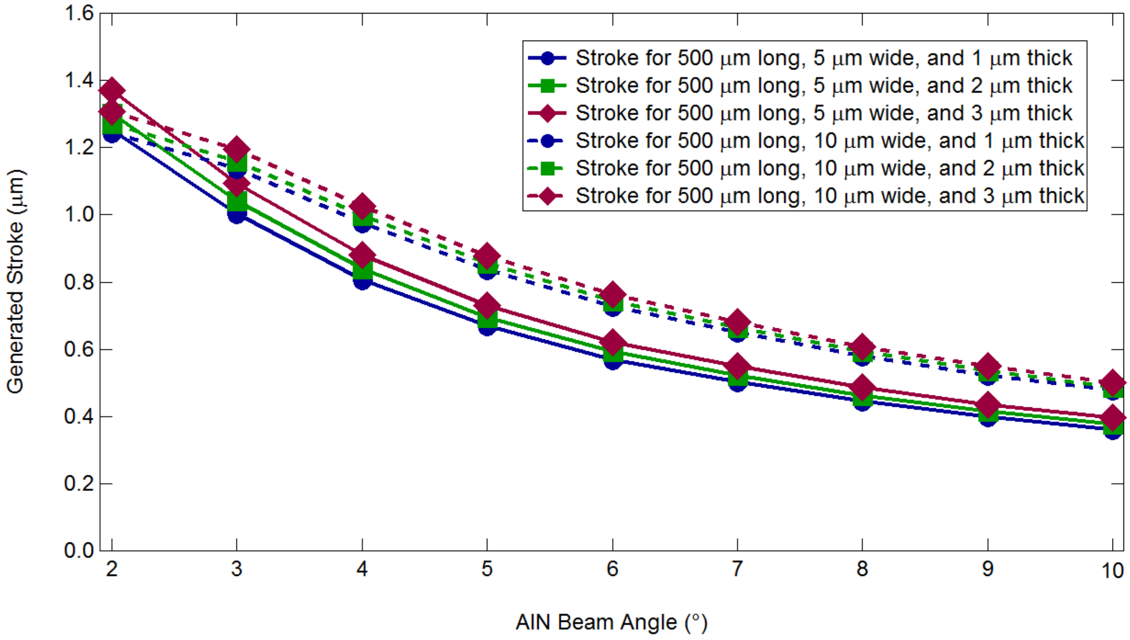

Fig. 48. Generated stroke of self-alignment bottom electrode for 500 µm long AlN beam with different beam width and different beam angle.

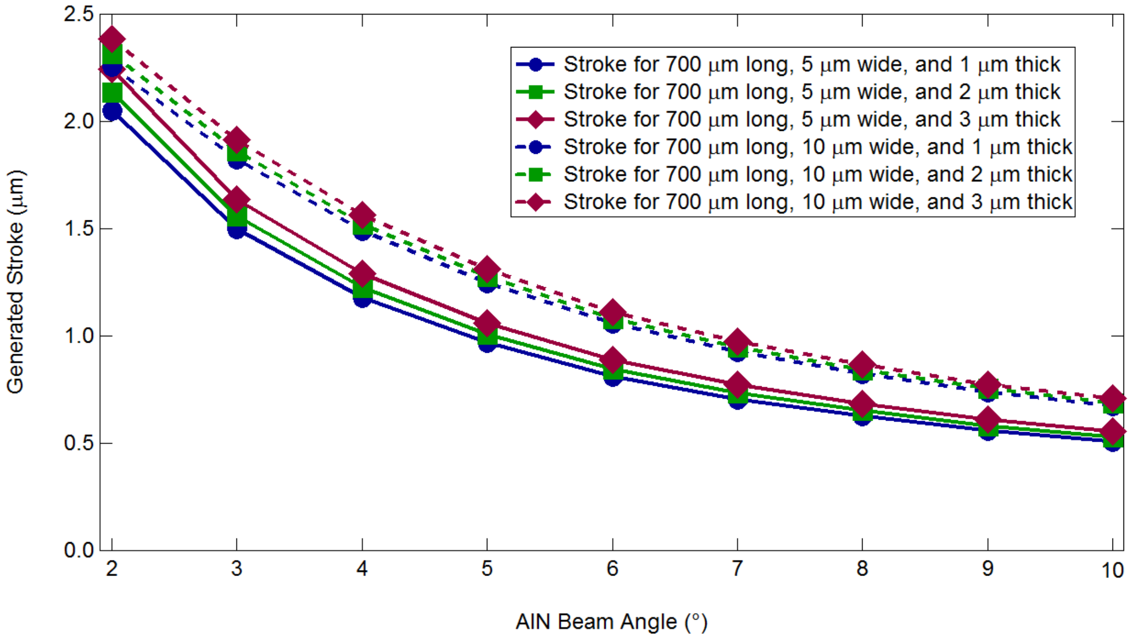

**Fig. 49. Generated stroke of self-alignment bottom electrode for 700 µm long AlN beam with different beam width and different beam angle.**

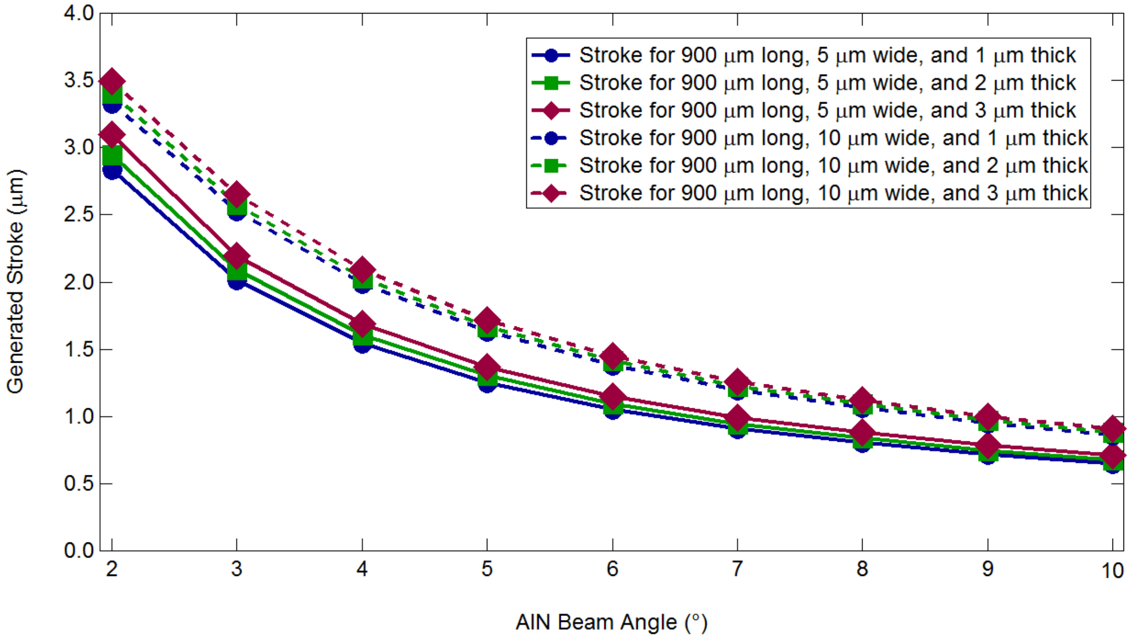

**Fig. 50. Generated stroke of self-alignment bottom electrode for 900 µm long AlN beam with different beam width and different beam angle.**

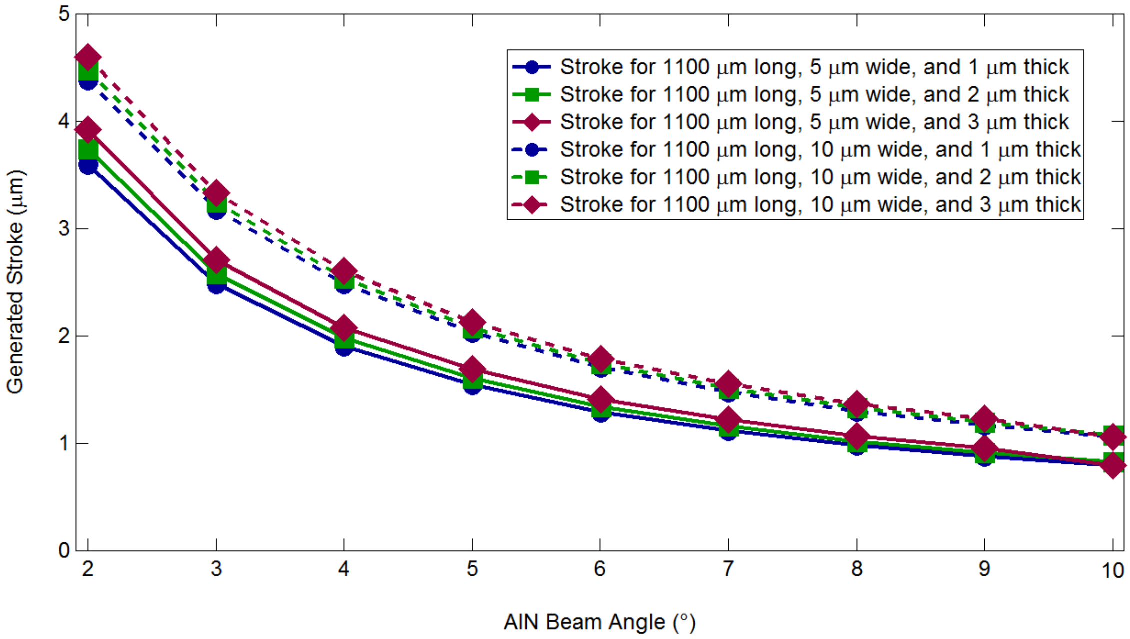

**Fig. 51. Generated stroke of self-alignment bottom electrode for 1100 µm long AlN beam with different beam width and different beam angle.**

Fig. 54 to Fig. 56 can be used to verify the influence of non-uniform electrical field. The electrical field distribution along cross sections for devices with fully-covered top/bottom electrode (as shown in Fig. 54), self-alignment bottom electrode (as shown in Fig. 55), and non-self-alignment bottom electrode (as shown in Fig. 56) from ANSYS simulation. From Fig. 54 to Fig. 56, we know the electrical field is the most uniform when the AlN beam is covered by both top electrode and bottom electrode (fully-covered top/bottom electrode, ideal device), and the less uniform one is when the AlN beam is only fully-covered by bottom electrode (self-alignment bottom electrode, actual device). The worst one will be the one neither fully-top electrode nor fully-bottom electrode covered (non-self-alignment bottom electrode, actual device). And these different is very apparent near the edge of the AlN beam and then reduce the generated stroke because of the uniform electric field the edge of the AlN beam (as shown in Fig. 54, Fig. 55, and Fig. 56).

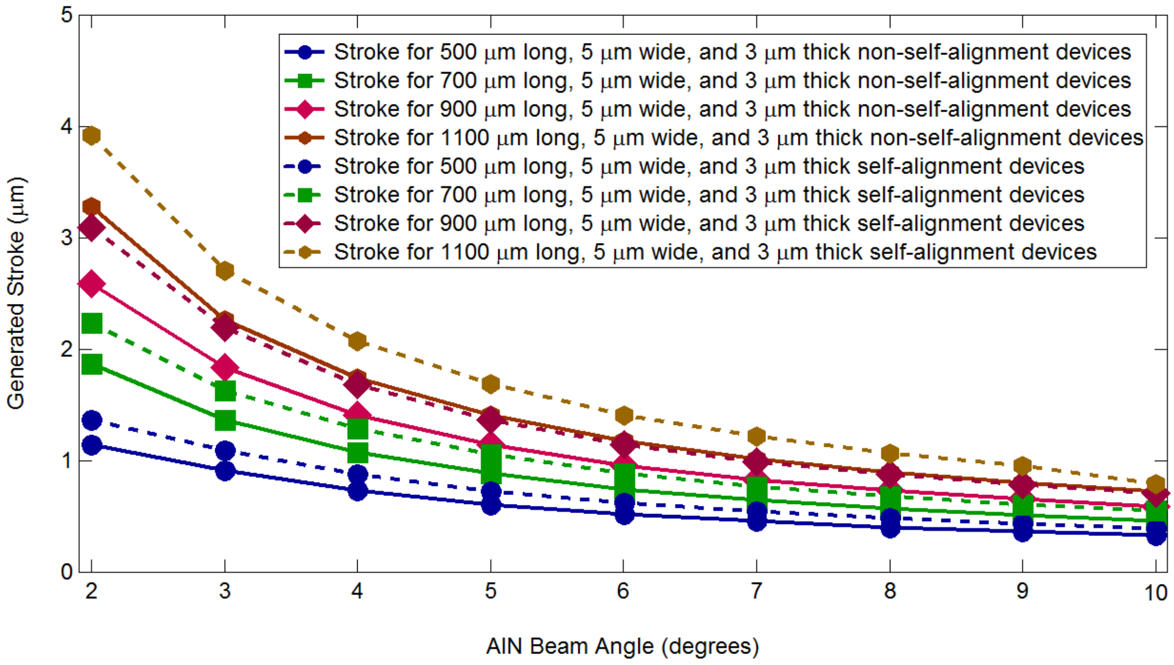

**Fig. 52. Generated stroke of non-self-alignment and self-alignment bottom electrode for different AlN beam, different beam width, and different beam angle.**

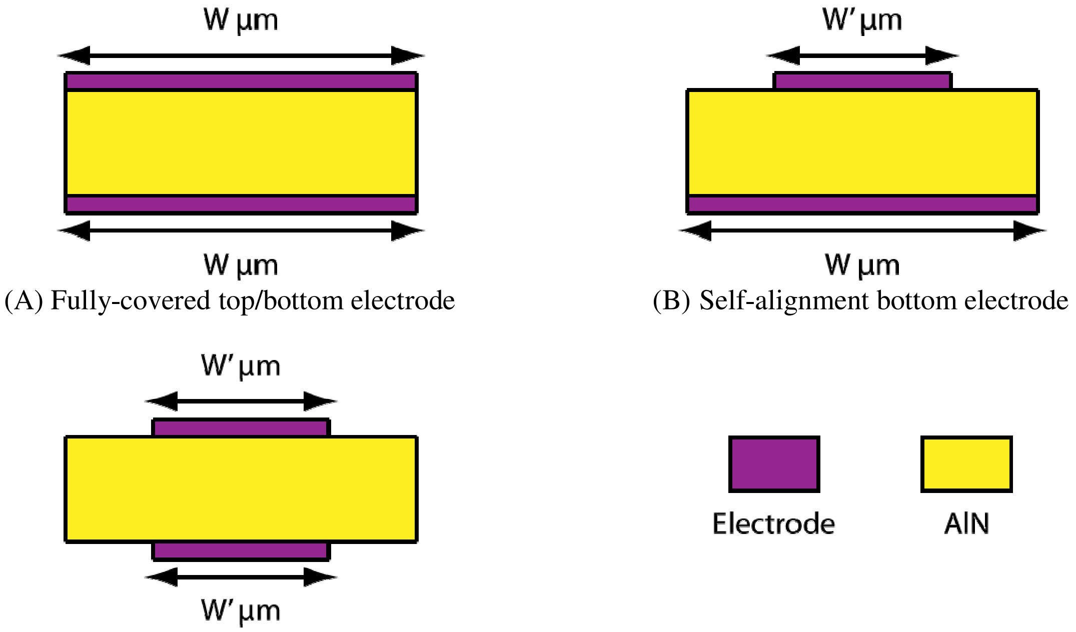

(A) Fully-covered top/bottom electrode

(B) Self-alignment bottom electrode

(C) Non-self-alignment bottom electrode

**Fig. 53. Sketch for devices with fully-covered top/bottom electrode, devices with self-alignment bottom electrode, and devices with non-self-alignment bottom electrode.**

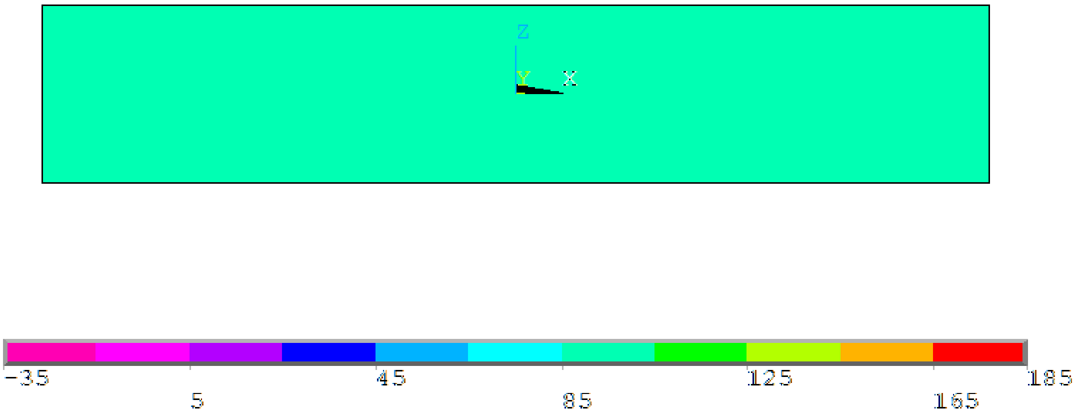

**Fig. 54.** **The distribution of electric fiend in the cross section of the AlN beam with fully-covered top/bottom electrode. The thickness and width of the AlN are 3 µm and 16 µm. The applied electrical field on the beam is 100 V/µm. The top electrode coverage width (W') and the AlN beam width (W) are all 16 µm in this simulation.**

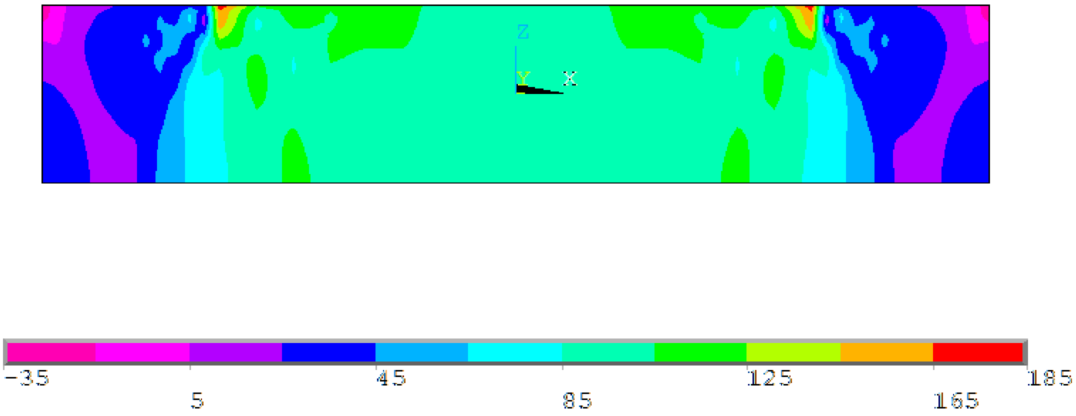

**Fig. 55.** **The distribution of electric fiend in the cross section of the AlN beam with self-alignment bottom electrode. The thickness and width of the AlN are 3 µm and 16 µm. The applied electrical field on the beam is 100 V/µm. The top electrode coverage width (W') and the AlN beam width (W) are 10 µm and 16 µm in this simulation.**

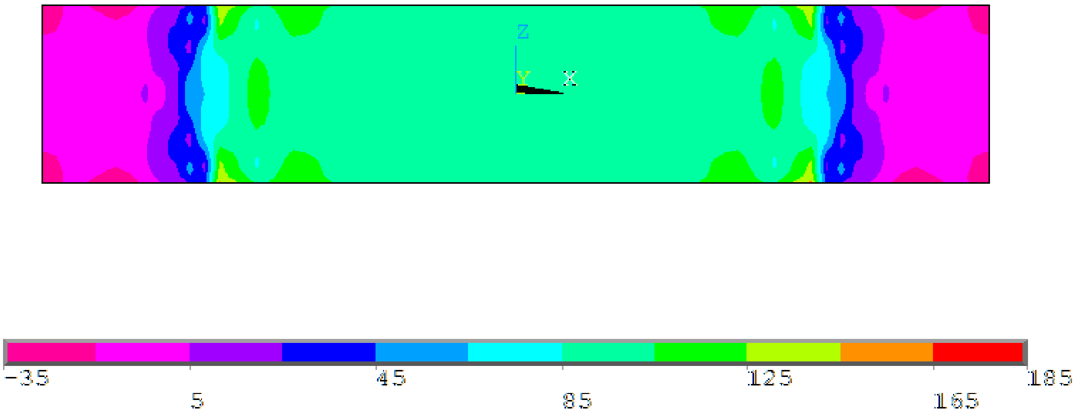

**Fig. 56. The distribution of electric fiend in the cross section of the AlN beam with non-self-alignment bottom electrode. The thickness and width of the AlN are 3 µm and 16 µm. The applied electrical field on the beam is 100 V/µm. The top electrode coverage width (W') and the AlN beam width (W) are all 10 µm in this simulation.**

## 3.5 Generated Force Simulation for Bi-Chevron Actuator Design with ANSYS

The generated force of devices with non-self-alignment bottom electrode for 500 µm long AlN beam, 700 µm long AlN beam, 900 µm long AlN beam, and 1100 µm long AlN beam with different beam width, different beam angle, and different beam thickness is as shown in Fig. 57, Fig. 58, Fig. 59, and Fig. 60. In these figures, the applied electrical field is kept at 100 volt/µm for all devices. And the generated force of devices with self-alignment bottom electrode is as shown in Fig. 61, Fig. 62, Fig. 63, and Fig. 64. From Fig. 57 to Fig. 64, we can evaluate the influence of AlN beam length, AlN beam width, AlN beam angle, and AlN beam thickness on generated force on the generated force:

A. The AlN beam angle will influence the generated force. Generated force will increase when AlN beam angle increases. This is the same as what is predicated in Equation (3.10).
B. The AlN beam width will influence the generated force. Generated force will increase when AlN beam width increases. This is the same as what is predicated in Equation (3.10).

C. The AlN beam thickness will influence the generated force. Generated force will increase when AlN beam thickness increases. This is the same as what is predicated in Equation (3.10).
D. The AlN beam length will have small influence on the generated stroke.

And the comparison of devices with self-alignment bottom electrodes and devices with non-self-alignment bottom electrodes is as shown in Fig. 65. The difference of generated force between device with self-alignment bottom electrodes and device with non-self-alignment bottom electrodes is due the uniform electrical field (as shown in Fig. 54 to Fig. 56), too.

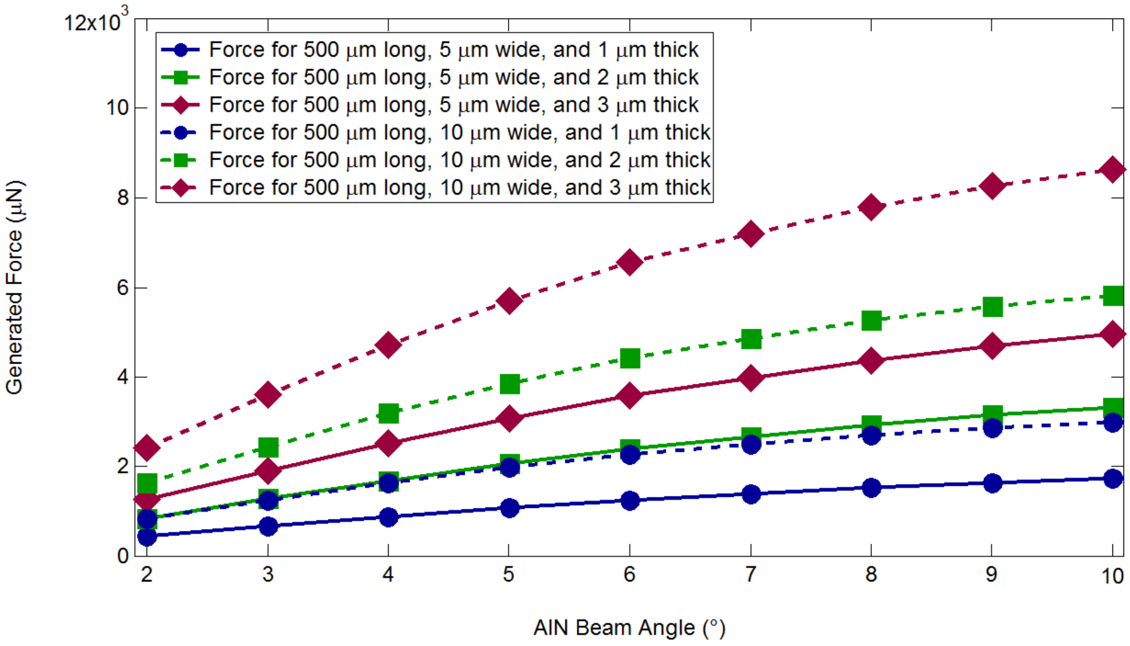

**Fig. 57. Generated force of non-self-alignment bottom electrode for 500 μm long AlN beam with different beam width and different beam angle.**

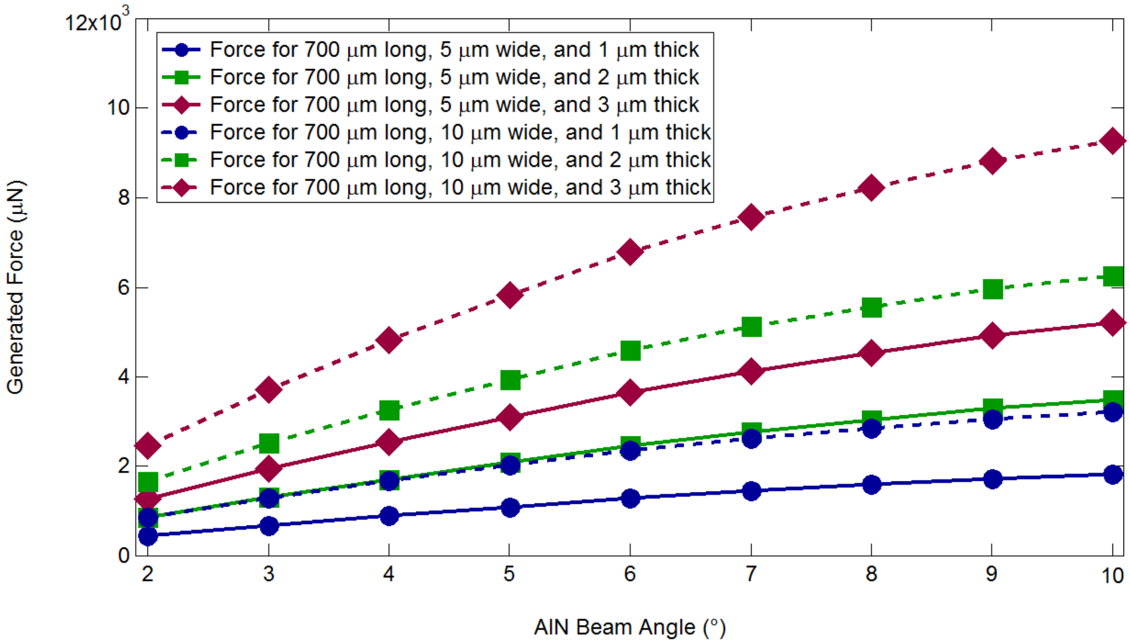

**Fig. 58. Generated force of non-self-alignment bottom electrode for 700 µm long AlN beam with different beam width and different beam angle.**

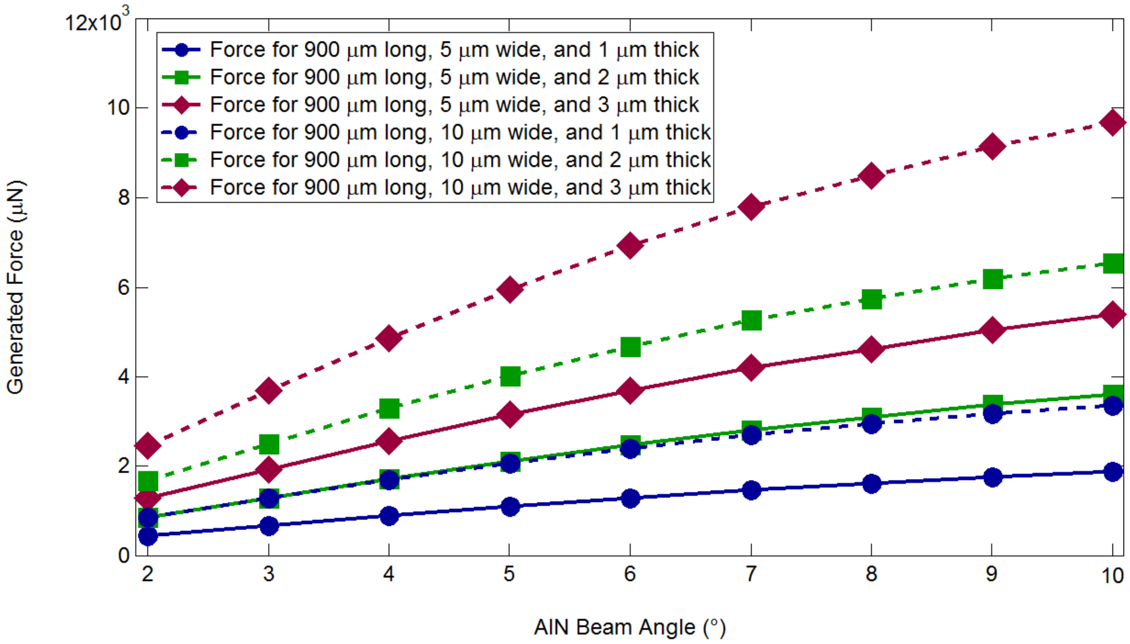

**Fig. 59. Generated force of non-self-alignment bottom electrode for 900 µm long AlN beam with different beam width and different beam angle.**

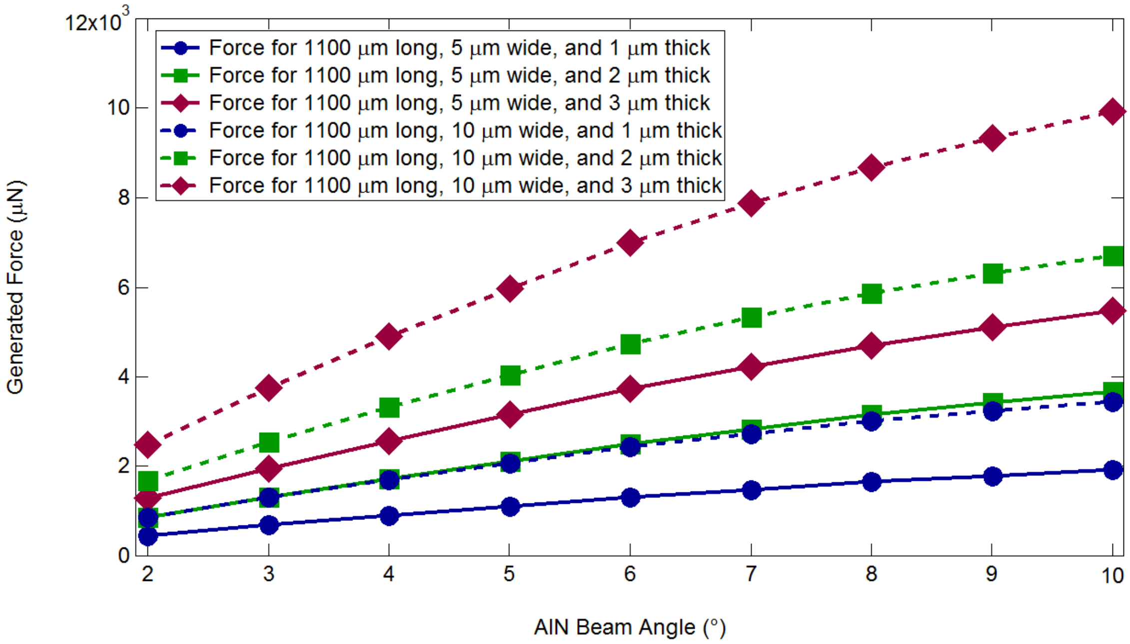

**Fig. 60. Generated force of non-self-alignment bottom electrode for 1100 µm long AlN beam with different beam width and different beam angle.**

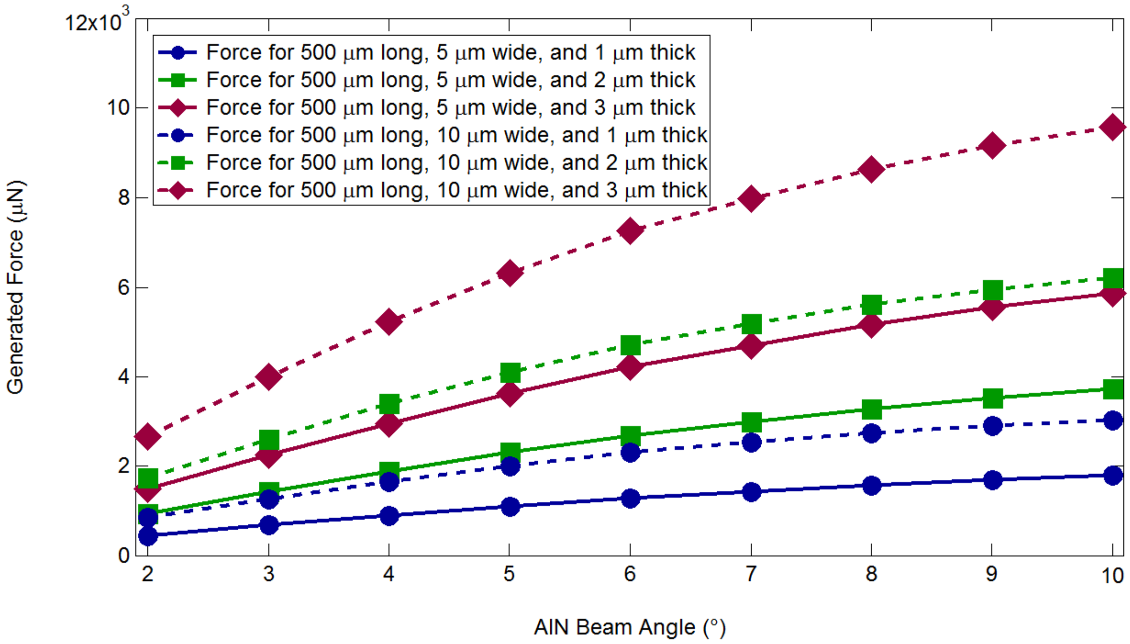

**Fig. 61. Generated force of self-alignment bottom electrode for 500 µm long AlN beam with different beam width and different beam angle.**

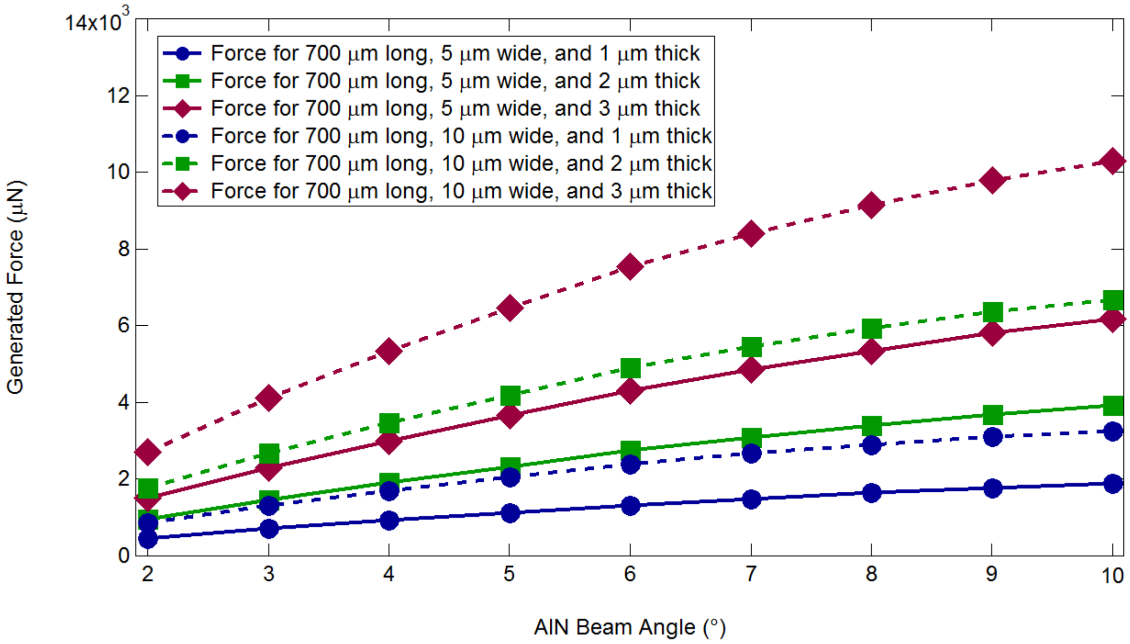

**Fig. 62.** Generated force of self-alignment bottom electrode for 700 μm long AlN beam with different beam width and different beam angle.

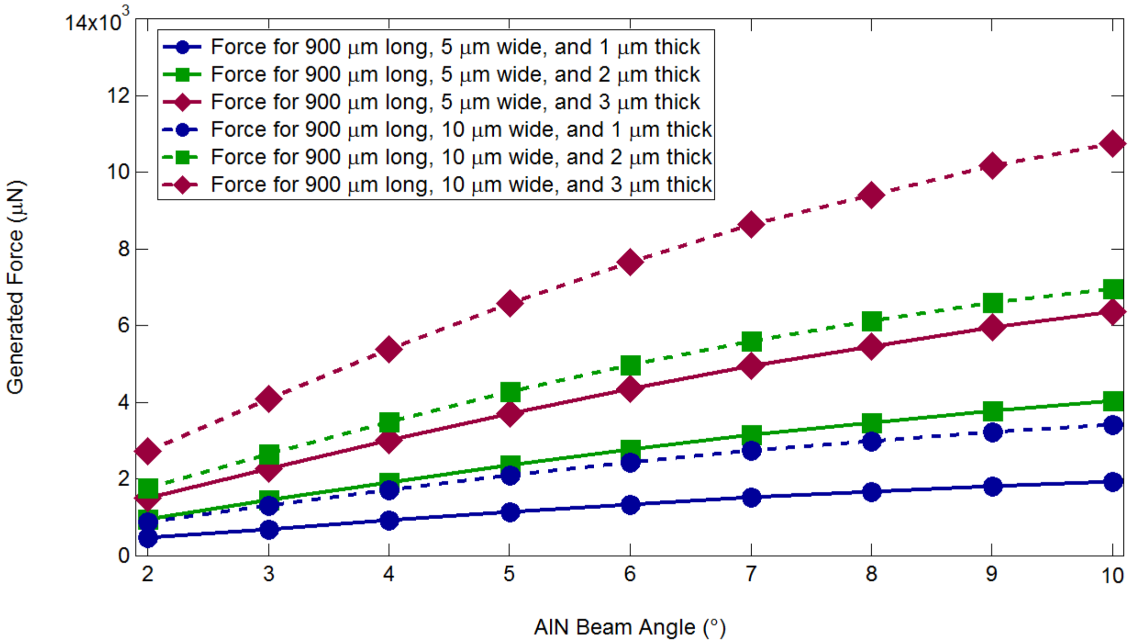

**Fig. 63.** Generated force of self-alignment bottom electrode for 900 μm long AlN beam with different beam width and different beam angle.

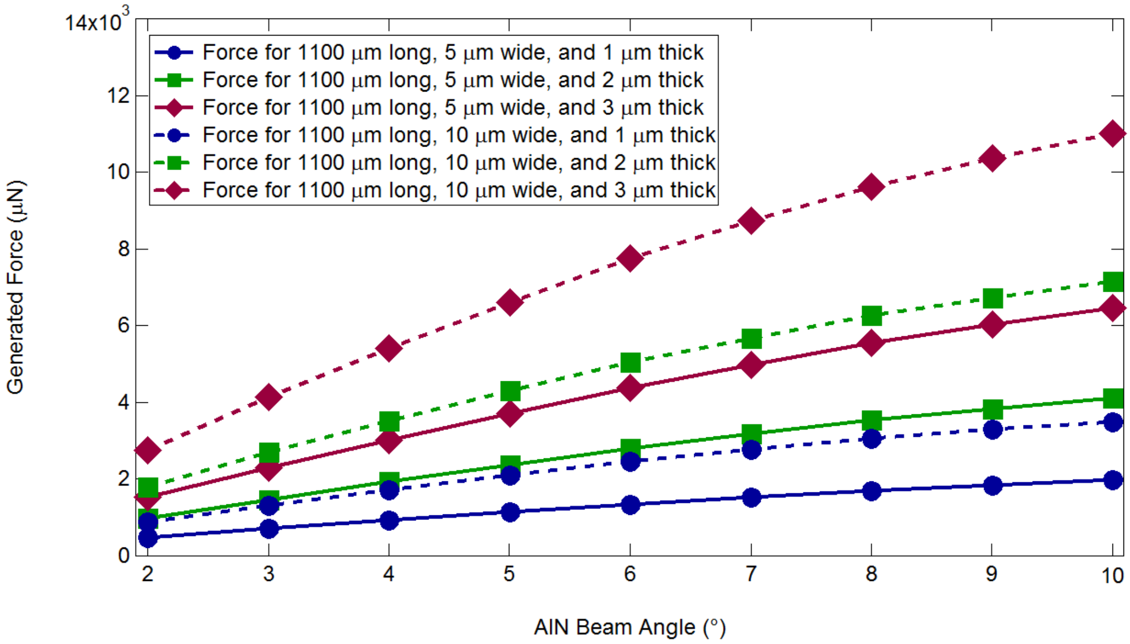

**Fig. 64. Generated force of self-alignment bottom electrode for 1100 µm long AlN beam with different beam width and different beam angle.**

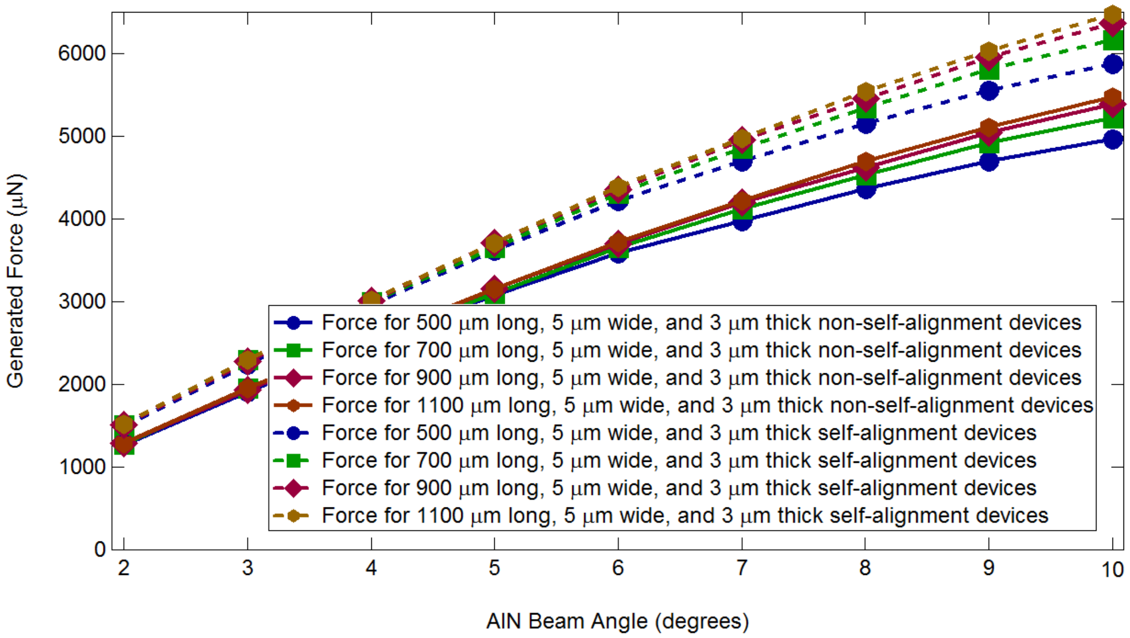

**Fig. 65. Generated force of non-self-alignment and self-alignment bottom electrode for different AlN beam, different beam width, and different beam angle.**

## 3.6 Resonant Frequency Simulation for Bi-Chevron Actuator Design with ANSYS

The $1^{st}$ in-plane resonant frequency (as shown in Fig. 66) and the $2^{nd}$ in-plane resonant frequency (as shown in Fig. 67) for 500 µm long AlN beam, 700 µm long AlN beam, 900 µm long AlN beam, and 1100 µm long AlN beam with different beam width, different beam angle, and different beam thickness are as shown from Fig. 68 to Fig. 75. And the plots that show more comparison between the effect of beam length, beam width, and beam angle are as shown in Fig. 76 and Fig. 77. From Fig. 68 to Fig. 77, we can evaluate the influence of AlN beam length, AlN beam width, AlN beam angle, and AlN beam thickness on $1^{st}$ in-plane resonant frequency and $2^{nd}$ in-plane resonant frequency and the influence of the geometry are summarized as following:

A. The in-plane resonant frequency is not influenced by the top/bottom electrode coverage since the FEM simulation doesn't include the top electrode and bottom electrode into the calculation.
B. The AlN beam angle will influence the in-plane resonant frequency. In-plane resonant frequency will increase when AlN beam angle increases. And the in-plane resonant frequency will saturate at certain value while the beam angle keeps on increasing.
C. The AlN beam width will influence the in-plane resonant frequency. In-plane resonant frequency will increase when AlN beam width increases.
D. The AlN beam thickness will not influence the in-plane resonant frequency.
E. The AlN beam length will have hug influence on in-plane resonant frequency. In-plane resonant frequency will decrease when AlN beam lenght increases.

About the influence of the AlN beam thickness for the in-plane resonant frequency, it is can be explained by the following equation that used to evaluate the $1^{st}$ in plane resonant frequency frequently in solid mechanics [100]:

$$f = \frac{1}{2\pi}\sqrt{\frac{8EI}{\rho AL}} \tag{3.13}$$

where E is the Young's modulus of object, ρ is the density of the object, I is the moment of the inertia, L is the beam length, A is the area of the cross section of the object, and π is a mathematical constant whose value is the ratio of any Euclidean plane circle's circumference to its diameter. For the in-plane vibration, the moment of the inertia (I) and the area of the cross section (A) can be written as the following equations:

$$I = \frac{tw^3}{12} \tag{3.14}$$

And

$$A = t \times w \tag{3.15}$$

where t is the beam thickness, and w is the beam width. If we combine Equation (3.13) to (3.15), the following equation can be used to calculate the 1st in-plane resonant frequency of a cantilever beam:

$$f = \frac{1}{2\pi}\sqrt{\frac{2Ew^2}{3\rho L}} \tag{3.16}$$

From Equation (3.16), we can see the thickness (t) of the cantilever beam has no effect on the in-plane resonant frequency of the cantilever beam. That is why in our FEM simulation, the bi-chevron AlN actuators with different beam thickness (the same beam length and the same beam width) have the same in-plane resonant frequency.

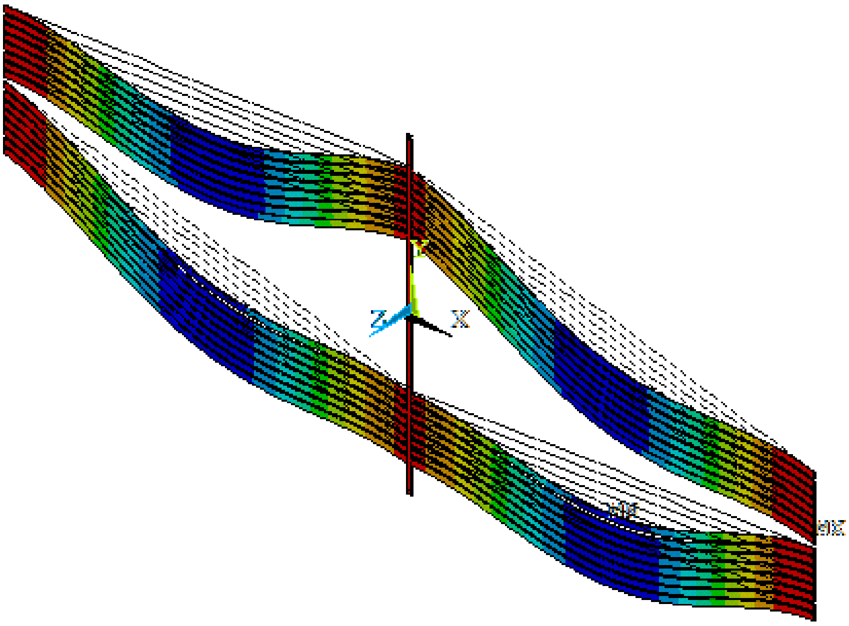

Fig. 66. Mode shape of the bi-chevron AlN Actuator at first in-plane resonant frequency

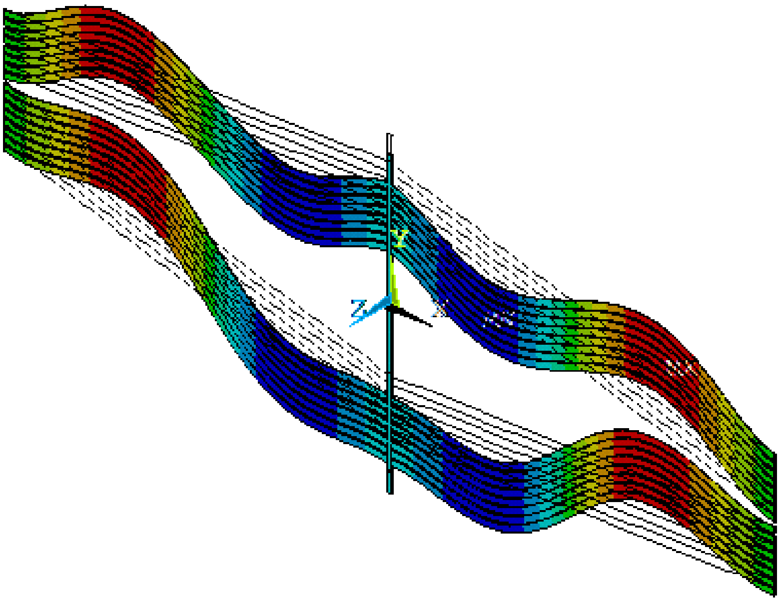

Fig. 67. Mode shape of the bi-chevron AlN Actuator at second in-plane resonant frequency

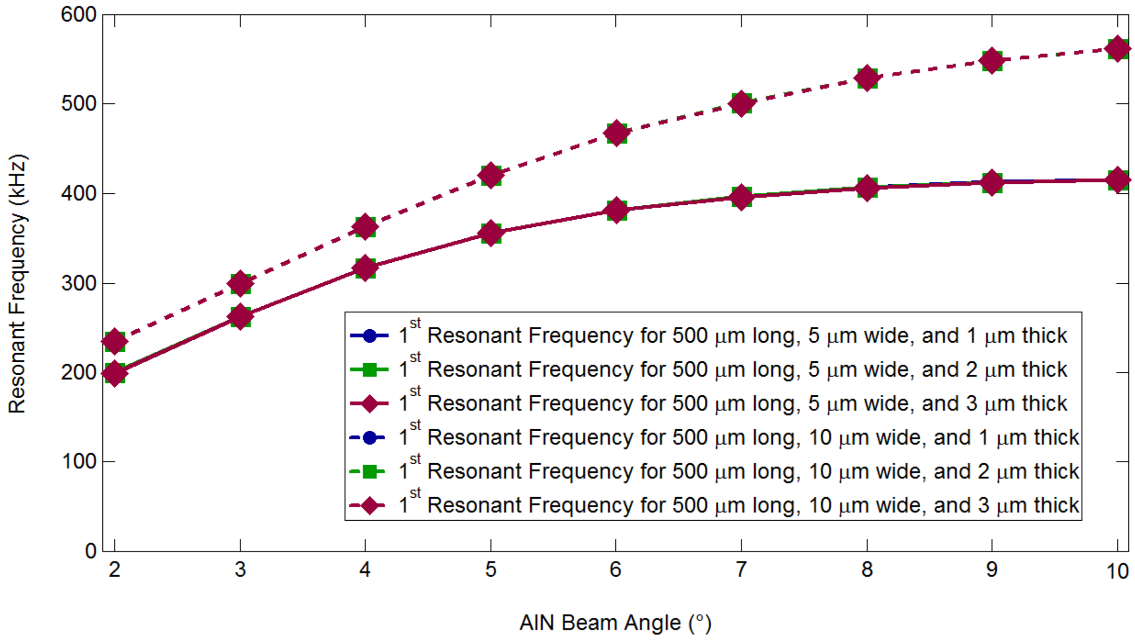

Fig. 68. First in-plane resonant frequency for 500 μm long AlN beam with different beam width and different beam angle.

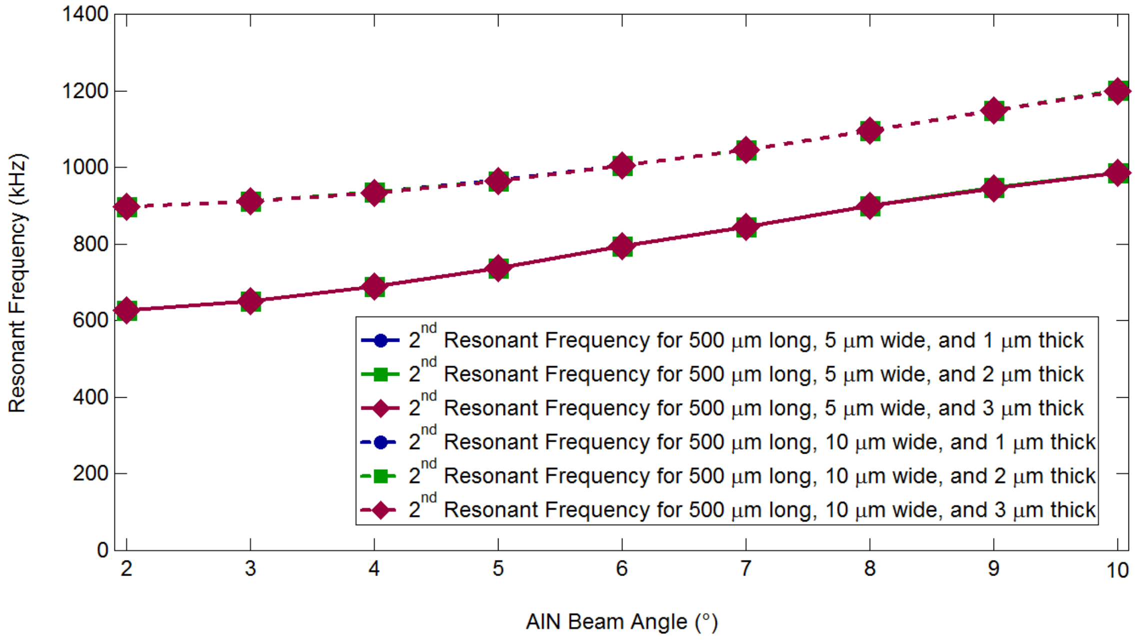

**Fig. 69. Second in-plane resonant frequency for 500 μm long AlN beam with different beam width and different beam angle.**

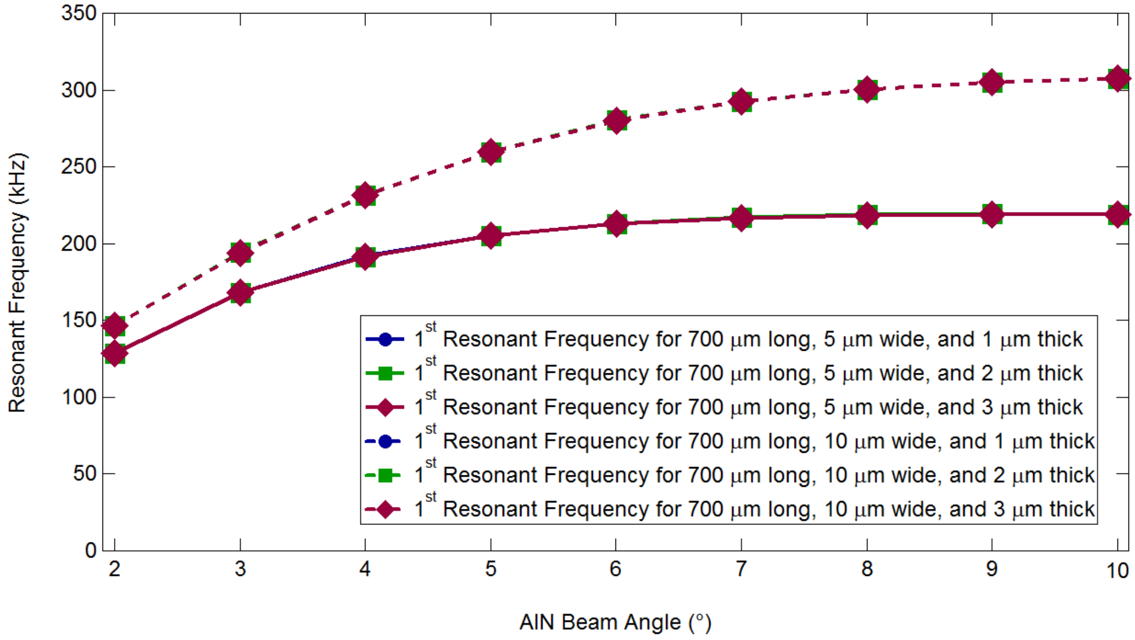

**Fig. 70. First in-plane resonant frequency for 700 μm long AlN beam with different beam width and different beam angle.**

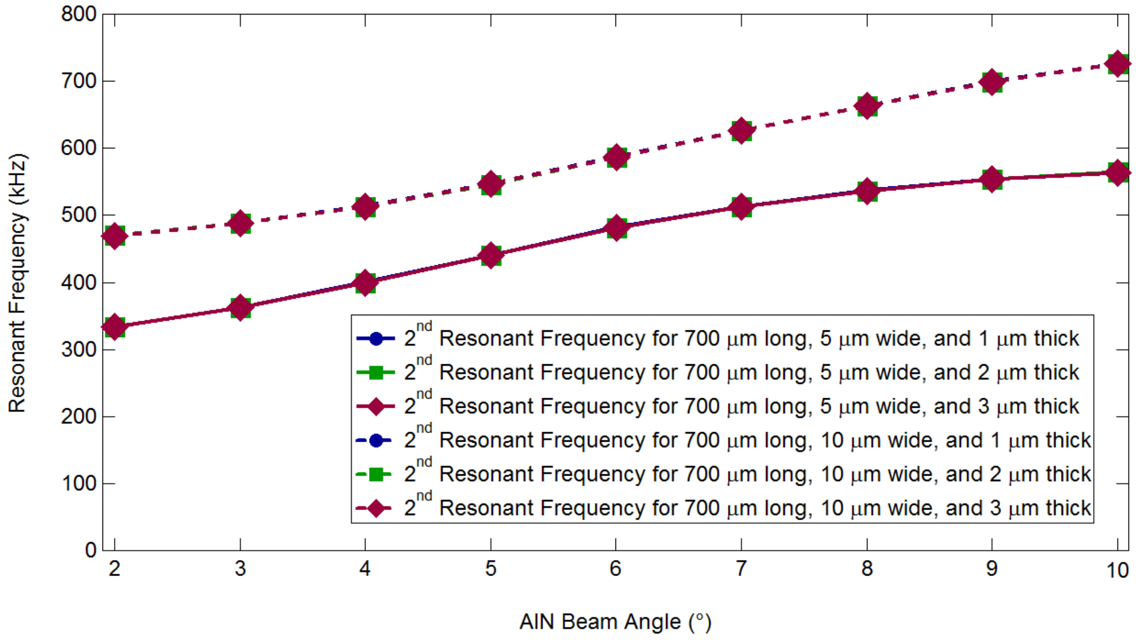

**Fig. 71. Second in-plane resonant frequency for 700 μm long AlN beam with different beam width and different beam angle.**

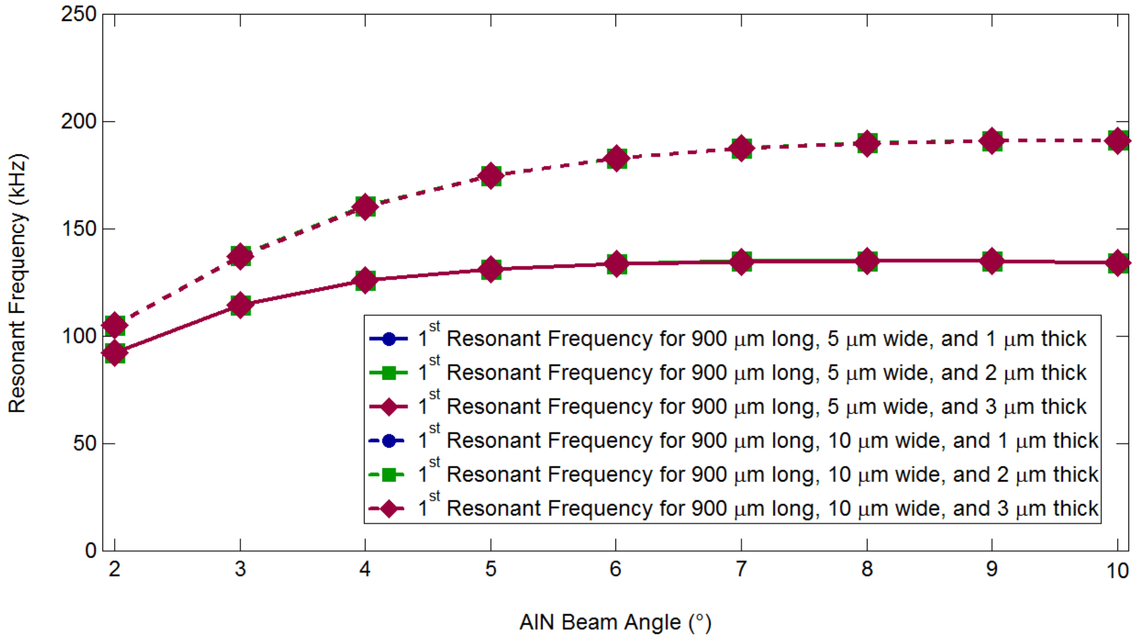

**Fig. 72. First in-plane resonant frequency for 900 μm long AlN beam with different beam width and different beam angle.**

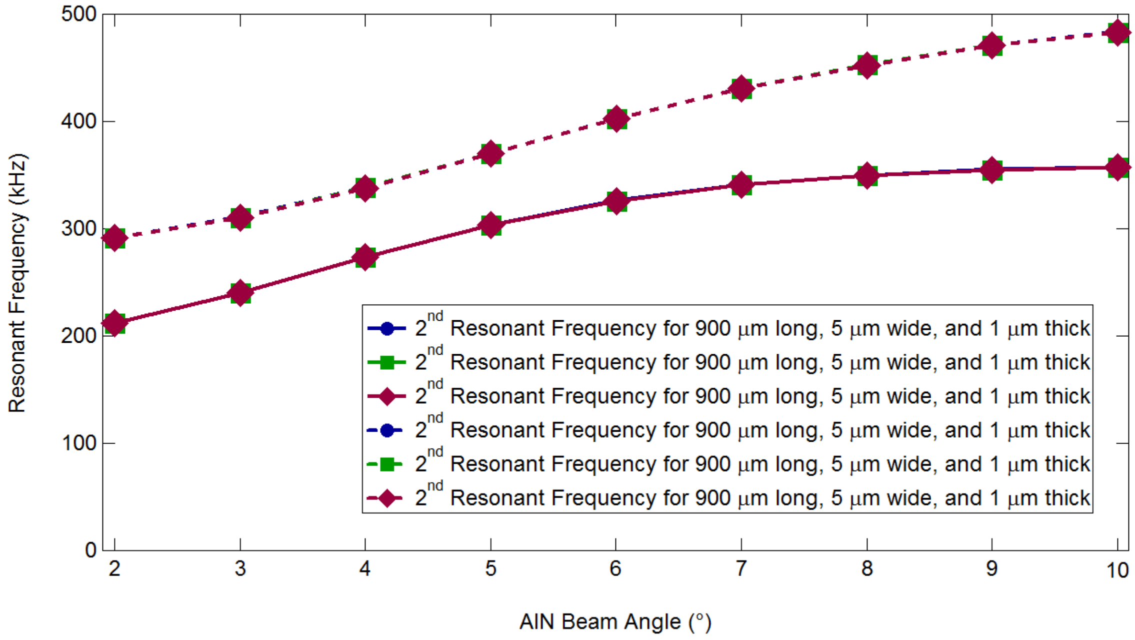

Fig. 73. Second in-plane resonant frequency for 900 μm long AlN beam with different beam width and different beam angle.

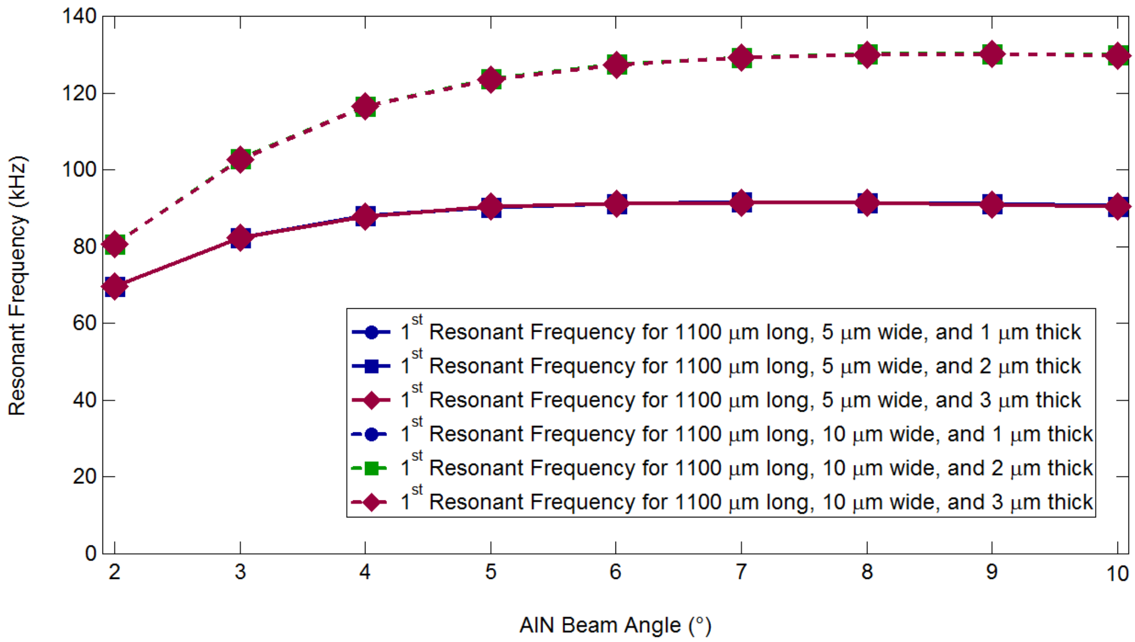

Fig. 74. First in-plane resonant frequency for 1100 μm long AlN beam with different beam width and different beam angle.

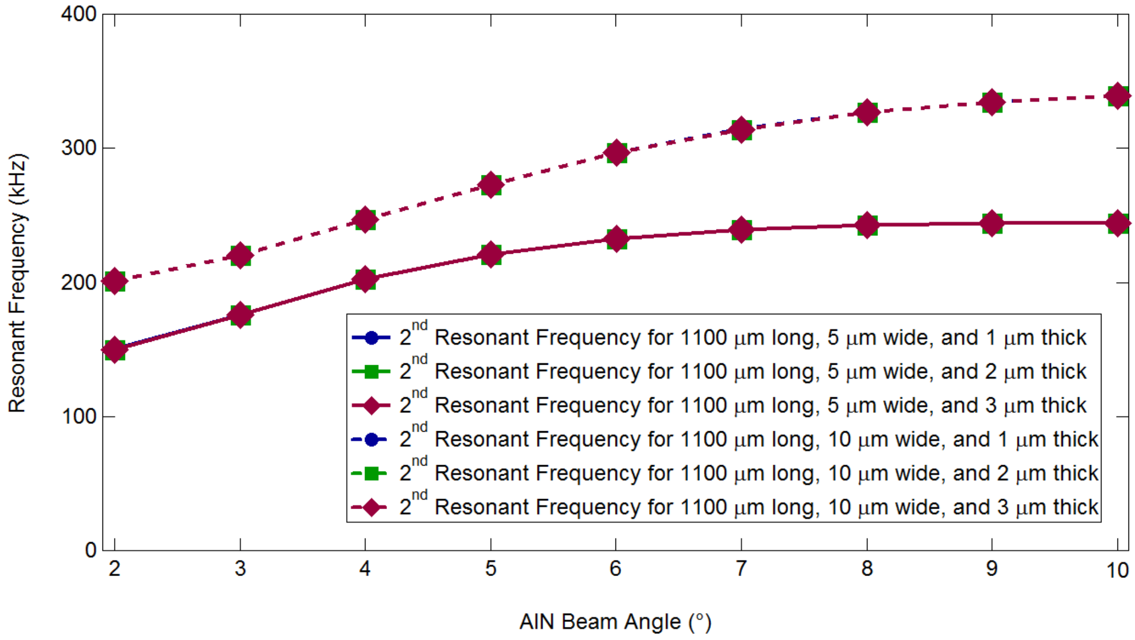

**Fig. 75. Second in-plane resonant frequency for 1100 μm long AlN beam with different beam width and different beam angle.**

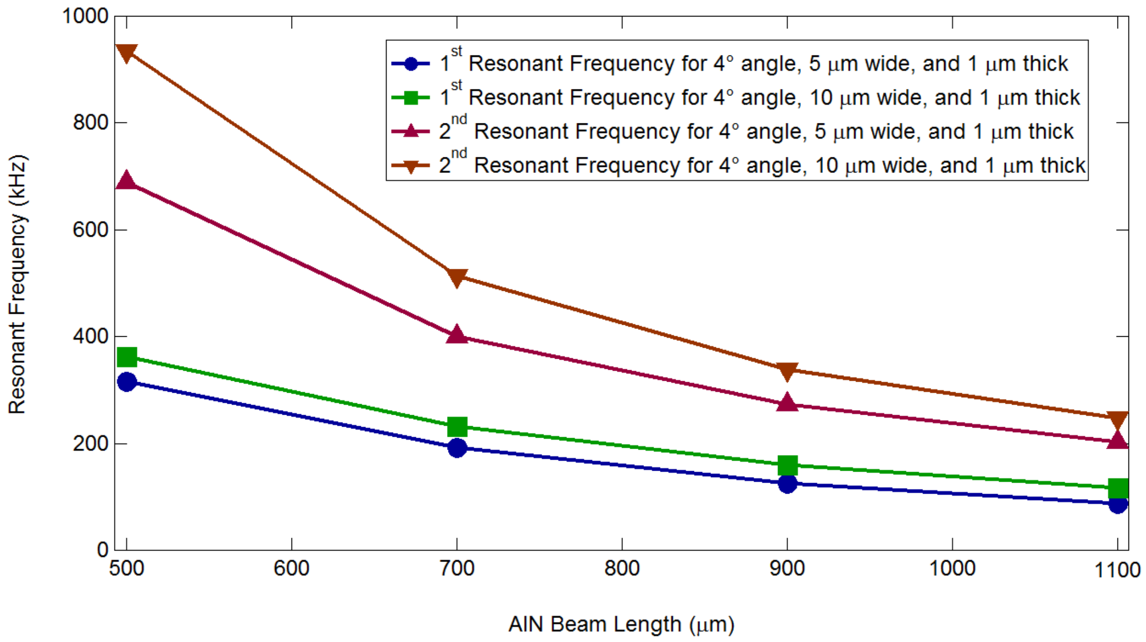

**Fig. 76. In-plane resonant frequency for different beam length and the same beam width for the same beam angle (4°).**

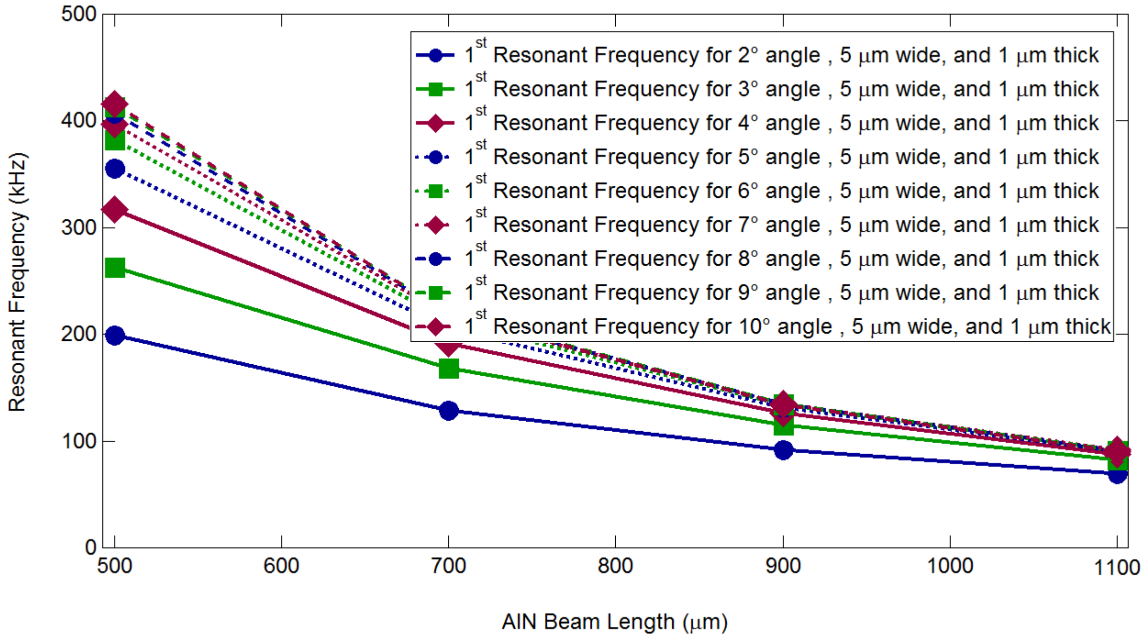

**Fig. 77. In-plane resonant frequency for different beam length and the same beam angle for the same beam width (5μm).**

# Chapter 4 Fabrication Process of Pre-Prototype Device and Prototype Device for Supercritical Carbon Dioxide Valve

Before the fabrication process for our goal device, the working function of the key component, bi-chevron AlN actuator, in the SCV design should be proven. In order to achieve this, we would like to introduce two different devices that can be used to verify the working function and fabrication process of the supercritical carbon-dioxide valve design: pre-prototype device (as shown in Fig. 78 (A)) and prototype devices (Fig. 78 (B)).

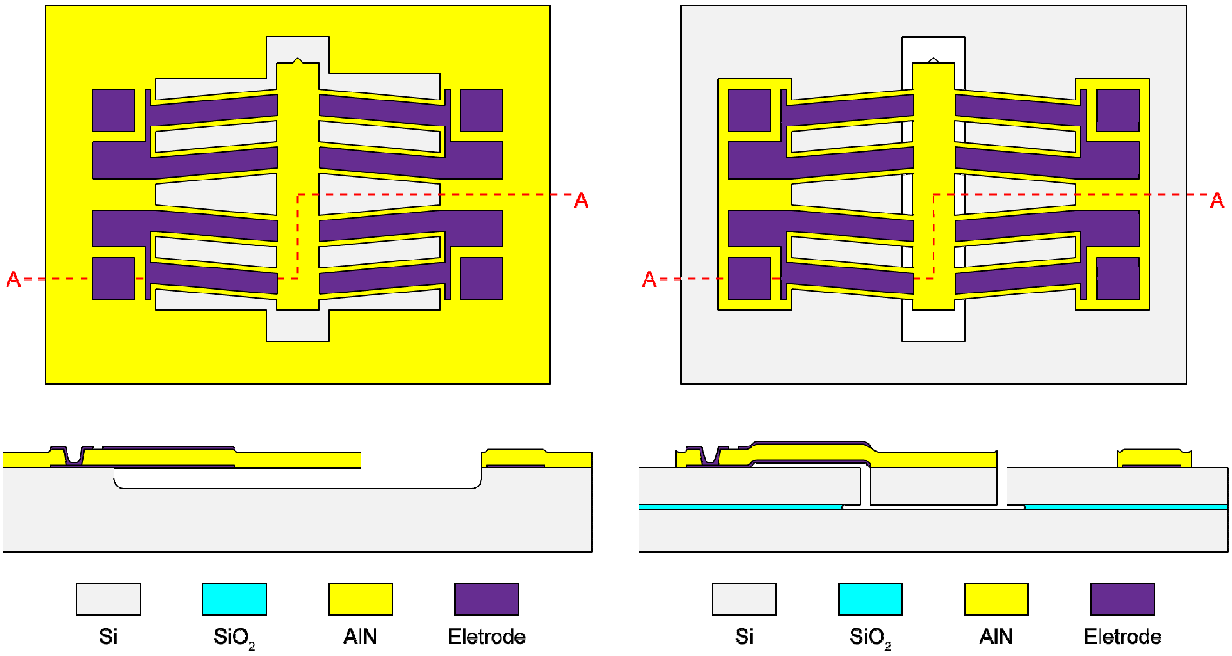

(A) Pre-Prototype Device (B) Prototype Device

Fig. 78. Sketch of pre-prototype device and prototype device.

There are two major differences between the pre-prototype device and prototype device and these differences are:

1. *<u>Composition of the movement part</u>*: For the pre-prototype devices, the moving part is composed only of AlN. And for the prototype devices, the moving part is composite both of AlN and silicon. Due to this reason, the pre-prototype is only an actuator and doesn't function as a valve. So in our approach, the pre-prototype device will be fabricated first to verify the design idea and working function of the bi-chevron AlN actuator. Once it is done, the prototype devices can be fabricated and this prototype device can become SCV after sealed with a cap.

2. *Releasing method*: The pre-prototype device is released by isotropic silicon substrate etch with xenon difluoride gas ($XeF_2$). However, the prototype device is released by silicon dioxide etch ($SiO_2$) with vapor hydrofluoric acid (HF). This difference is made necessary by the use of silicon for the valve: $XeF_2$ would attach the valve component.

Due to the different design goal, the fabrication process for pre-prototype devices and prototype devices will be dissimilar. In addition, there will be some different design considerations for these two different fabrication processes. The detail about these differences of the fabrication process and the design consideration will be discussed more in the following sections.

## 4.1 Fabrication Process for Pre-Prototype Device

To fabricate the pre-prototype device, a very stable fabrication process developed by Piazza *et al*. [115] for AlN RF filter is used. This fabrication process for the pre-prototype device (as shown in Fig. 79 (A)) is started with a high-resistivity silicon substrate. First, the photoresist (PR) is deposited and defined for the following lift-off step of the bottom electrode aluminum (Al). After this step, the bottom electrode Al is deposited with s-gun sputtering and then the coming step is lift-off to get the pattern of the bottom electrode (as shown in as shown in Fig. 79 (B)).

Next, aluminum nitride (AlN) thin film can be deposited with AlN sputtering tool. And the stress of this AlN thin film should be controlled between 0~100 MPa tensile to avoid the buckling and breaking of the AlN beams since the pre-prototype device contains long and thin AlN beams and that makes the influence of the stress become significant. The stress control of AlN thin film can be adjusted by changing the Ar flow rate, $N_2$ flow rate, or sputtering power [98-104]. In addition to the stress control, the process parameter of AlN thin deposition should be optimized to get the best crystal orientation (higher piezoelectric coefficient) for the goal of better performance, generated stroke and generated force. The quality of the crystal orientation of the AlN thin film can be determined the full width at half maximum (FWHM) value of the rocking curve from the x-ray diffractometer [102, 103, 104, 106, and 108] (XRD).

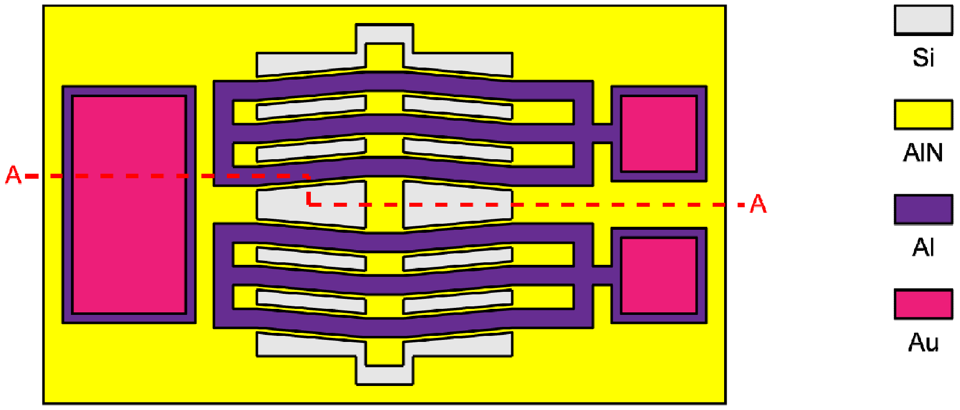

(A) Top view of the pre-prototype device

(B) Deposit and define the bottom electrode

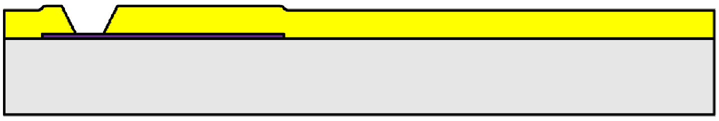

(C) Deposit and wet etch AlN for AlN via

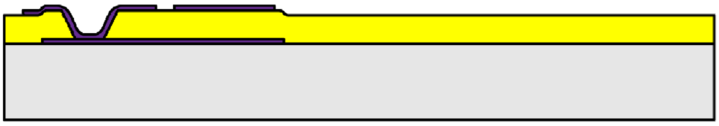

(D) Deposit and define the top electrode

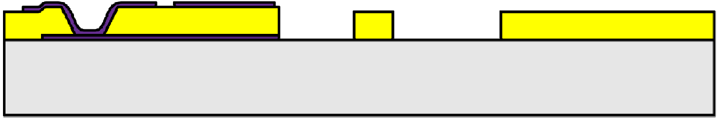

(E) Etch AlN to define the shape of the pre-prototype device

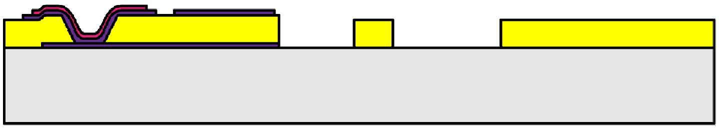

(F) Deposit and define a thick Au layer

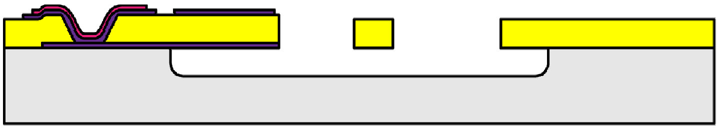

(G) Release the structure with isotropic silicon etch

**Fig. 79. Fabrication process of pre-prototype devices. (A) is the top view of the pre-prototype device after the fabrication process. (B)-(G) are the cross sections of the pre-prototype device during the fabrication process.**

After the AlN thin film is deposited, the AlN via will be defined to offer the connection between the bottom electrode and the top electrode (as shown in as shown in Fig. 79 (C)). The AlN via can be etched by immersing the wafer in 160 C hot phosphoric acid with oxide as the etch mask and then the oxide etch mask will be removed for the next step. Once the AlN via is defined, the top electrode will be defined by the PR lift-off method (as shown in Fig. 79 (D)). The top electrode Al film is deposited by s-gun sputtering, the same metal sputtering machine for the bottom electrode. One the top electrode is patterned, the AlN will be etched by plasma etch (Lam3 aluminum reactive ion etcher, RIE, by Lam Research) tool to get the outline of the AlN actuator (as shown in Fig. 79 (E)). The etch mask for this AlN dry tech is low-temperature oxide (LTO) since oxide etch mask gives a better AlN/$SiO_2$ selectivity than AlN/PR and generates a more steep side wall. The oxide etch mask for AlN etch can be removed by plasma etch (Lam2 oxide RIE by lam research) since the selectivity between oxide/AlN and oxide/Al is excellent.

Once the oxide etch mask for the AlN dry etch is removed, we can deposit and define a thick gold (Au) layer with lift-off method to cover the electrical pad and AlN via area (as shown in Fig. 79 (F)). This thick Au layer is used to reduce the resistivity near AlN via due to the poor step coverage of the top Al electrode on the AlN via part. As this step is finished, the finally step is to release the pre-prototype device with $XeF_2$ gas (as shown in Fig. 79 (G)).

In Fig. 80, there is a scanning electron microscope (SEM) image of a pre-prototype device from the fabrication process described as the previous section. The device in Fig. 80 has been released with $XeF_2$ gas. In each pre-prototype device, there is a built-in Vernier scale (as shown in Fig. 81). The built-in Vernier scale is used for the generated stroke measurement. Further details on the Veriner scale for generated stroke measurement will be discussed in the following sections.

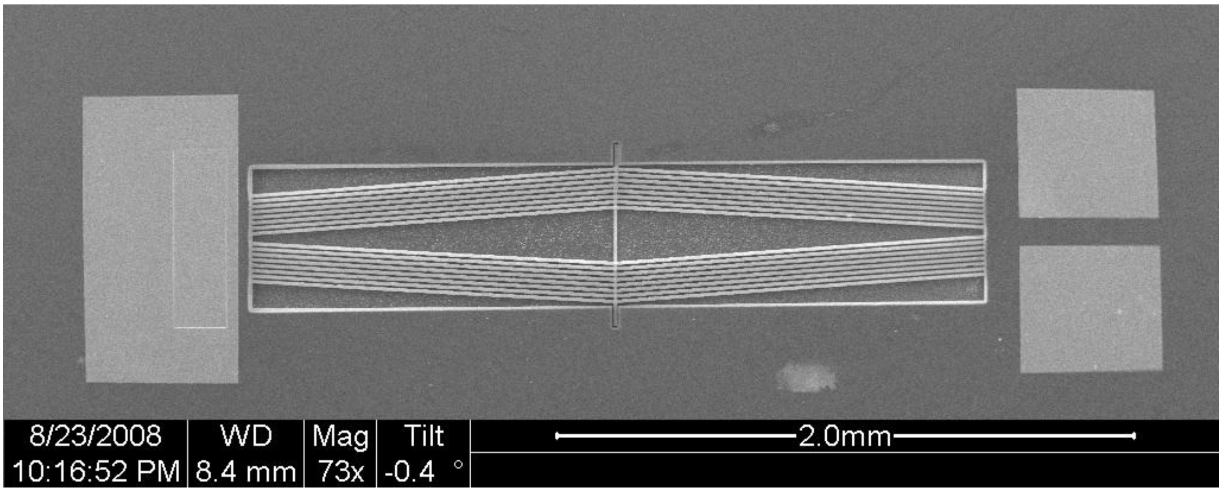

Fig. 80. SEM image of the pre-prototype device.

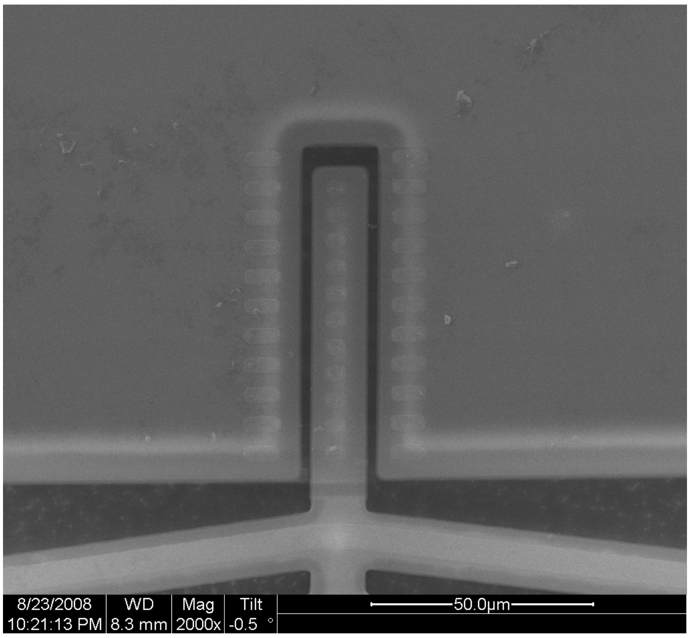

**Fig. 81. SEM of the Vernier scale on the pre-prototype device.**

## 4.2 Fabrication Process for Prototype Device and its Process Parameter

Since the working function of the pre-prototype devices is verified, the prototype device can be fabricated with the corresponding fabrication process. However, before this, the corresponding fabrication process should be modified to seek for better performance of the prototype device.

To realize our design idea for the prototype design, a new fabrication process that combines silicon-on-insulator (SOI) wafer and prototype design (bi-chevron AlN Actuator) has been developed (as shown from Fig. 82 to Fig. 120). The whole fabrication process of this prototype device is started on a SOI wafer with 10 µm device layer and 0.25 µm isolating oxide layer.

The fabrication process for the prototype devices is started with a SOI wafer that has a 10 µm thick device layer and 0.25 µm thick isolation layer (as shown in Fig. 82). First, an 1.3 µm OCG 825 (G-line) will be deposited (as shown in Fig. 83) and defined (as shown in Fig. 84) to define the microchannel for supercritical carbon-dioxide flow. After hardbake, this wafer will be put into deep reactive-ion etching (DRIE) system, Surface Technology Systems (STS) Advanced Silicon Etch (ASE) system. This system will etch the device silicon layer that is not protected by the PR. Due the excellent selectivity (100:1 between G-line PR and silicon) between silicon and oxide in STS, the DRIE will stop at the interface of device layer and oxide layer and this step will not attack the substrate at all (as shown in Fig. 85). Here, STS is operated under low frequency (LF) mode since it used for the etching of silicon layer to oxide layer. The SOI LF option can reduce the non-uniformity etch of the wafer (bull's-eye effect), the micro loading effect (RIE lag), and the aspect ratio dependent etching effect (ARDE).

After strip the photoresistive (PR) for the etch mask of STS (as shown in Fig. 86), the wafer will be cleaned with piranha. And then the wafer will be deposited with 2 µm tetraethooxysihme (TEOS) oxide as the sacrificial layer (Fig. 87). Here TEOS oxide is chosen as the oxide material for sacrificial layer because TEOS oxide has much better step coverage than thermal oxide and low-temperature oxide (LTO) [109-111]. That is why TEOS oxide can fill the trench with less oxide thickness deposition [112].  However, TEOS oxide doesn't have good insulation quality. Thus after the TEOS oxide deposition, the wafer will be annealed in furnace 1000°C for 1 hour to improve the quality of TEOS oxide [113].

After TEOS oxide annealing, a 2µm PR will be deposited and define (as shown in Fig. 88 and Fig. 89) for the following the sacrificial layer definition step.  And then the PR will be hardbaked to become the etch mask for the following oxide wet etch step. Here wet oxide etch is used instead of dry oxide etch. It is because wet etch can offer a less steep side wall than dry etch and then can avoid the bad bottom electrode coverage over the opening. After using buffer HF (BHF) 5:1 for TEOS oxide wet etch (as shown in Fig. 90), the etch mask PR will be striped (as shown in Fig. 91). Here buffer HF is used instead of HF since HF will peel off the PR and buffer HF will not.

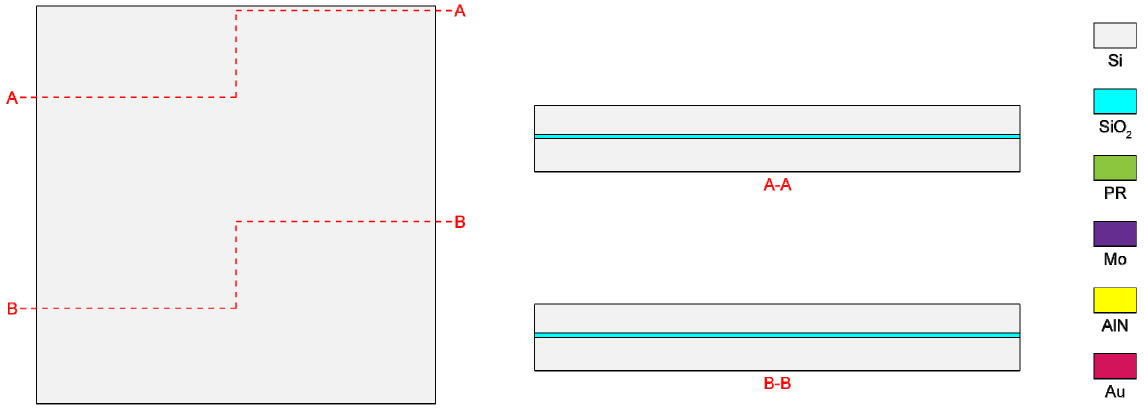

Fig. 82.  SOI wafer for the prototype device for the prototype device.

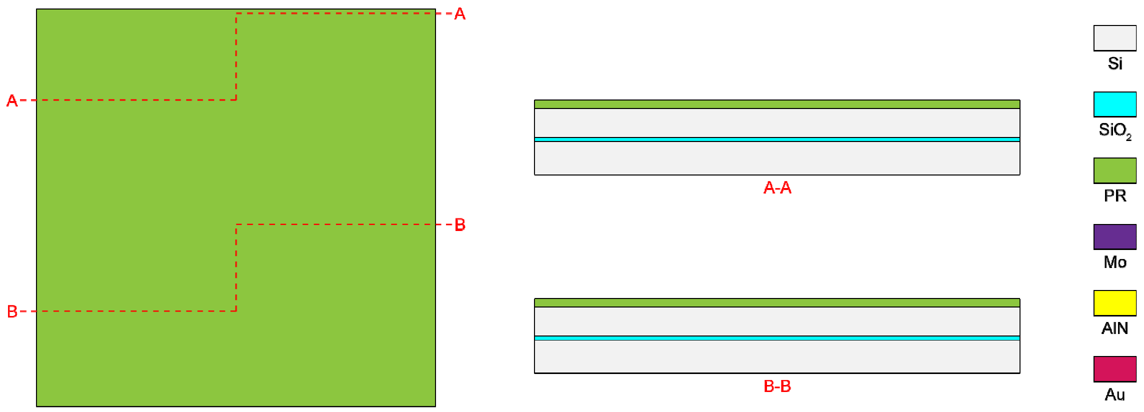

Fig. 83. Deposit photoresist for the prototype device.

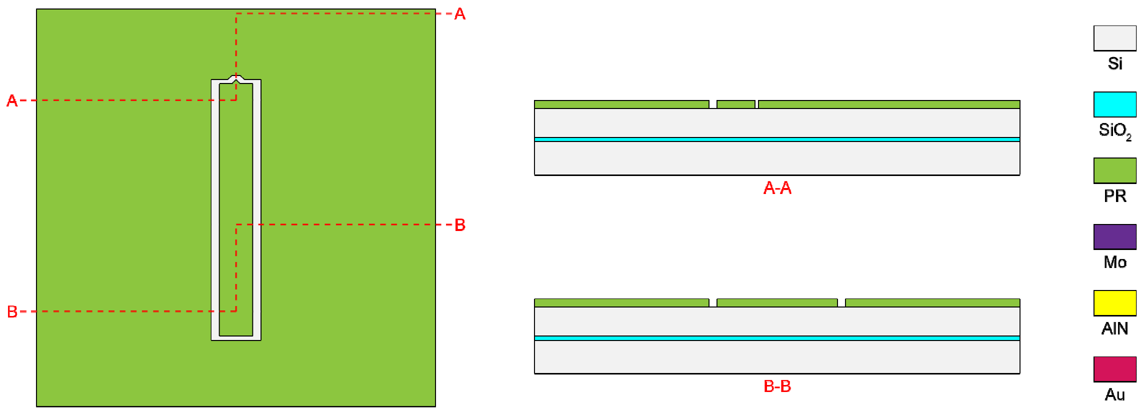

Fig. 84. Deposit photoresist to define microchannel for the prototype device.

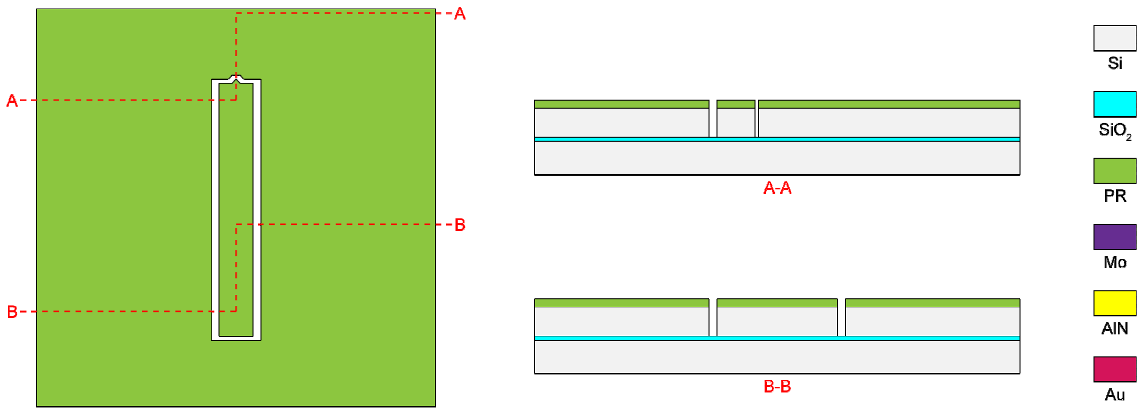

Fig. 85. Etch device layer in STS with photoresist etch mask for the prototype device.

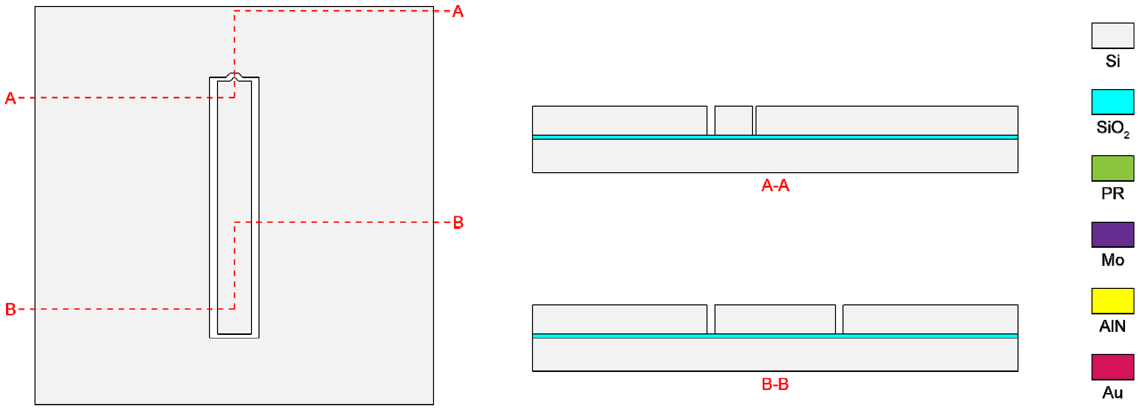

Fig. 86. Strip PR for the prototype device.

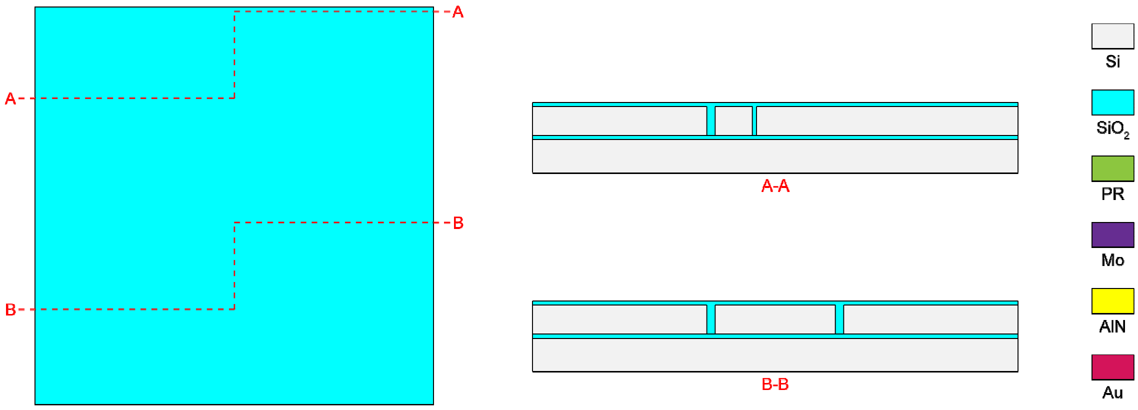

Fig. 87. Deposit sacrificial layer TEOS to fill the microchannel for the prototype device.

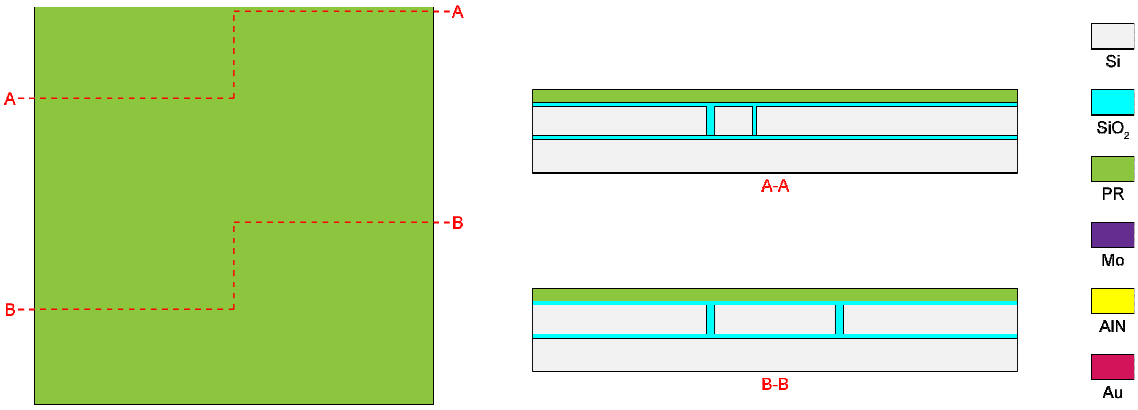

Fig. 88. Deposit photoresist to define TEOS oxide for the prototype device.

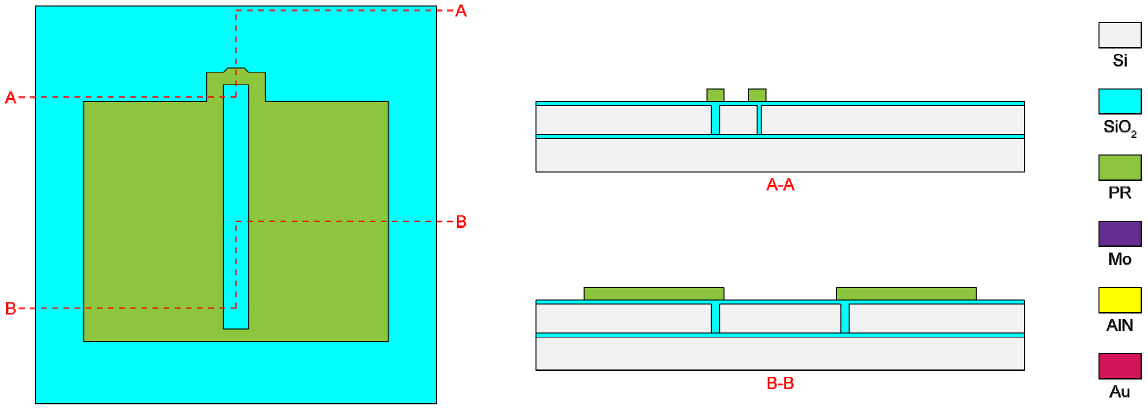

Fig. 89. Define PR for the prototype device.

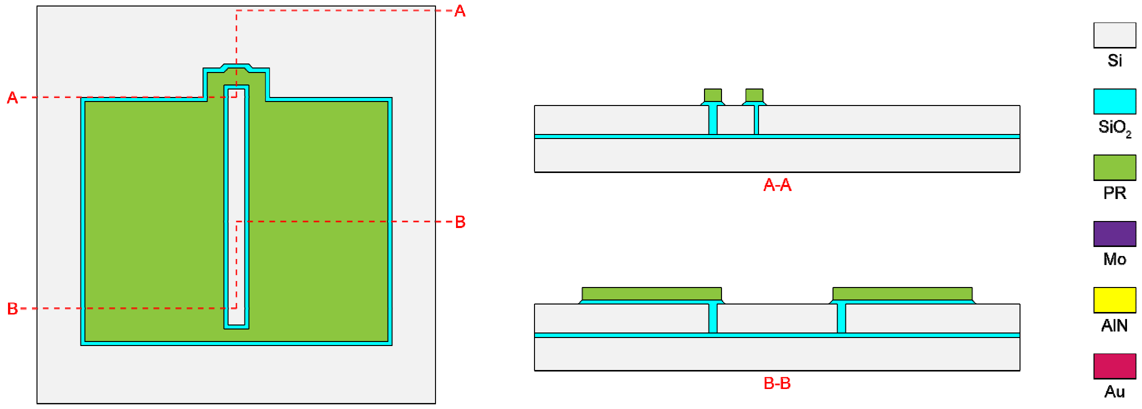

Fig. 90. Wet etch TEOS oxide for the prototype device.

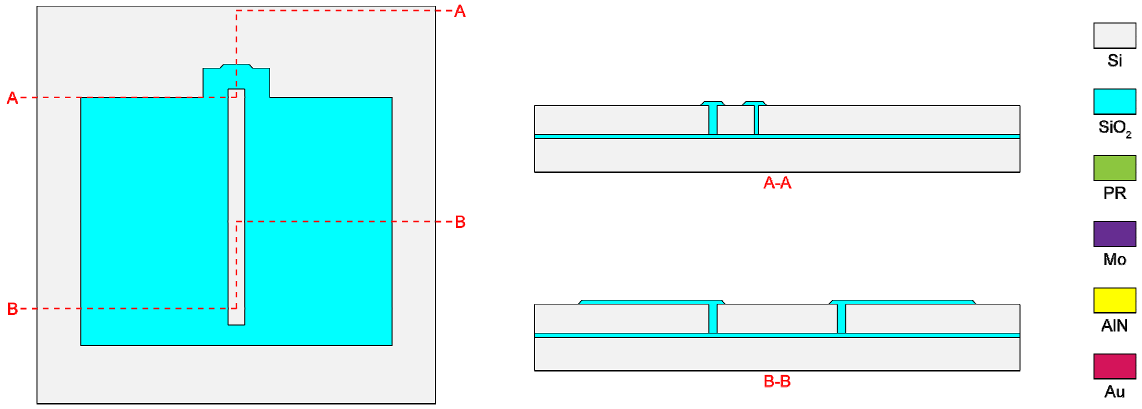

Fig. 91. Strip PR for the prototype device.

Next, the bottom electrode molybdenum (Mo) can be deposited. The quality of the bottom electrode Mo is very important since it will influence the quality (crystal orientation) of the piezoelectric layer (AlN) that is deposited on the bottom electrode Mo. In order to get really high quality of Mo layer, these special steps were performed in the fabrication process:

1. *Piranha clean before the deposition:* The wafer should be cleaned with piranha before the deposition. Piranha can remove any organic and dirty particles on the wafer surface and then offer better surface condition for the bottom electrode material to crystallize. This can result in better crystal orientation of the bottom electrode material.
2. *Seed layer deposition before the deposition*: A Seed layer [114-122] is deposited on the dielectric layer to improve the crystal orientation of the bottom electrode by introducing a lower energy barrier (activation energy/potential barrier) material. The seed layer must be thin, smooth, continuous, and high purity to make sure that there are no cracks or holes. For bottom electrode (Mo), different seed layer materials (AlN seed layer [114-117], Au seed layer [117], or Ti seed layer [118-122]) have been used to improve the quality of bottom electrode Mo and then induce a good crystal orientation of the AlN thin film.

Due to these reasons, a 30 nm thick AlN seed layer is deposited before the deposition of bottom electrode Mo since this AlN seed layer can improve the crystal orientation of Mo. The stress of the bottom electrode Mo layer is controlled to between 0 MPa to 100 MPa tensile to avoid the broken of the AlN bema due to the high tensile stress. The stress and crystal orientation of Mo can be optimized by altering the process parameters [123]. Next a well crystal-oriented and low stress 250 nm Mo thin film is deposited (as shown in Fig. 92and then follows by the 2µm AlN thin film deposition (as shown in Fig. 93). Here the stress of the AlN thin film is controlled between 0 MPa tensile to 100 MPa tensile to avoid any fracture of the AlN beams. And in order to obtain excellent crystal orientation of the AlN film, all the AlN seed layer, Mo bottom electrode, and AlN piezoelectric layer are all deposited in the machine without breaking the vacuum. This will reduce the opportunity for any contamination when the wafer is exposed to the air and then keep the best surface condition for the following deposition.

Once the active AlN layer deposition is done, the plasma-enhanced chemical vapor deposition (PECVD) oxide is deposited to become the etch mask for AlN via etch (as shown in Fig. 94). This PECVD oxide is deposited at a temperature around 200°C. After this low-temperature PECVD oxide deposition, a PR layer will be deposited (as shown in Fig. 95), defined (as shown in Fig. 96), and then hardbaked to define AlN via wet etch area. With this PR layer as the etch mask, the PECVD oxide will be wet etched (as shown in Fig. 97with 5:1 BHF and then the PR can be striped (as shown in Fig. 98).

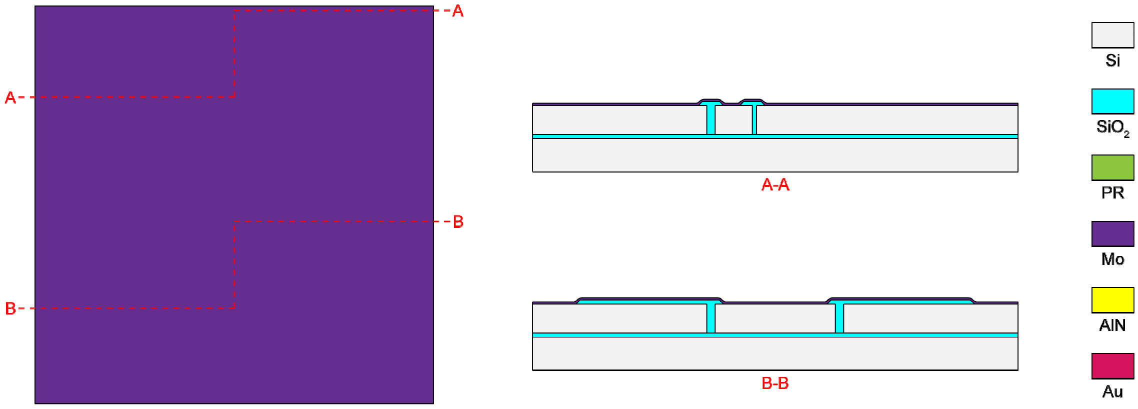

Fig. 92. Deposit bottom electrode Mo for the prototype device.

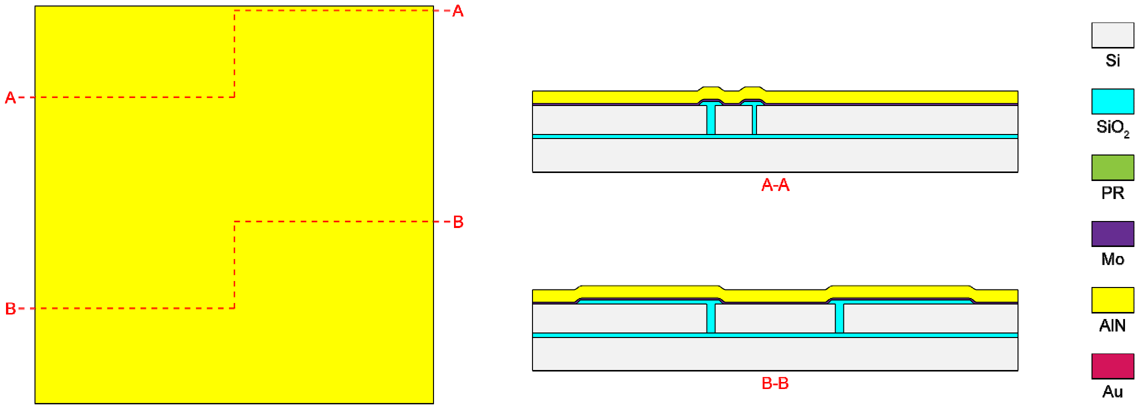

Fig. 93. Deposit piezoelectric layer AlN for the prototype device.

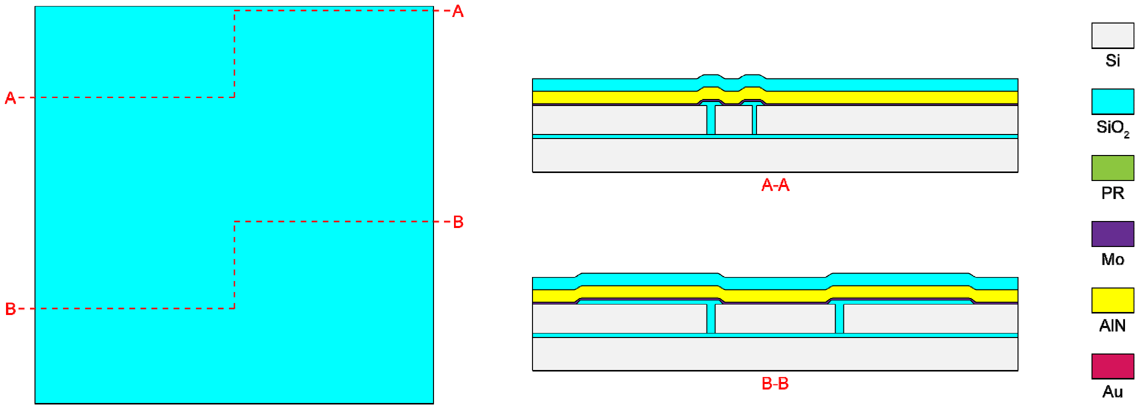

Fig. 94. Deposit AlN via etch mask for the prototype device.

After strip the PR, hot phosphoric (160 °C) will be use to etch AlN via (as shown in Fig. 99) with the low-temperature PECVD oxide as the etch mask. Here, hot phosphoric is selected for the AlN via wet etch because its good selectivity between AlN and Mo. And then the whole wafer will be put in the BHF 5:1 again to etch away the oxide etch mask used for AlN via etch (as shown in Fig. 100). Next, the top electrode Mo will be deposited on the active AlN layer by RF sputtering (Fig. 101). The stress of the top electrode Mo is controlled within 0 MPa tensile to 100 MPa tensile to avoid the bending or buckling of AlN after vapor HF releasing step.

Next, G-line PR will be deposited (as shown in Fig. 102) and defined (as shown in Fig. 103) to be used for the etch mask of the top electrode Mo etch. After all, the top electrode Mo will be etched with the plasma etch tool (as shown in Fig. 104) and then the etch mask, PR, will be striped (as shown in Fig. 105).

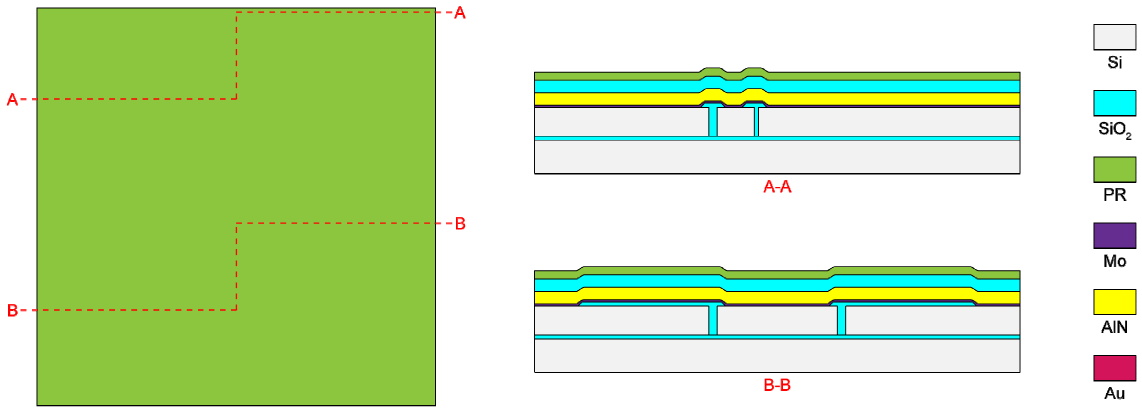

Fig. 95. Deposit PR to define the AlN via for the prototype device.

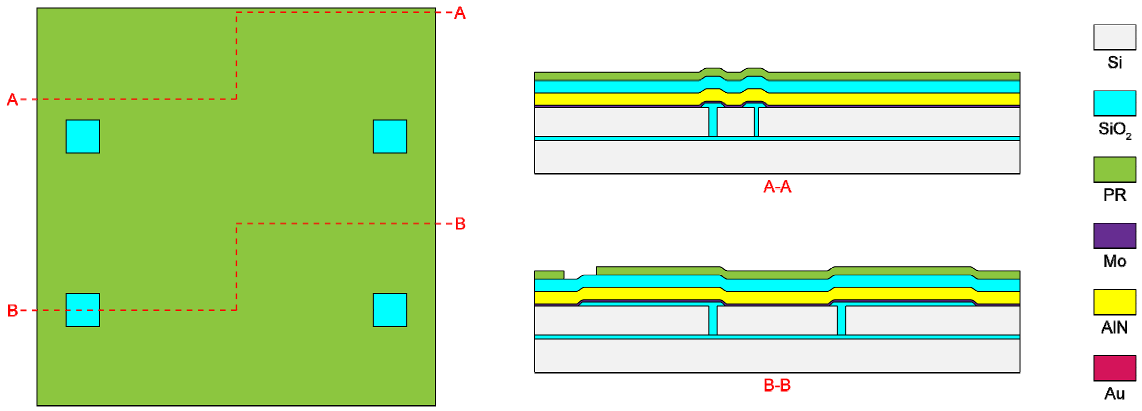

Fig. 96. Define PR for the prototype device.

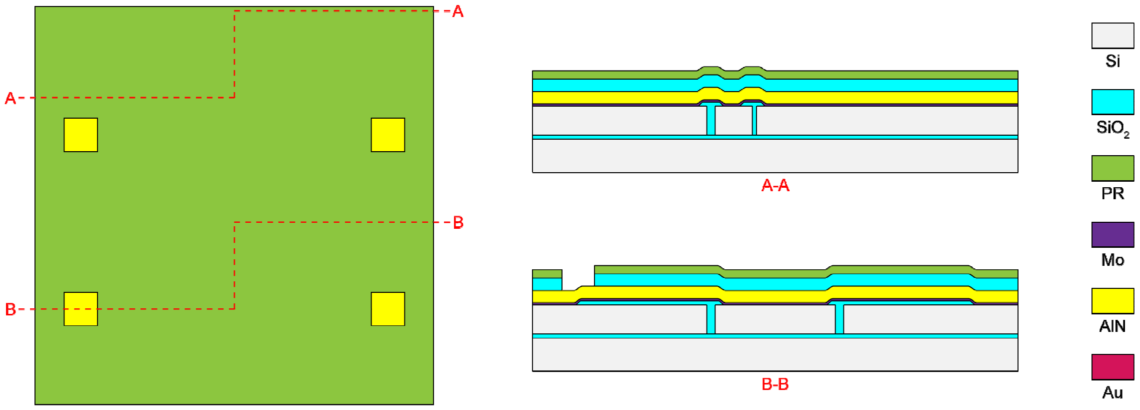

Fig. 97. Wet etch the oxide to define the etch mask for AlN via for the prototype device.

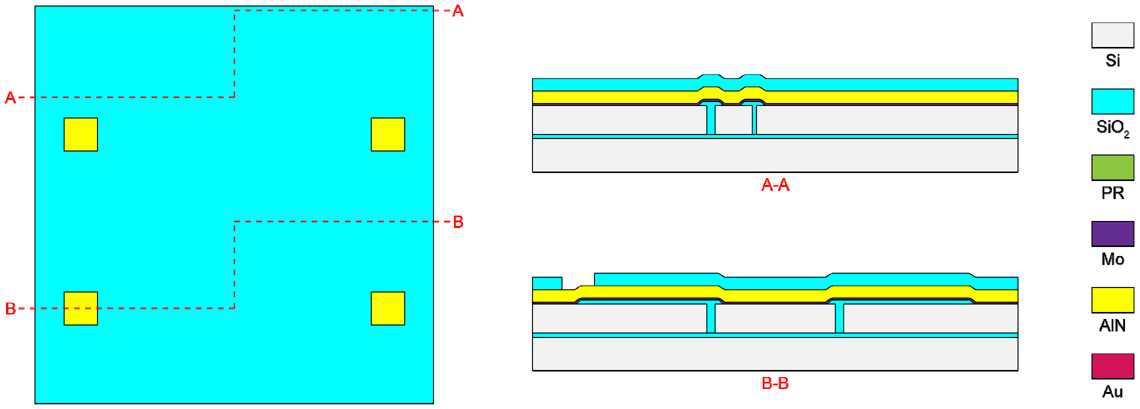

Fig. 98. Strip PR for the prototype device.

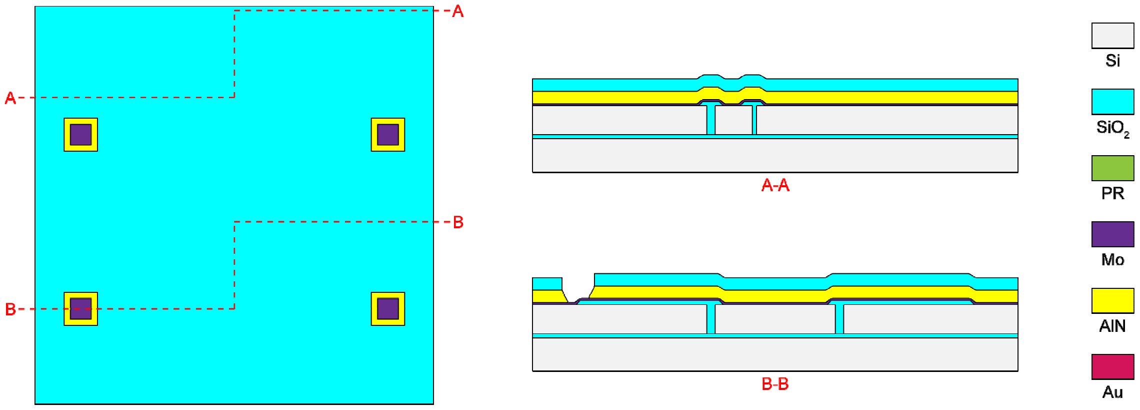

Fig. 99. Hot phosphoric etch AlN via for the prototype device.

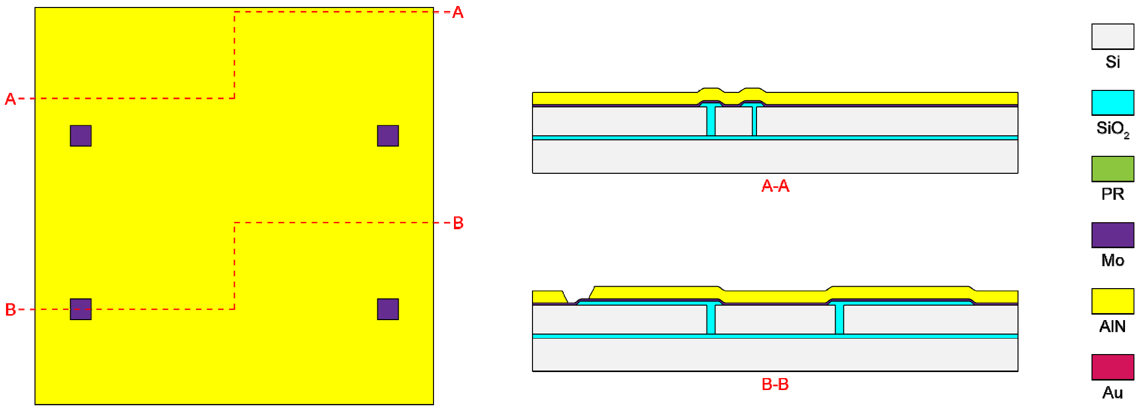

Fig. 100.  Wet etch away the etch mask of AlN via for the prototype device.

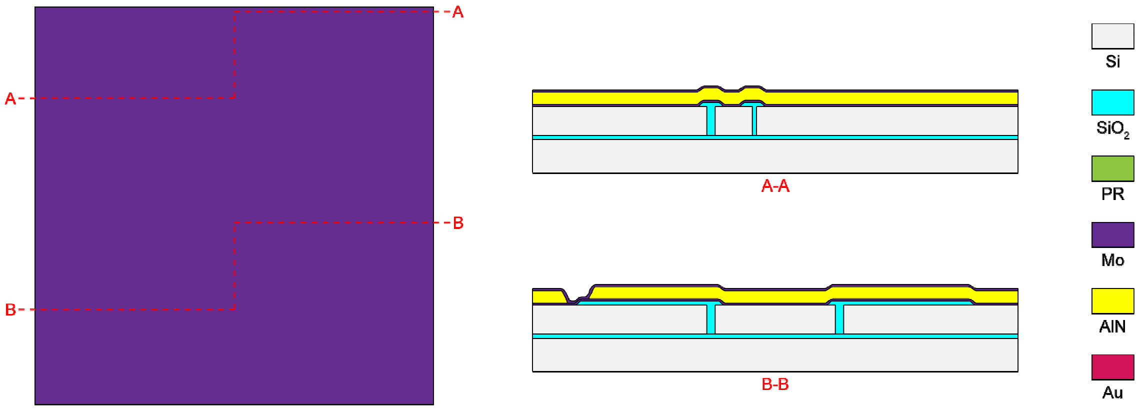

Fig. 101.  Deposit top electrode Mo for the prototype device.

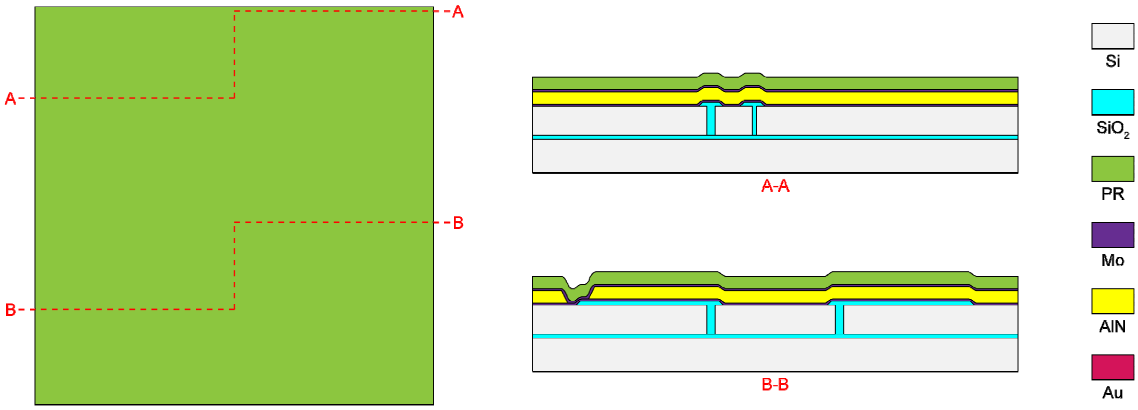

Fig. 102.  Deposit PR to define top electrode for the prototype device.

The next step will be the AlN etch with oxide etch mask. The oxide etch mask is deposited by 200°C PECVD (as shown in Fig. 106tool. And then, the PR will be deposited (as shown in Fig. 107), defined (as shown in Fig. 108), and hardbaked. With this PR etch mask, we will do oxide dry etch to define the oxide etch mask for AlN (as shown in Fig. 109) and then the PR etch mask for oxide etch (Fig. 110) will be stripped.  Since the oxide etch mask is defined, we can start the AlN etch (as shown in Fig. 111) to define the outline of the bi-chevron AlN actuator.

In order to reduce the resistivity near AlN via and get better electrical connection between top electrode and bottom electrode near AlN via, a 200 nm Au is deposited to cover the AlN via area. For the 200 nm Au deposition, an opening of the PECVD oxide etch mask for the AlN etch is needed. To do this, we will deposit (as shown in Fig. 112), defined with photolithography (as shown in Fig. 113), and hardbake PR to make an opening on wet oxide etch of the AlN etch mask. Next we wet etch the AlN oxide etch mask with BHF 5:1 (as shown in Fig. 114) and after this step the PR is stripped (as shown in Fig. 115). Since the opening for Au deposition is generated, we can start the lift-off process for the Au deposition.

For the lift-off process, we will deposit PR (as shown in Fig. 116) and then define this PR (as shown in Fig. 117). And then, we can deposit the Au layer (as shown Fig. 118) and perform the lift-off process to define the Au (as shown in Fig. 119). After dicing the wafer for singulation, we can release the device with HF to avoid the broken of the beam due to stiction (as shown in Fig. 120). The pictures of prototype device from this fabrication process are as shown in Fig. 121 and its Vernier scale for the generated stroke measurement is as shown in Fig. 122.

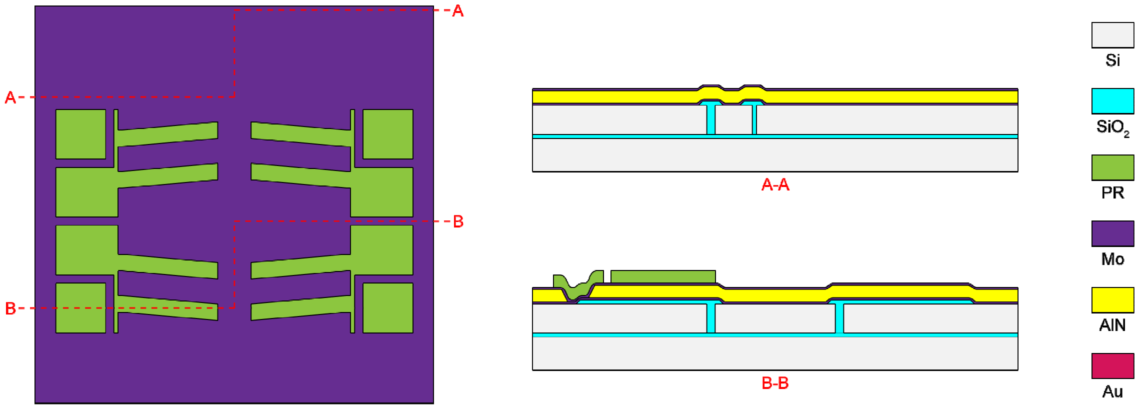

Fig. 103.  Define PR for top electrode etch for the prototype device.

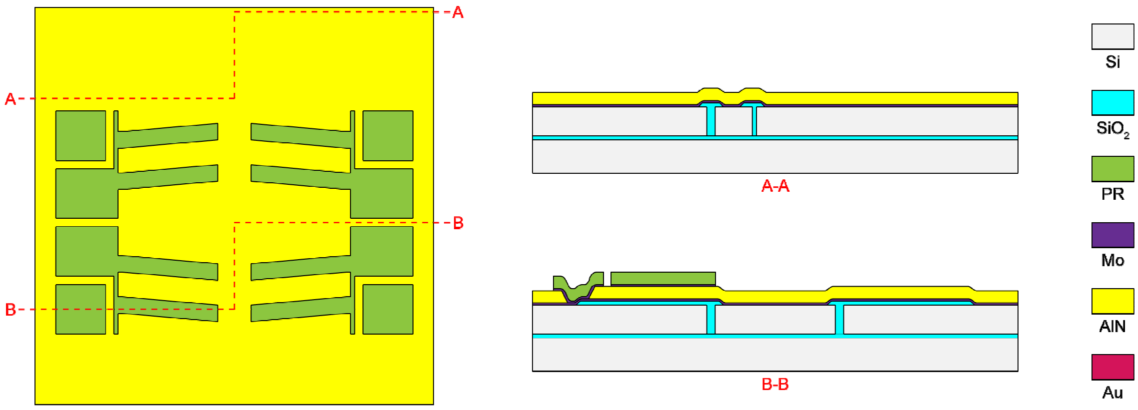

Fig. 104.  Top electrode Mo etch for the prototype device.

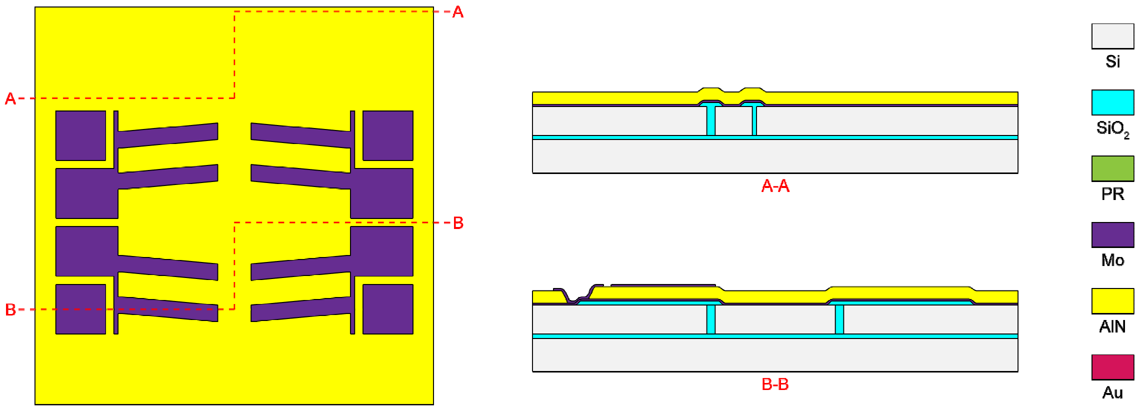

Fig. 105.  Strip PR for the prototype device.

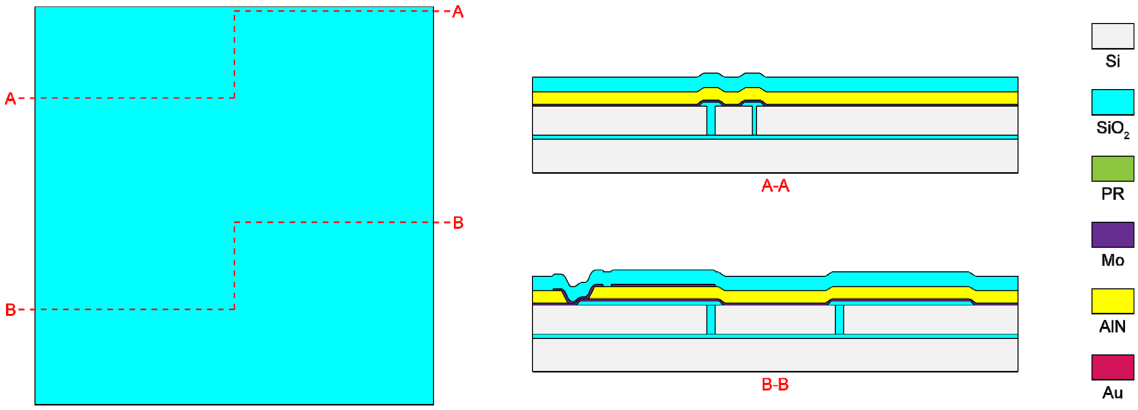

Fig. 106.  Deposit PECVD oxide as the etch mask for AlN etch for the prototype device.

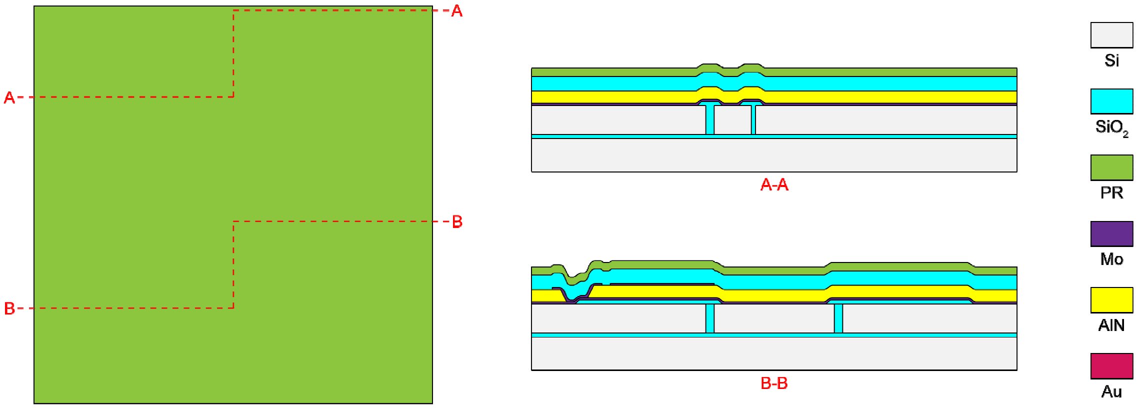

Fig. 107.  Deposit PR to define the etch mask for AlN etch for the prototype device.

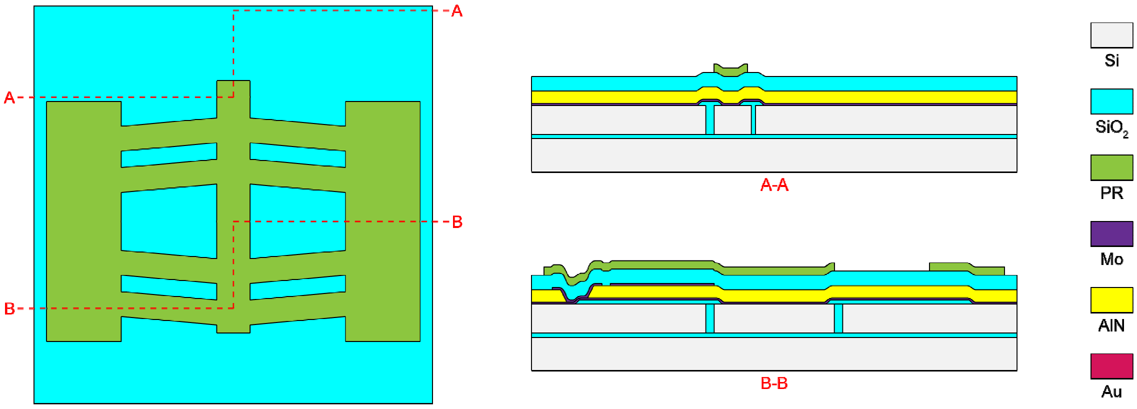

Fig. 108.  Define PR to define the etch mask for AlN etch for the prototype device.

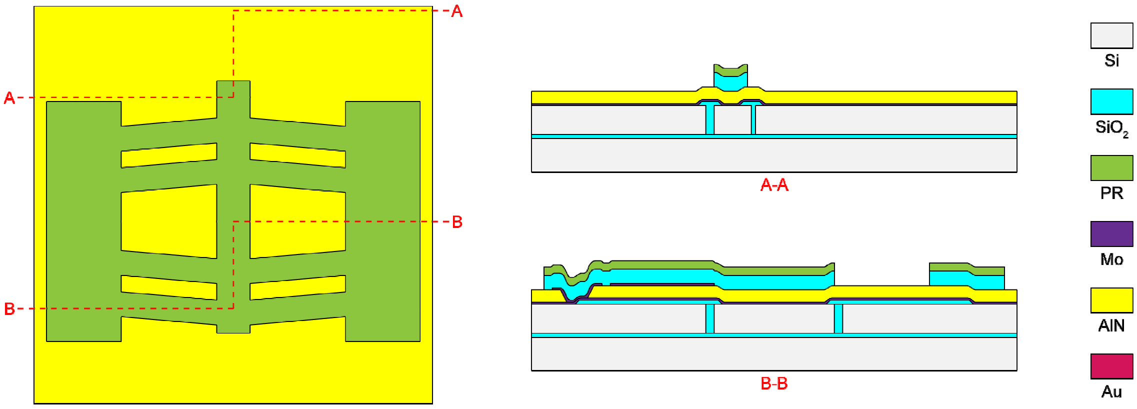

Fig. 109.  Dry etch oxide to define the etch mask for AlN etch for the prototype device.

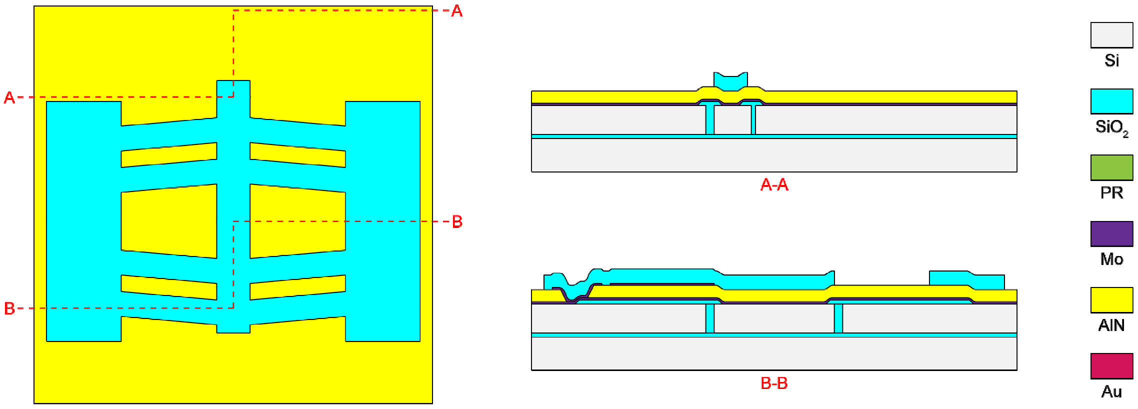

Fig. 110. Strip PR for the prototype device.

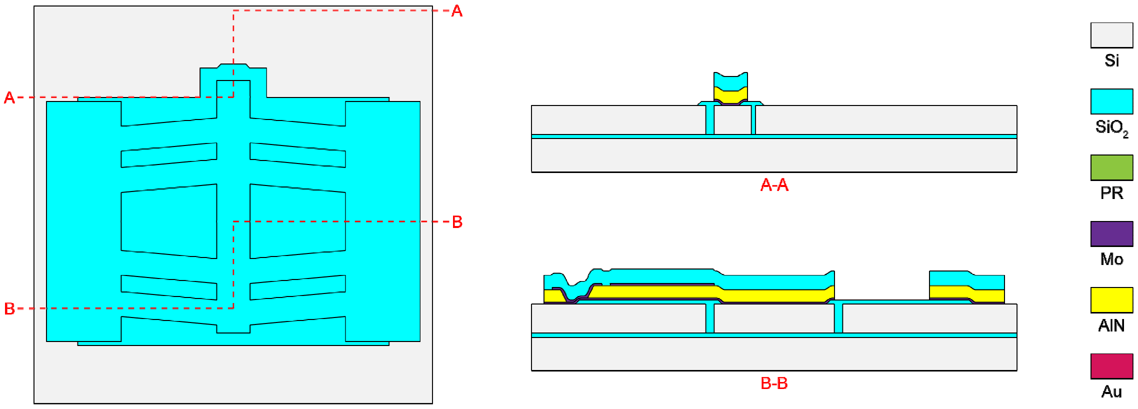

Fig. 111. Dry etch AlN to define AlN with the oxide etch mask for the prototype device.

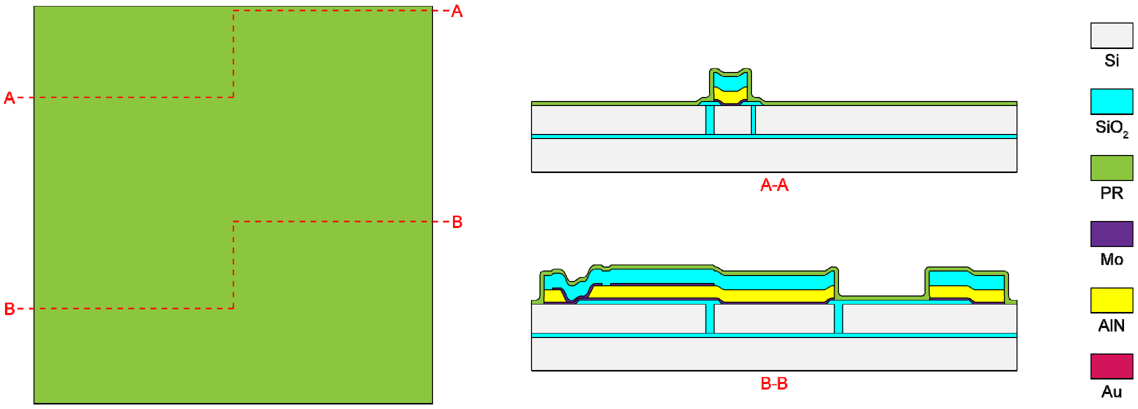

Fig. 112. Deposit PR for Au lift-off for the prototype device.

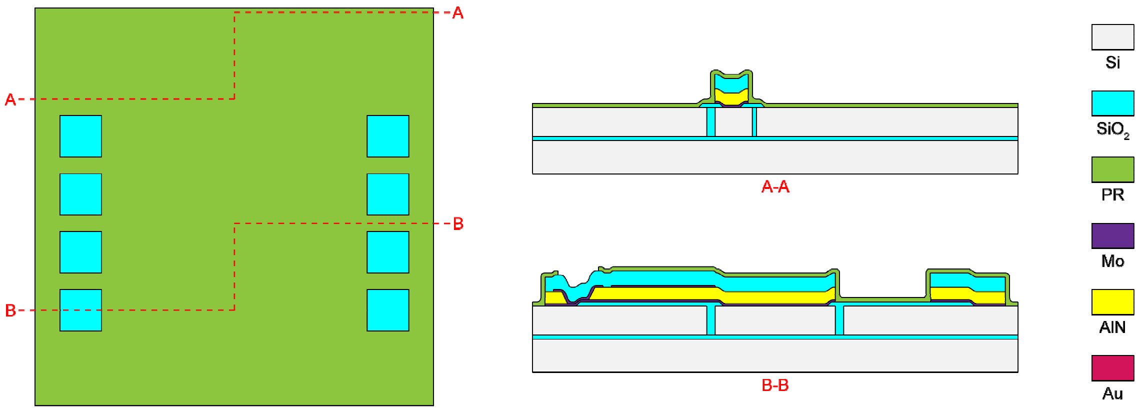

Fig. 113. Define PR for Au lift-off for the prototype device.

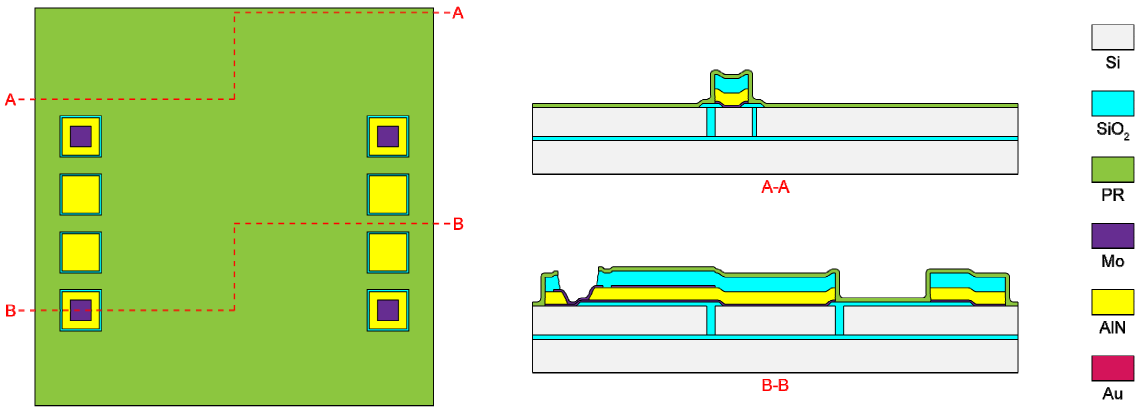

Fig. 114. Wet etch PECVD oxide for Au lift-off for the prototype device.

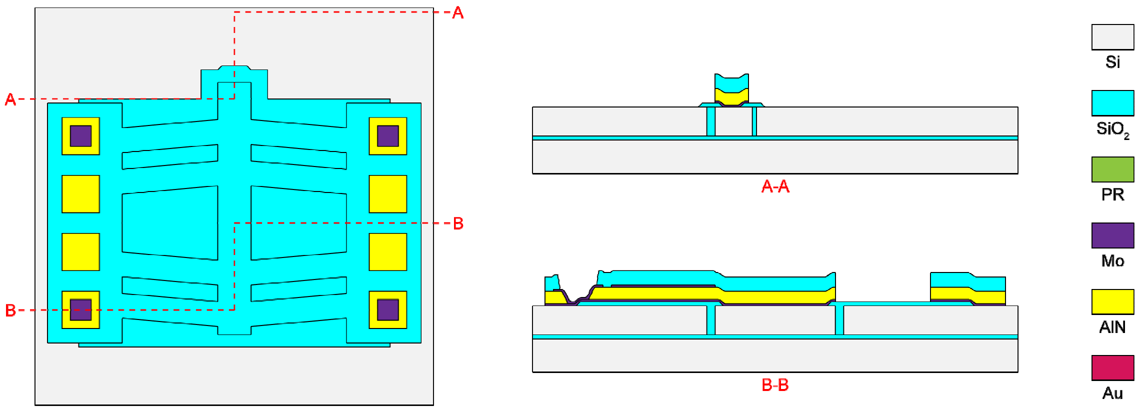

Fig. 115. Strip PR for the prototype device.

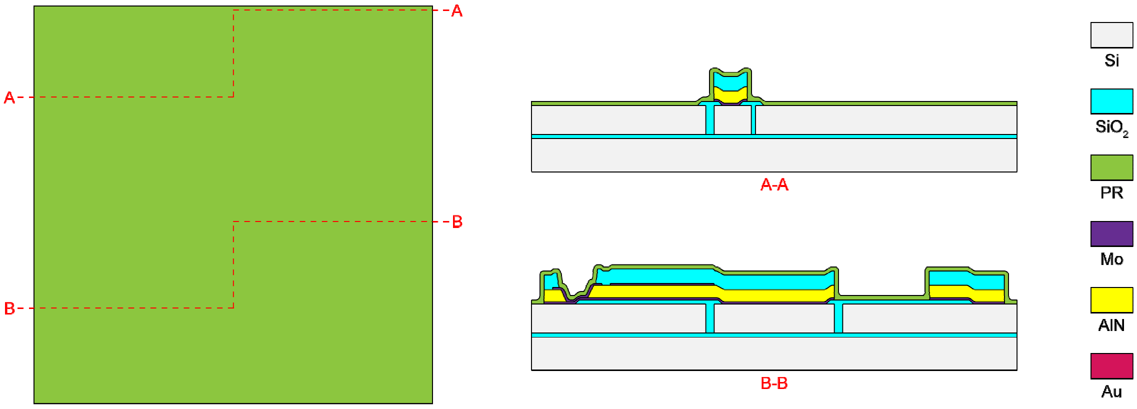

Fig. 116. Deposit PR for Au lift-off for the prototype device.

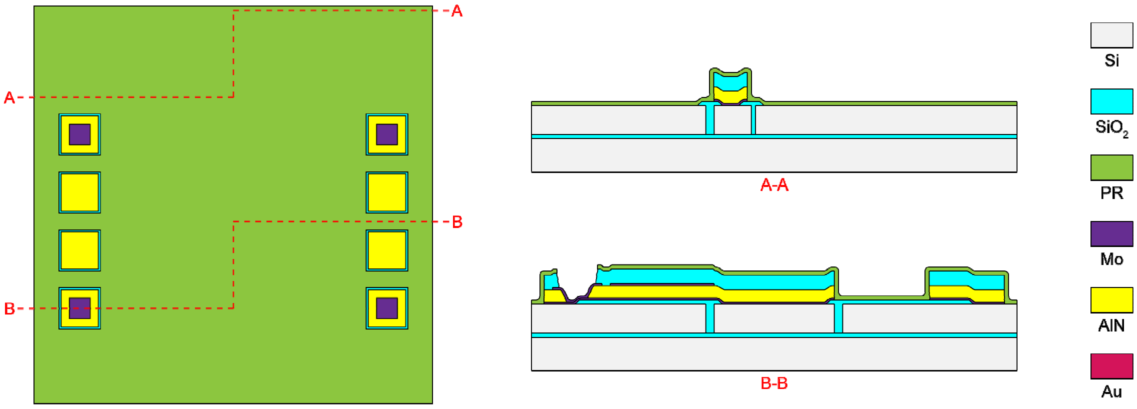

Fig. 117. Define PR for Au lift-off for the prototype device.

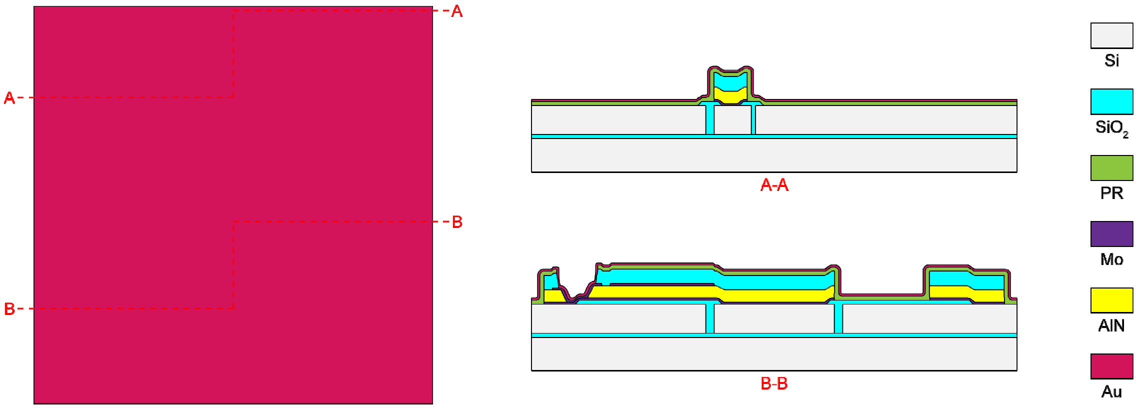

Fig. 118. Deposit Au for lift-off for the prototype device.

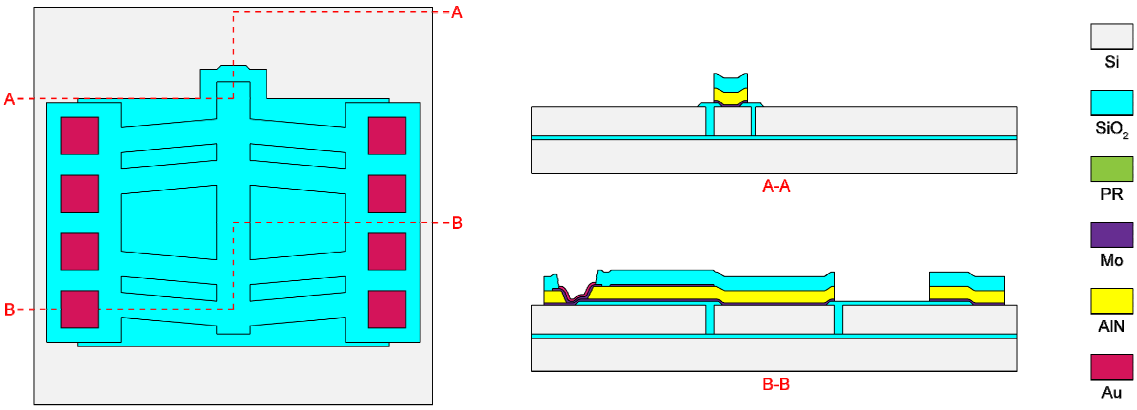

Fig. 119. Lift-off Au for the prototype device.

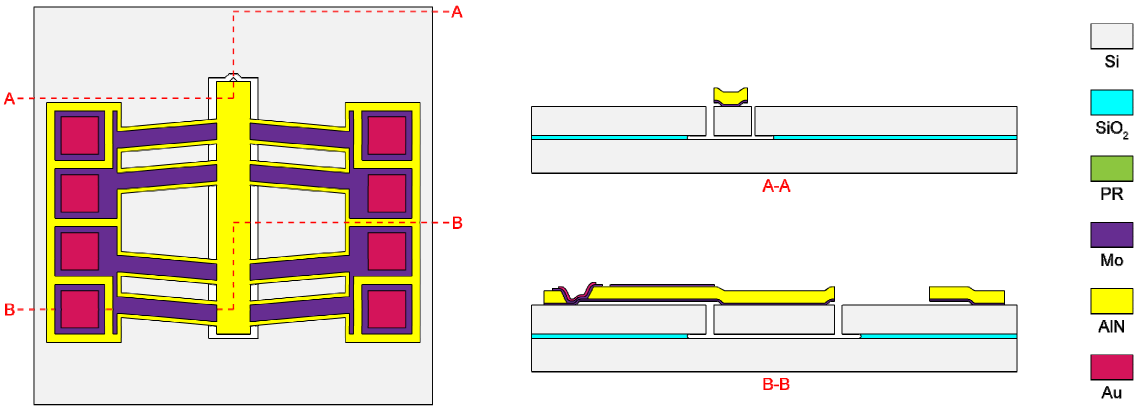

Fig. 120. Vapor HF releasing for the prototype device.

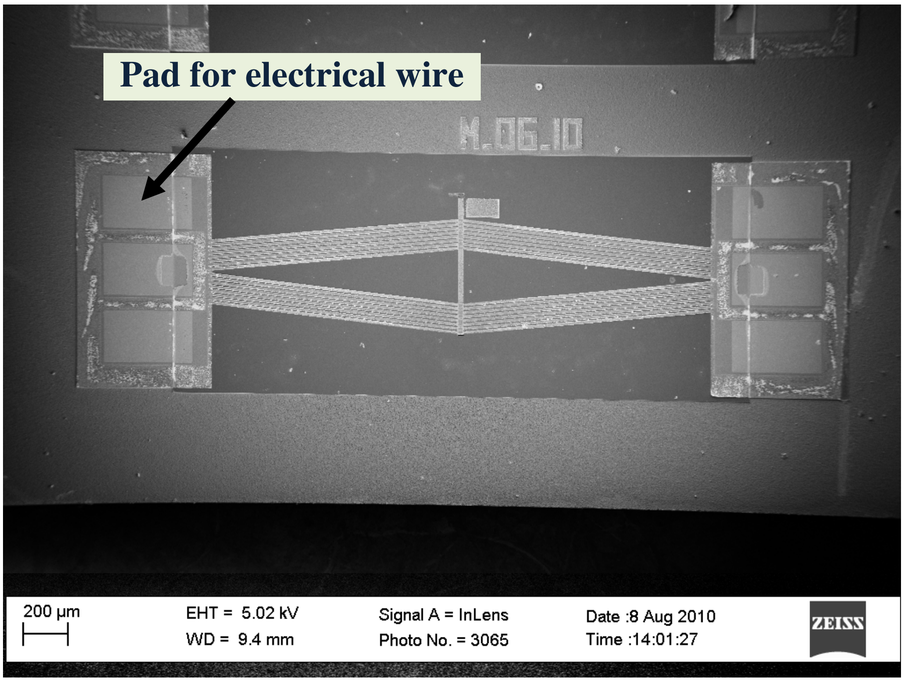

Fig. 121. SEM pictures of the prototype device.

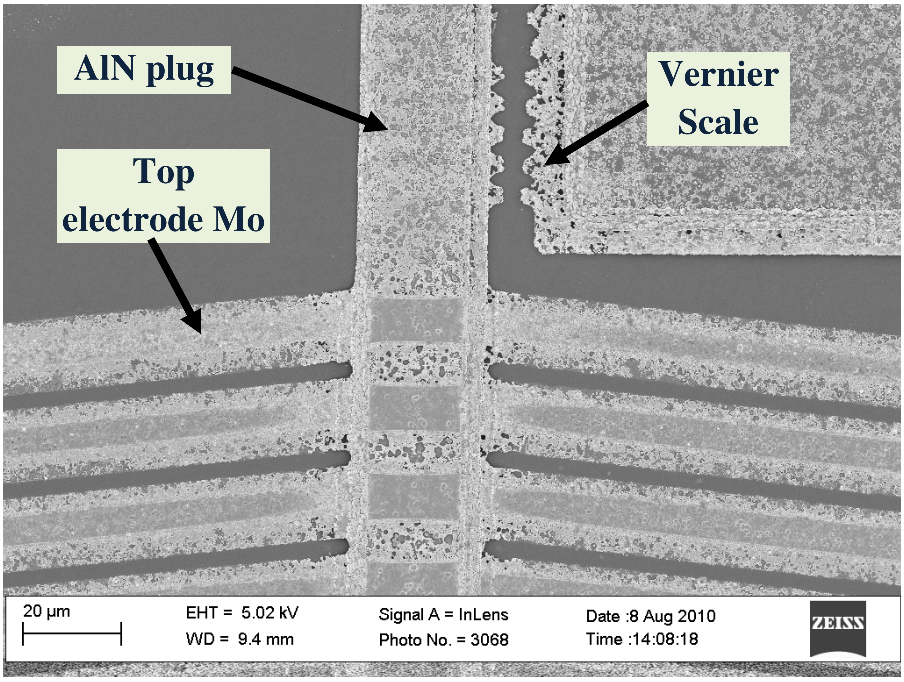

Fig. 122. SEM pictures of the Vernier scale on the prototype device.

# Chapter 5 Experiment Testing of Pre-Prototype Device and Prototype Device for Supercritical Carbon Dioxide Valve

## 5.1 Static Characteristic of Pre-Prototype Device

The fabricated pre-prototype device will be mounted on the package chip and then be wire-bonded for the electrical connecting (as shown in Fig. 123). Once this step is finished, the pre-prototype device with its package chip will be applied with the corresponding electrical field to make the movement (as show in Fig. 124). In the setup, two DC power supplies (Hewlett Packard E3612A) are used to apply different electrical field on the upper pair and lower pair AlN beams to actuate the pre-prototype devices (as shown in Fig. 124). In Fig. 124, there are two 10KΩ resistors connecting to the positive and negative input voltage. These two resistors are used to over-current causing the device to burn and fail. In this setup, a microscope is focused on tip of the pre-prototype device to observe the change Veriner scale part (as shown in Fig. 125 (A)) and this change of Vernier scale can be record by a computer for the calculation of the generated stroke (as shown in Fig. 125 (B)).

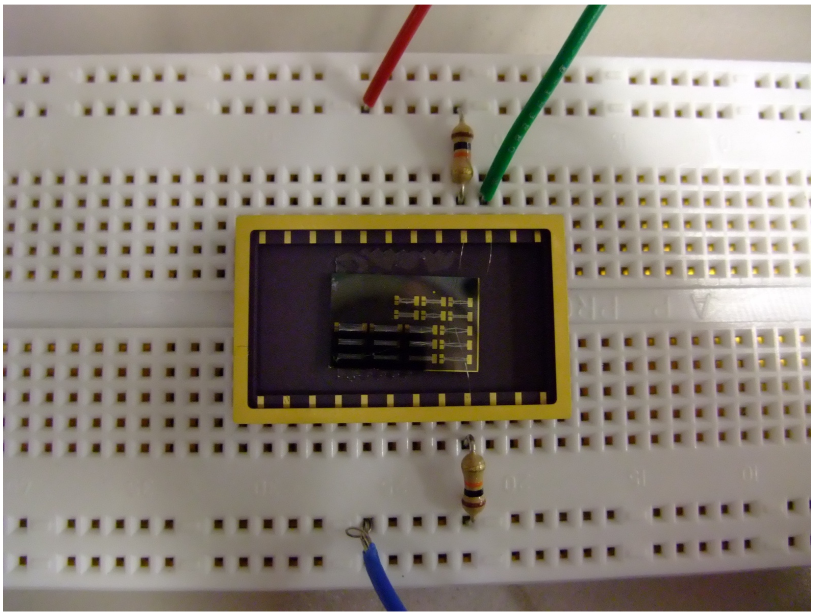

Fig. 123. Fabricated pre-prototype on the package chip.

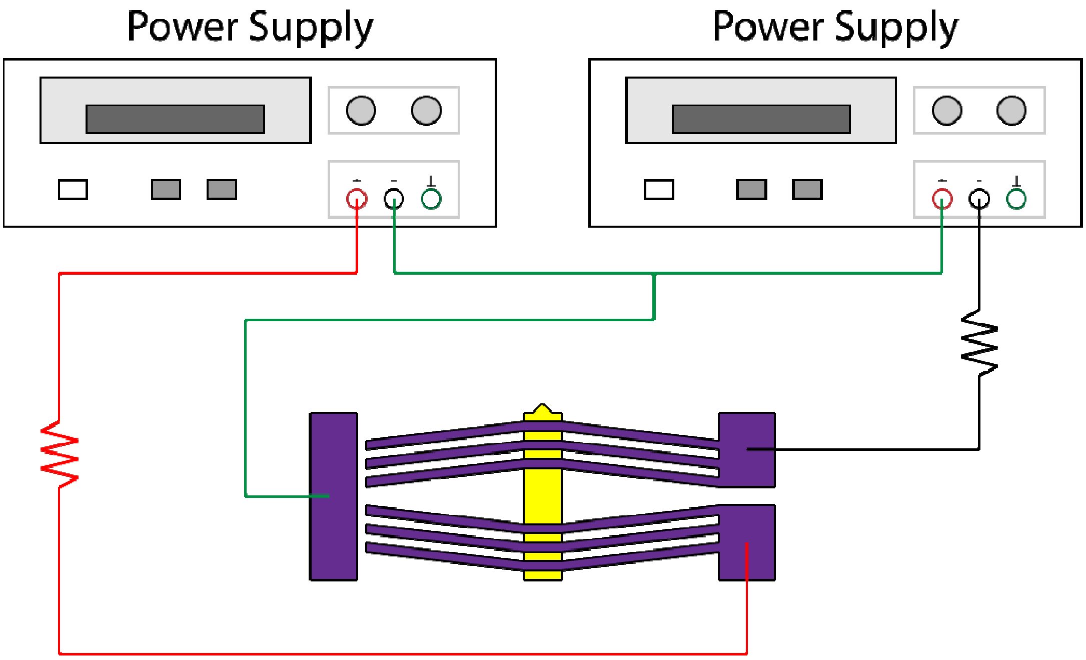

Fig. 124. Sketch of electrical connecting for the DC power supplies and the devices for in-plane generated stroke measurement.

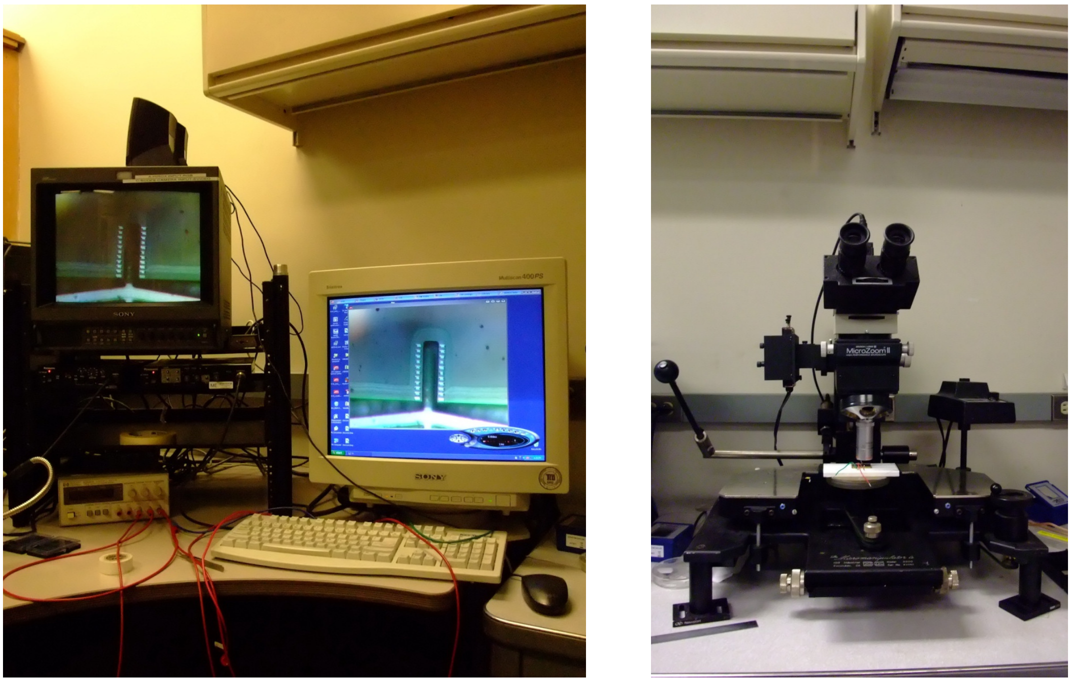
(A) Computer setup to record the image of the movement of pre-prototype devices

(B) Microscope used observe image of the movement

Fig. 125. Setup for in-plane generated stroke measurement during DC actuating voltage.

To verify the bi-direction movement, the pre-prototype device will be actuated to move both forward and backward with corresponding electrical field. Before applying any electrical field, the pre-prototype device is at equilibrium position (as shown in Fig. 126 (A)). First, a positive electrical field will be applied on the upper pair AlN beams and a negative electrical field will be applied on the lower pair AlN beams. This will actuate the pre-prototype device to move forward (as shown in Fig. 126 (B)). And then, next, a negative electrical field will be applied on the upper pair AlN beams and a positive electrical field will be applied on the lower pair AlN beams. This will actuate the pre-prototype device to move backward (as shown in Fig. 126 (C)). And the movement of the pre-prototype can be calculated from the Vernier Scale (as shown in Fig. 127) with the following equation:

$$\Delta G = (\Delta d_1 - \Delta d_2) \times (N - M) \tag{5.1}$$

where $\Delta G$ is the movement of the pre-prototype device, $\Delta d_1$ is the gap between the electrodes for the fixed end, $\Delta d_2$ is the gap between the electrodes for the free end, N is the number of the aligned electrode after movement, and M is the number of the aligned electrode before movement. From the above equation, we know the resolution of the Vernier scale is determined by the difference between $\Delta d_1$ and $\Delta d_2$.

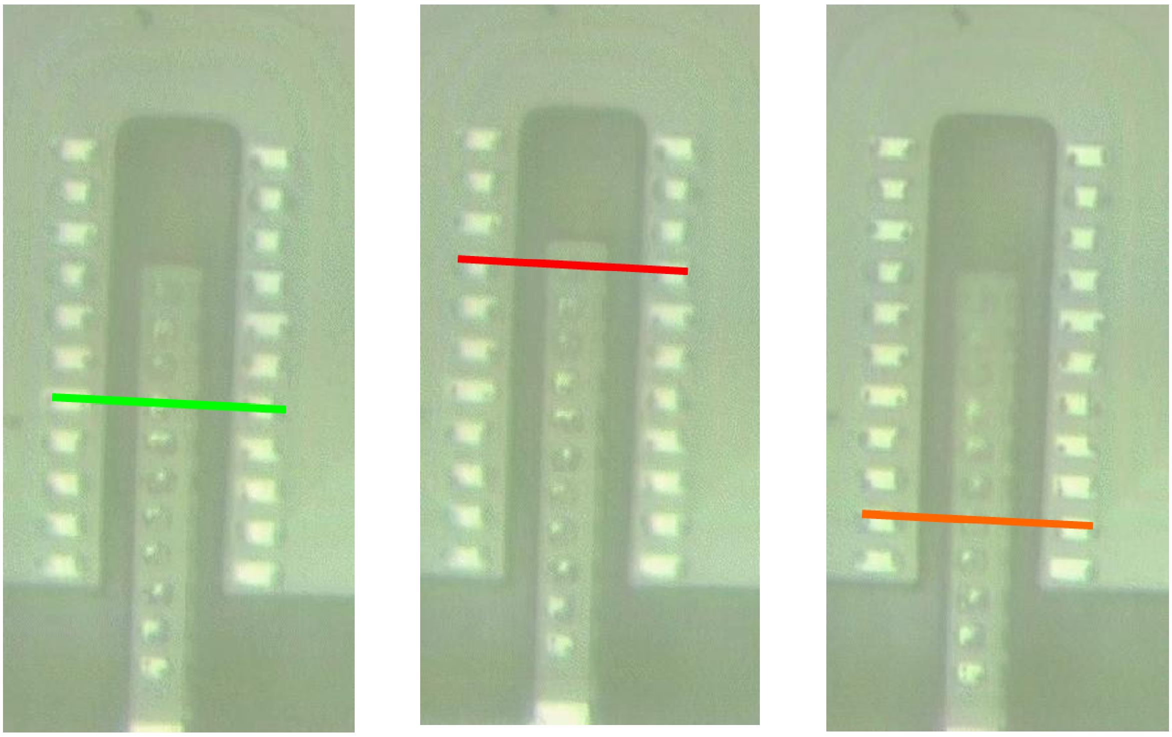
(A) Equilibrium Position (B) Forward Movement (C) Backward Movement

**Fig. 126. Images of Vernier scale when the pre-prototype device is at equilibrium position, actuated to move forward, and move backward.**

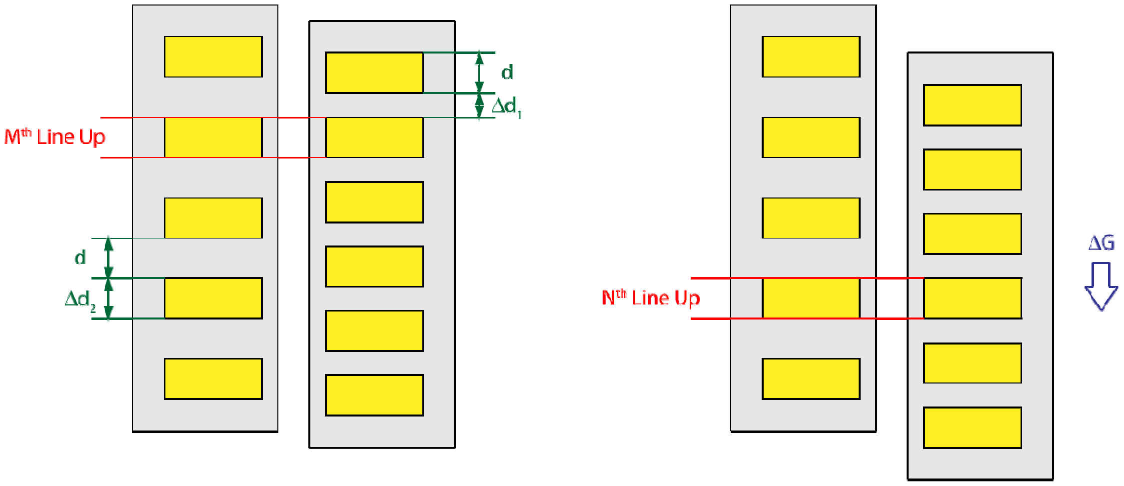

(A) Vernier scale before the movement (B) Vernier scale after the movement

**Fig. 127. Sketch of Vernier scale for movement calculation.**

The comparison of generated stroke between theory, finite-element simulation, and measurement for pre-prototype devices with 1100 µm long, 5 µm wide, and 1 µm thick AlN beams is as shown in Fig. 128and **Error! Reference source not found.**. The generated stroke of the pre-prototype devices agrees well with finite-element-method (FEM) simulation values from ANSYS (maximum error is about 17 %). This difference is suspected to come from the 0.6 µm resolution of the Vernier scale for the pre-prototype devices. The discrepancy between theory and ANSYS is due to the partial-coverage of the top electrode; this has been confirmed by simulation (as shown in Fig. 129). From Fig. 129, it is evident that as the width of the actual top electrode (W') approaches the width (W) of the idea device, the generated force (F') and generated stroke (ΔL') of actual device approaches the generated force (F) and generated stroke (ΔL) of ideal device. This is because partial-coverage results in a nonuniform electrical field along the width of the AlN beam and simultaneously reduces the generated stroke and the generated force. FEM simulation results show the actuation force of the fabricated devices can overcome 10 MPa pressure for a 10 µm by 10 µm plug area for 1 µm AlN thin film.

**Table. 1. Comparison of generated stroke from theoretical calculation, FEM simulation (ANSYS), and measurement data from device. The maximum 17 % error between ANSYS and device is suspect to be from the limitation of the resolution of the Vernier scale (0.6 µm).**

| **Beam Angle (°)** | **Theoretical (µm)** | **FEM (µm)** | **Measurement (µm)** | **Error** |
|---|---|---|---|---|
| **2** | 4.554 | 2.158 | 1.8 | 17 % |
| **4** | 2.442 | 1.144 | 1.2 | 5 % |
| **8** | 1.248 | 0.588 | 0.6 | 2 % |

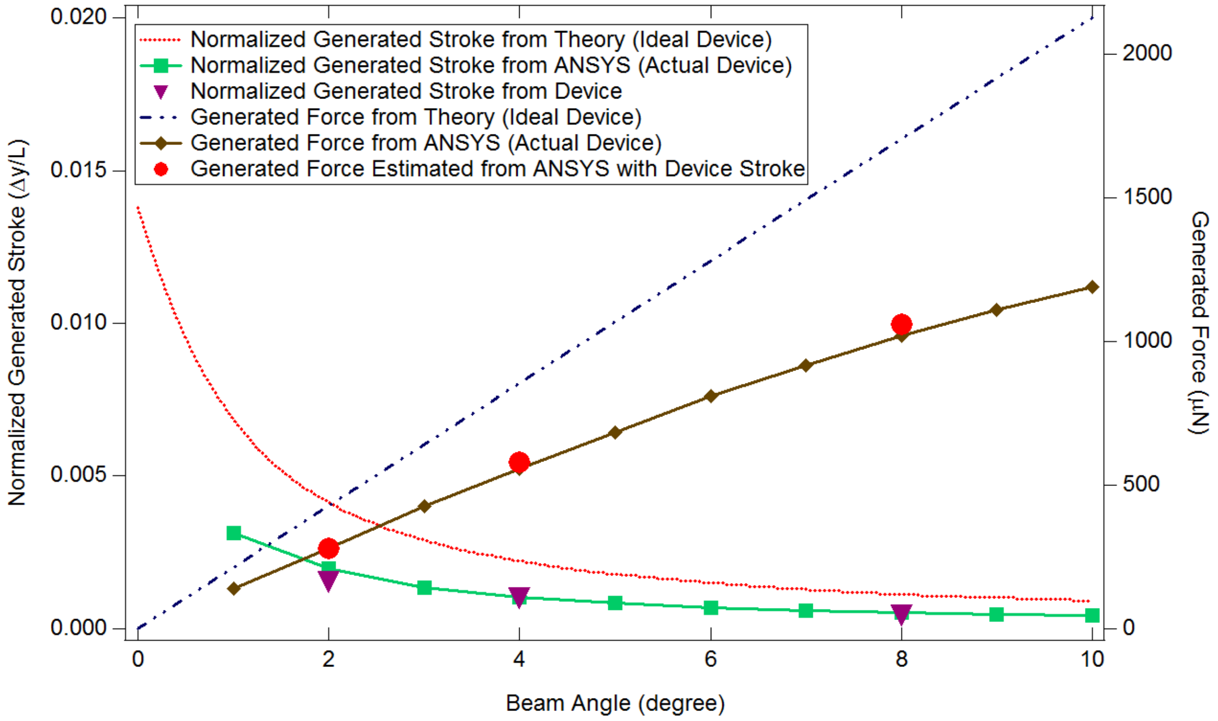

Fig. 128. Theoretical design relationship of normalized generated stroke and normalized generated force for the bi-chevron actuator compared to FEM (ANSYS) and device measurement during DC power actuation.

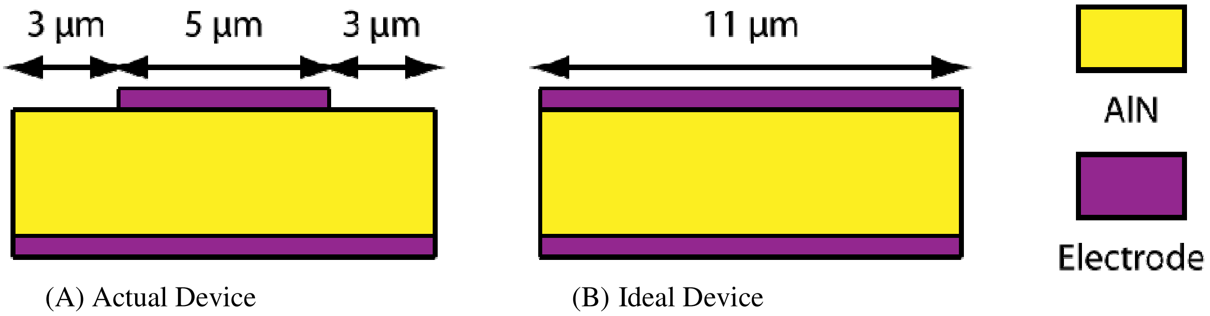

(A) Actual Device (B) Ideal Device

Fig. 129. Top electrode coverage of pre-prototype devices.

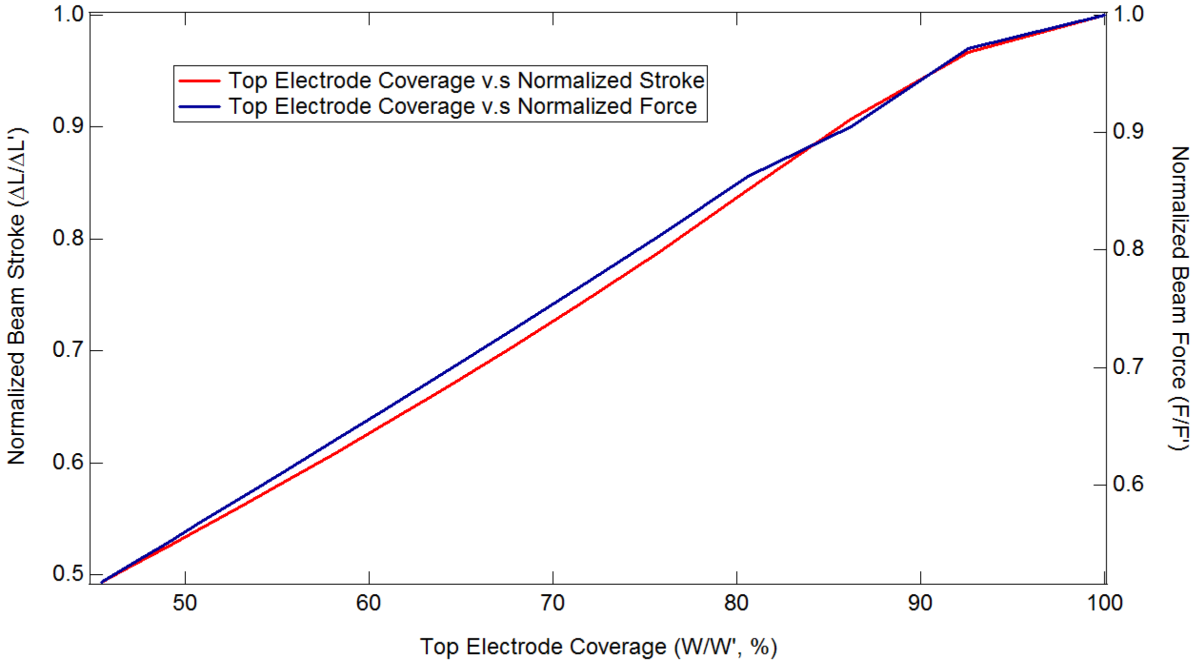

**Fig. 130. Simulation of top electrode coverage for actual device and ideal device and its influence on normalized beam stroke and normalized beam force.**

## 5.2 In-Plane Dynamic Characteristic of Pre-Prototype Device

In order to evaluate the dynamics performance of the pre-prototype (bi-chevron actuator) design for in-plane generated stroke, we use the planar motion analyzer (PMA) setup made by Polytec. This setup uses a high-speed camera with stroboscopic technique and a digital image processing for dynamic measurement. Te high-speed camera can capture image of the movement of the device due the input voltage for different frequency [124]. Digital processing software is used to calculate the motion of the device from the image data collected.

The setup of the MPA is as shown in the Fig. 131. In the setup, we can use the Polytec MMA-400 junction box to apply different voltages with varying frequency on the prototype device (bi-chevron actuators). MMA-400 can generate a positive sine wave and a negative sine wave at the same time and then these actuating voltages are connected to the devices correctly to actuate these devices. The sketch of how the actuating voltage is applied on the device is as shown in Fig. 132.

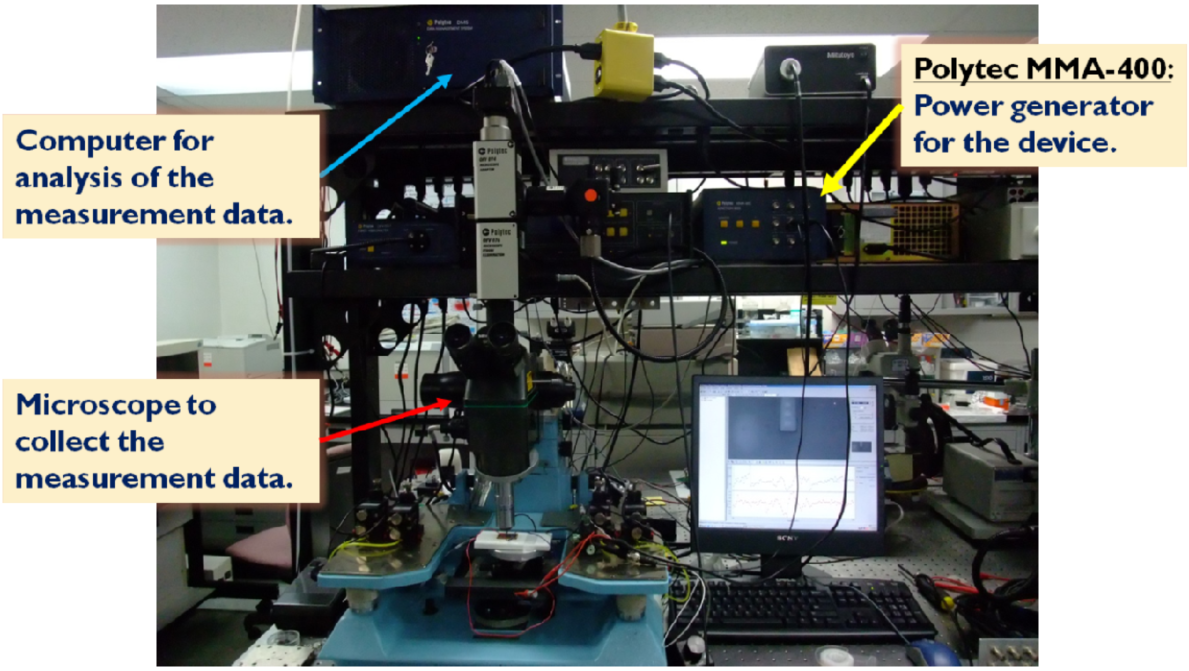

Fig. 131.  Setup of PMA for in-plane generated stroke measurement.

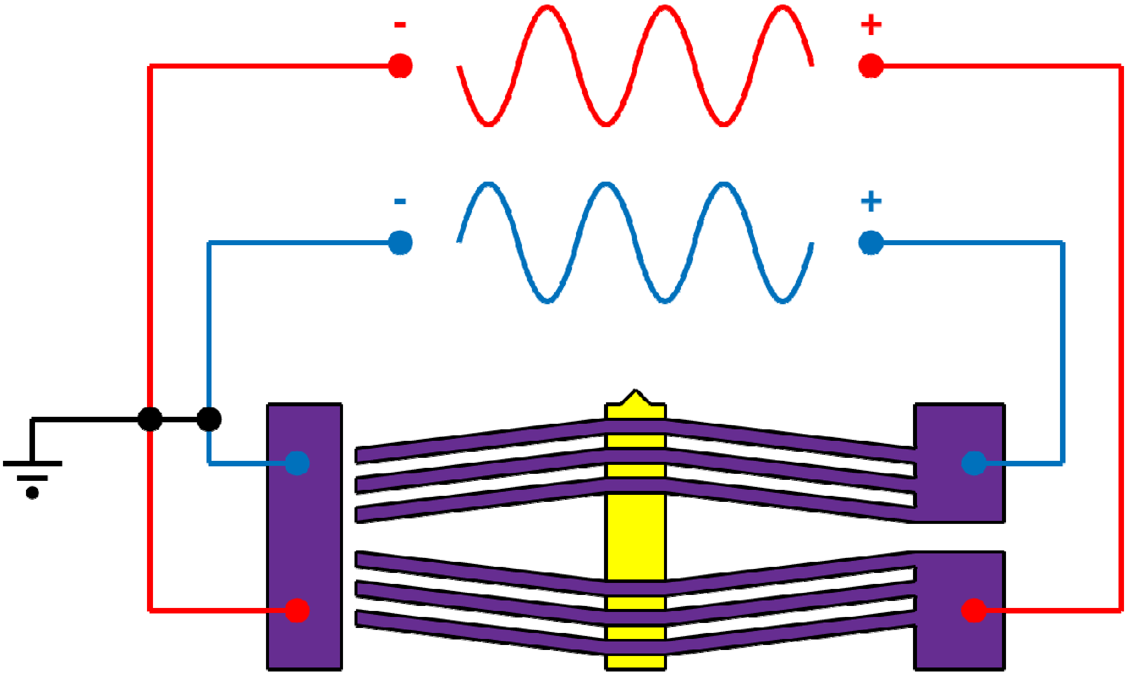

Fig. 132.  Sketch for the electrode connecting for PMA system and the device.

To measure the generated stroke under different frequency, the MPA setup actuates these devices with 10 V with actuating frequency ranging from 50 kHz to 150 kHz. The maximum voltage the PMA system can supply is 10 V and the actuating voltage for the dynamic testing is set at 10 V. In order to get a more accurate plot, the data is collected at a frequency of 500 Hz and the image is analyzed in 40 points for each frequency. With this measurement setting, the frequency spectrum of the generated stroke is as shown in Fig. 133 and Fig. 134. Fig. 133 shows the dynamic response of the pre-prototype device with 1100 µm long, 5 µm wide, 1 µm thick, and 8° AlN beams. In Fig. 133, the first in-plane resonant frequency can be observed around 70 kHz. And Fig. 134 shows the dynamic response of the pre-prototype device with 1100 µm long, 10 µm wide, 1 µm thick, and 2° AlN beams. In Fig. 134, the first in-plane resonant frequency can be observed around 60 kHz.

In Fig. 133 and Fig. 134, we can see the beam width and beam angle will influence the 1st in-plane resonant frequency and maximum generated stroke corresponding to this resonant frequency. However, in these plots, there is some noise. This noise is because the out-of-plane generated stroke effects make it difficult to accurately process the digital image and in turn calculate the in-plane generated stroke. This is one of the reasons why only a few of the devices among the devices that operate successfully during static actuation can yield sufficient dynamic response data. Another possible reason is the illumination issue. During the measurement, the illumination should be adjusted since it will vary under different frequency for the same setting. This results in dark images at particular frequency and cannot be analyzed by the digital image processing.

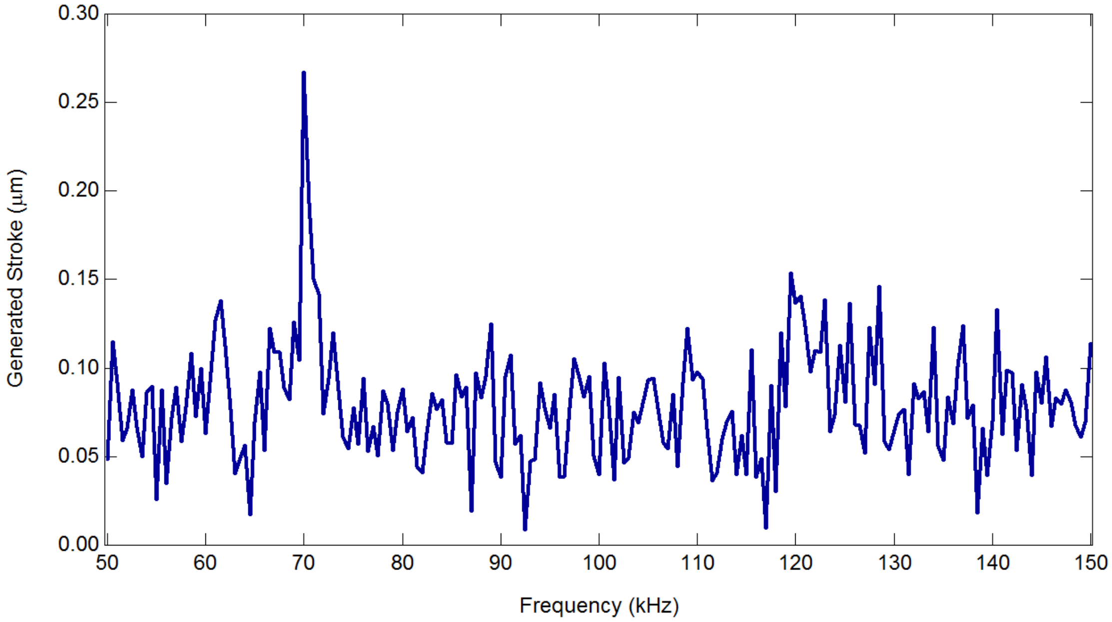

**Fig. 133. In-plane generated stroke for 1100 µm long AlN beam with 5 µm beam width and 8° beam angle.**

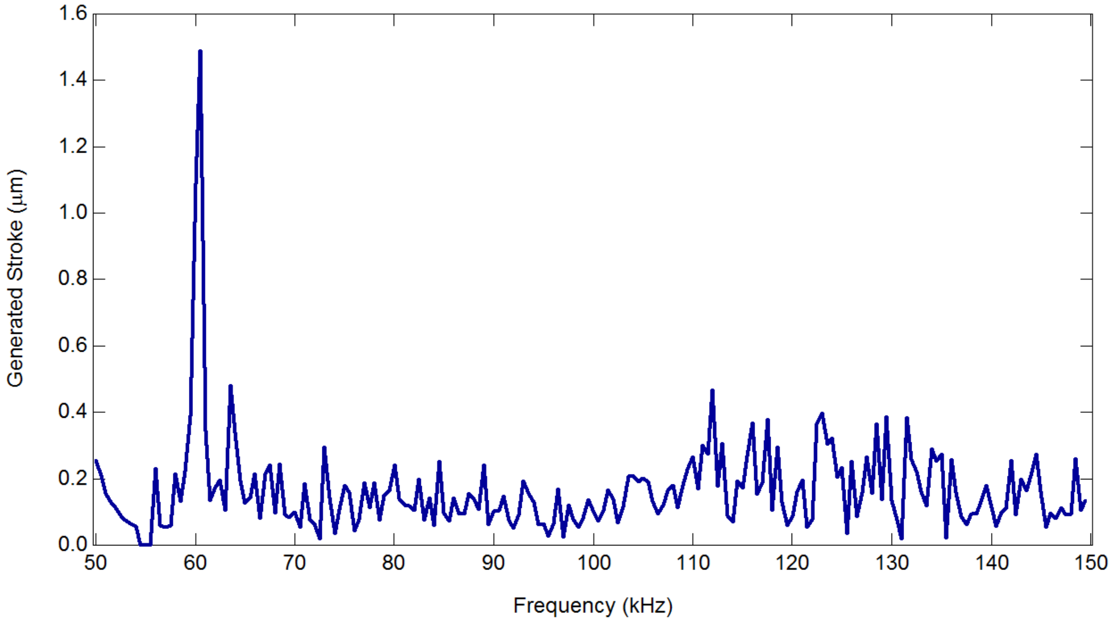

**Fig. 134. In-plane generated stroke for 1100 µm long AlN beam with 10 µm beam width and 2° beam angle.**

## 5.3 Out-of-Plane Dynamic Characteristic of Pre-Prototype Device

To evaluate the out-of-plane dynamic performance of the pre-prototype device, we will just the laser Doppler vibrometer (LDV) (as shown in Fig. 135) for the out-of-plane generated stroke measurement. In this setup, the light coming from laser source will be split into two parts. One part will go the photo-detector directly and the other part will go the measured devices. The light going the device will be reflected with a frequency shift due to Doppler effect [125]. The frequency shift is a function of the velocity of the object:

$$f_d = 2\frac{V_{object}}{\lambda} \tag{5.2}$$

where $f_d$ is the frequency shift due to the Doppler effect, $V_{object}$ is the velocity of the object, and $\lambda$ is the wavelength of the laser light. Once we compared the frequency of the lights going to the photodetector and the light going the device, we can calculate the frequency shift due to the Bragg cell and Doppler effect. Since the frequency shift ($f_b$) due to the Bragg Cell is known, we will be able to calculate $f_d$ due to Doppler effect and then calculate the velocity of the object with Equation (5.2). And the displacement and the velocity of the object have the following relationships:

$$V_{object} = 2\pi \times f_o \times S_{object} \tag{5.3}$$

where $f_o$ is the frequency of the light coming from the laser source and $S_{object}$ is the out-of –plane displacement of the object. So with Equation (3.3), we will be able to calculate the out-of-plane displacement of the object from the out-of-plane velocity of the object.

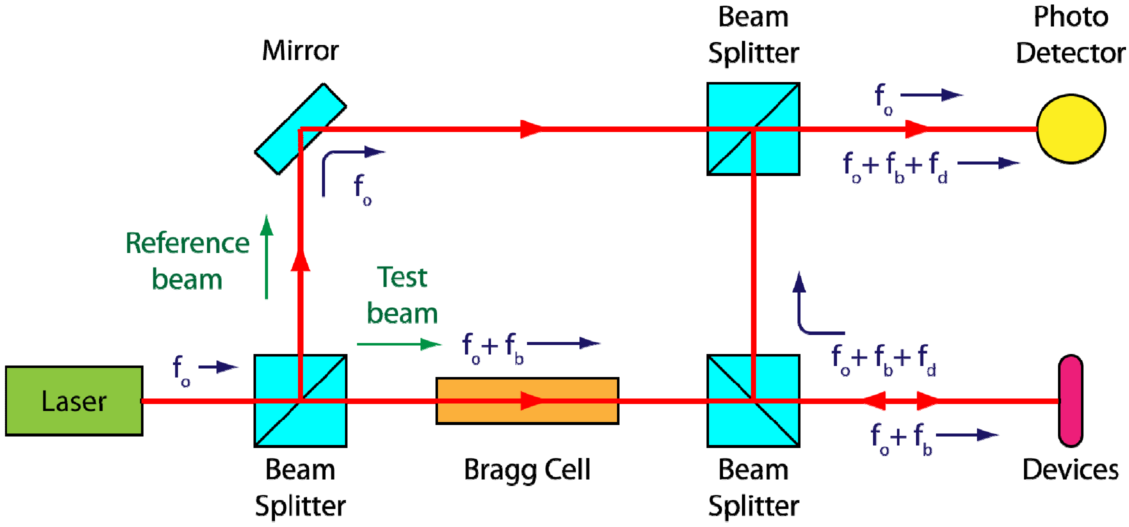

Fig. 135. Sketch of LDV for out-of-plane generated stroke measurement.

With the setup as shown in Fig. 135, we will be able to get the frequency response for out-of-plane generated stroke and the data is compared with the frequency response for in-plane generated stroke (as shown in Fig. 136). In Fig. 136, there are the frequency responses of in-plane generated stroke and out-of-plane generated stroke for a pre-prototype device with 1100 μm long AlN beam, 10 μm AlN beam width, 1μm beam thickness, and 2° AlN beam angle. The actuating voltage for this plot is 10 volts both for in-plane generated stroke and out-of-plane generated stroke.

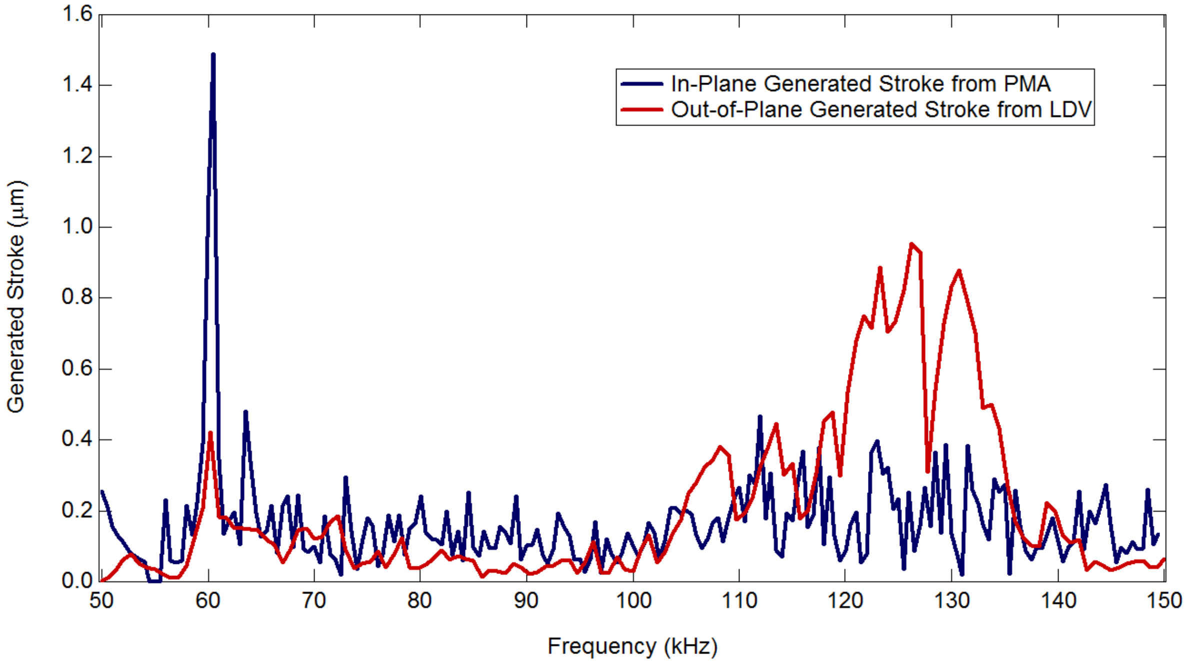

**Fig. 136. In-plane generated stroke and out-of-plane generated stroke for 1100 μm long AlN beam with 10 μm beam width and 2° beam angle.**

From Fig. 136, we find out the first in-plane resonant frequency will show up around 60 kHz. If the pre-prototype device is actuated around 60kHz, we will get in-plane generated around 1.5 μm with 10 V actuating voltage and have the acceptable out-of-plane generated stroke at the same time.

## 5.4 Static and Dynamic Characteristic of Prototype Device

The fabricated prototype device will be mounted on a package chip (as shown in Fig. 137 (A)) and then has the corresponding wire bonding geometry to actuate the prototype device (as shown in Fig. 137 (B)). After the device is measured on the setup (as shown in Fig. 124) for static measurement of generated stroke, the prototype device will have 0.3 µm generated stroke and its AlN beams are 1100 µm long, 10 µm wide, 2 µm thick, and 9 degree. The actuating voltage for this prototype device is 130 V and it will generate 65 V/µm electric field.

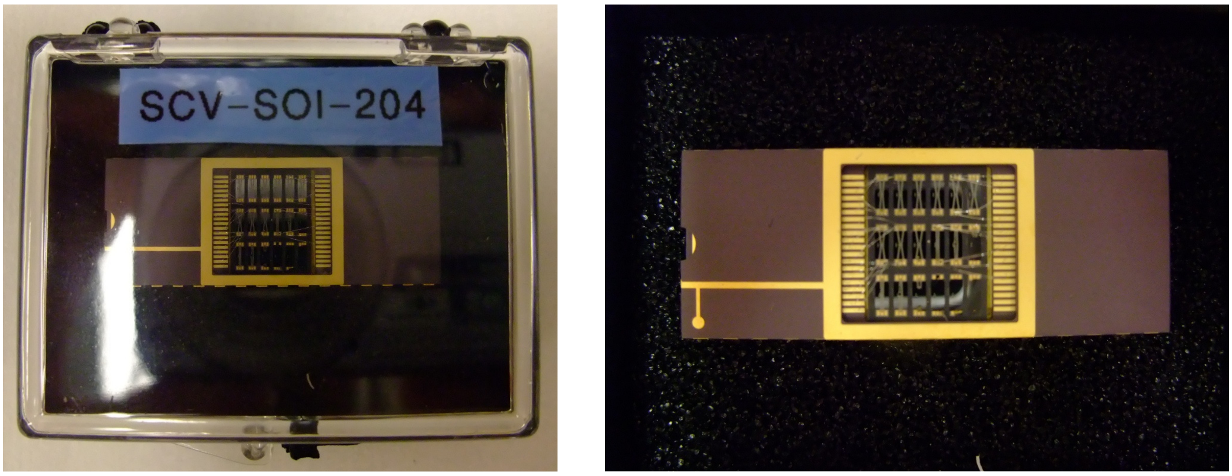

(A) Prototype devices in a package chip (B) Prototype devices with its wire-bonding

**Fig. 137. Prototype devices after mounted on the package chip and wire-bonded.**

# Chapter 6 Conclusion and Outlook

## 6.1 Conclusion

This work develops a new supercritical carbon dioxide valve system with bi-chevron AlN actuator for the advanced printing technology with supercritical carbon dioxide as the solvent. With supercritical carbon dioxide as the solvent for the ink, the ink particles generated from RESS process will be extremely small and extremely uniform and the size of these ink particles can thousand times smaller than the size of ink dye of current printing technology. Due to this excellent performance, this new printing technology should be developed for better printing quality and resolution. However, there are some design requirements while designing a valve system for this new printing technology since it has some unique characteristics. The design requirements for this supercritical carbon valve design are as shown in the following:

- High pressure application
- IC fabrication process compatibility
- High frequency operation
- High temperature stability
- Small volume for printing requirement
- Good flow control to avoid block problem

In this work, a supercritical carbon dioxide valve that meets these requirements is introduced for this new printing technology. This supercritical carbon dioxide valve is actuated by a bi-chevron AlN actuator to achieve open/close mechanism. In this valve system, AlN is chose as the piezoelectric material than PZT because of the following results:

- Integrated circuit (IC) compatible
- No external strong field and high temperature is needed for polarization process
- No compressive-stress depolarization

In addition, this actuator is designed with bi-chevron shape not only to amplify the generated stroke but also to reduce the out-of-plane stroke. This amplification mechanism is achieved by the cantilever beam structure without increasing the size significantly. And the out-of-plane generated stroke is minimized due to the symmetric design in vertical direction and in horizontal direction.

This bi-chevron AlN actuator is analyzed base on the simple model and the result shows a conflict between the generated stroke and the generated force with varying AlN beam angle. And a finite element simulator, ANSYS, is used to give more inside view about the operation of the bi-chevron AlN actuator. From the finite element simulation, the influence of the geometry on the performance is summarized as following:

- Partial top/bottom electrode coverage will influence the generated stroke and the generated force due to the uniform electric field distribution.
- Beam width will influence the generated stroke, the generated force, and the in-plane resonant frequency.
- Beam length will influence the generated stroke and the in-plane resonant frequency.
- Beam angle will influence the generated stroke, the generated force, and the in-plane resonant frequency.
- Beam thickness will only influence the generated force.

To verify the working function of the bi-chevron actuator, a pre-prototype device is introduced and fabricated. And the result from the static testing of the pre-prototype device is compared with the finite element simulation and the theoretical analysis. The result shows a very good fitting between finite element simulation and the pre-prototype device measurement. However, the error between the theoretical analysis and finite element simulation is significant due the particle top/bottom electrode coverage. For the dynamic performance, the result shows that the prototype device will give 1.5 μm in-plane generated stroke with acceptable out-of-plane generated stroke when the device is actuated in 60 kHz with 10 V actuating voltage. The pre-prototype device has 1100 μm long, 10 μm wide, and 2° angle AlN beams.

In addition to the pre-prototype device, the prototype device is fabricated and this prototype device can become goal device, supercritical carbon dioxide valve, after sealing the device with a cap. This prototype device uses a SOI wafer with bi-chevron AlN actuator to control the flow of the supercritical carbon dioxide valve. This is prototype device is also evaluated and the result verify that this fabrication process is correct.

In summary, in this work, a supercritical carbon dioxide valve is introduced to control the flow of supercritical carbon dioxide for advanced printing technology. Some unique achievements have been done in this work and are summarized as following:

- The first work introduces AlN as the piezoelectric material for actuator application.
- The first valve is design for the supercritical carbon dioxide flow application.
- The first actuator design can work under a pressure as high as 30 MPa.
- The valve design can generate two dimensional flow rather than three dimensional flow for better control on the flow.
- The static and dynamic performances of fabricated bi-chevron AlN actuators are verified with the finite element simulation and theoretical analysis and give a satisfying result.

Although this work has verified the future development for the supercritical carbon dioxide valve design, there are more that we should improve to really bring this design to commercialization and they will be discussed in the following section.

## 6.2 Outlook

In order to further demonstration this technology and bring it to commercialization, the analysis and fabrication of the supercritical carbon dioxide valve should be improved for better performance of the devices. What can be improved will be discussed in the following.

### 6.2.1 Fluidic Simulation for Supercritical Carbon Dioxide Flow

When the supercritical carbon dioxide goes through the SCV system, it will transfer its state from supercritical carbon dioxide to gas carbon dioxide. This transformation is very critical for the fluidic performance of the system and should be characterized carefully. However, there is no commercial software for such kind of simulation. In the future work, if the fluidic simulation for the supercritical carbon dioxide flow can be developed, the fluidic performance of the SCV system can be optimized.

### 6.2.2 Stress Gradient Control for AlN Thin film

The stress control of the AlN thin film is very critical for the fabrication process of the prototype devices since bad stress control will induce the fail of the devices. In the previous fabrication process, the stress is controlled between 0~100 MPa tensile. This stress control is focus on the average stress control. However, in the future work, the stress gradient in the thickness direction should be minimized since it will induce the buckling of the AlN beams.

### 6.2.3 Orientation Control for AlN Thin film

In addition to the stress gradient control of the AlN thin film, the crystal orientation control of AlN thin film is very important, too. For the future work, the full width of half maximum from rocking curve of the AlN thin film should be minimized since it means a better piezoelectric quality.

### 6.2.4 Stability for the Vapor HF Etch

The etch rate of the vapor HF that is used to release the prototype device is not very stable. The process parameter for the releasing should be optimized for more stable etch rate. Or the cleanline of the etch chamber should be improved to avoid any change of the etch rate.

### 6.2.5 Step coverage of TEOS oxide

TEOS oxide is used in the fabrication process to fill the trench. The step coverage should be improved to minimize the TEOS thickness needed to fill the trench. The step coverage can be improved by adjusting the pressure, temperature, and $O_2$/TEOS ratio.

### 6.2.6 Resolution of Bonding Alignment

The leakage of the valve system is determined by how performance the bonding of device wafer and cape wafer. The resolution of bonding alignment should be minimized for less leakage.

These suggestions include the analysis, fabrication, and package. If these suggestions are really achieved in the future, the performance of the device can be improved. These suggestions will be applied for the future work and then lead to the commercialization of the supercritical carbon dioxide valve.

# Appendix A. Constitutive Equations for Piezoelectric Material

The constitutive equations for piezoelectric material are as shown in the following:

$$\{T\} = [c^E]\{S\} - [e]^T\{E\}$$

$$[T] = [c^E][S] - [e]^T[E]$$

$$\underline{\underline{T}} = \underline{\underline{\underline{\underline{c}}}}^E : \underline{\underline{S}} - \underline{\underline{\underline{e}}}^T \cdot \underline{E}$$

$$\{D\} = [e]\{S\} + [\varepsilon^S]\{E\}$$

$$[D] = [e][S] + [\varepsilon^S][E]$$

$$\underline{D} = \underline{\underline{\underline{e}}} : \underline{\underline{S}} + \underline{\underline{\varepsilon}}^S \cdot \underline{E}$$

$\{T\}$: stress tensor

$\{S\}$: strain tensor

$\{D\}$: electric flux density

$\{E\}$: electric field

$[c^E]$: tensor of elastic moduli

$[\varepsilon^S]$: dielectric constant

$[e]$: piezoelectric stress matrix

The coupled equations for piezoelectric material from Mechanical field (Navier's equations) are as following:

$$\{f_b\} + \nabla \cdot \{T\} = \rho\{\ddot{u}\}$$

$$\underline{f_b} + \nabla \cdot \underline{\underline{T}} = \rho\underline{\ddot{u}}$$

$$\{S\} = \nabla\{u\}$$

$$\underline{\underline{S}} = \nabla\underline{u}$$

$\{u\}$: mechanical displacement

$\{f_b\}$: mechanical body force

From Maxwell's equation, the following equation will be applied in electrostatic field

$$\nabla \cdot \{D\} = -q_b$$

$$\nabla \cdot \underline{D} = -q_b$$

$$\nabla \times \{E\} = 0$$

$$\nabla \times \underline{E} = 0$$

$$\{E\} = -\nabla V$$

$$\underline{E} = -\nabla V$$

And

$$\{D\} \cdot \{n\} = -q_t$$

$$\underline{D} \cdot \underline{n} = -q_t$$

$V$: scalar electrical potential

$q_b$: free electric charge density

$q_t$: surface electric charge density

Coupled field equations

1. $\{f\} + \nabla \cdot \{\sigma\} = \rho\{\ddot{u}\}$

$$\{f_b\} + \nabla \cdot \{T\} = \rho\{\ddot{u}\}$$

$$\{f_b\} + \nabla \cdot \left[[c^E]\{S\} - [e]^T\{E\}\right] = \rho\{\ddot{u}\}$$

$$\{f_b\} + \nabla \cdot \left[[c^E]\{S\} + [e]^T\nabla V\right] = \rho\{\ddot{u}\}$$

$$\rho\{\ddot{u}\} - \nabla\cdot\left[[c^E]\{S\} + [e]^T\nabla V\right] - \{f_b\} = 0$$

$$\underline{f_b} + \nabla\cdot\underline{\underline{\sigma}} = \rho\underline{\ddot{u}}$$

$$\underline{f_b} + \nabla\cdot\left[\underline{\underline{\underline{\underline{c}}}}^E : \underline{\underline{S}} - \underline{\underline{\underline{e}}}^T\cdot\underline{E}\right] = \rho\underline{\ddot{u}}$$

$$\underline{f_b} + \nabla\cdot\left[\underline{\underline{\underline{\underline{c}}}}^E : \underline{\underline{S}} + \underline{\underline{\underline{e}}}^T\cdot\nabla V\right] = \rho\underline{\ddot{u}}$$

$$\rho\underline{\ddot{u}} - \nabla\cdot\left[\underline{\underline{\underline{\underline{c}}}}^E : \underline{\underline{S}} + \underline{\underline{\underline{e}}}^T\cdot\nabla V\right] - \underline{f_b} = 0$$

2. $\nabla\cdot\{D\} = 0$

$$\nabla\cdot\{D\} = q_b$$

$$\nabla\cdot\left[[e]\{S\} + [\varepsilon^S]\{E\}\right] = q_b$$

$$\nabla\cdot\left[[e]\{S\} - [\varepsilon^S]\nabla V\right] = q_b$$

$$\nabla\cdot\underline{D} = q_b$$

$$\nabla\cdot\left[\underline{\underline{\underline{e}}} : \underline{\underline{S}} + \underline{\underline{\varepsilon}}^S\cdot\underline{E}\right] = q_b$$

$$\nabla\cdot\left[\underline{\underline{\underline{e}}} : \underline{\underline{S}} - \underline{\underline{\varepsilon}}^S\cdot\nabla V\right] = q_b$$

Strong form

$$\rho\{\ddot{u}\} - \nabla\cdot\left[[c^E]\{S\} + [e]^T\nabla V\right] - \{f_b\} = 0$$

$$\nabla\cdot\left[[e]\{S\} - [\varepsilon^S]\nabla V\right] = q_b$$

$$\rho\underline{\ddot{u}} - \nabla\cdot\left[\underline{\underline{\underline{\underline{c}}}}^E : \underline{\underline{S}} + \underline{\underline{\underline{e}}}^T\cdot\nabla V\right] - \underline{f_b} = 0$$

$$\nabla\cdot\left[\underline{\underline{\underline{e}}}:\underline{\underline{S}}-\underline{\underline{\varepsilon^S}}\cdot\nabla V\right]=q_b$$

Weak form

$$\rho\{\ddot{u}\}-\nabla\cdot\left[[c^E]\{S\}+[e]^T\nabla V\right]-\{f_b\}=0$$

$$\rho\underline{\ddot{u}}-\nabla\cdot\left[\underline{\underline{\underline{\underline{c^E}}}}:\underline{\underline{S}}+\underline{\underline{\underline{e^T}}}\cdot\nabla V\right]-\underline{f_b}=0$$

If the material is static, the acceleration is zero and then

$$-\nabla\cdot\left[[c^E]\{S\}+[e]^T\nabla V\right]-\{f_b\}=0$$

$$-\nabla\cdot\left[\underline{\underline{\underline{\underline{c^E}}}}:\underline{\underline{S}}+\underline{\underline{\underline{e^T}}}\cdot\nabla V\right]-\underline{f_b}=0$$

Integral to get weak form

$$\int_\Omega\left[-\nabla\cdot\underline{\underline{T}}-\underline{f_b}\right]\cdot\underline{v}d\Omega=0$$

$$\int_\Omega\left[-\nabla\cdot\left(\underline{\underline{\underline{\underline{c^E}}}}:\underline{\underline{S}}+\underline{\underline{\underline{e^T}}}\cdot\nabla V\right)-\underline{f_b}\right]\cdot\underline{v}d\Omega=0$$

And

$$\nabla\cdot\left(\underline{\underline{T}}\cdot\underline{v}\right)=\left(\nabla\cdot\underline{\underline{T}}\right)\cdot\underline{v}+\underline{\underline{T}}:\left(\nabla\underline{v}\right)$$

$$\left(\nabla\cdot\underline{\underline{T}}\right)\cdot\underline{v}=\nabla\cdot\left(\underline{\underline{T}}\cdot\underline{v}\right)-\underline{\underline{T}}:\left(\nabla\underline{v}\right)$$

And then

$$\int_\Omega\left[-\nabla\cdot\underline{\underline{T}}-\underline{f_b}\right]\cdot\underline{v}d\Omega=0$$

$$\int_\Omega\left[-\left(\nabla\cdot\underline{\underline{T}}\right)\cdot\underline{v}-\underline{f_b}\cdot\underline{v}\right]d\Omega=0$$

$$\int_\Omega\left[-\nabla\cdot\left(\underline{\underline{T}}\cdot\underline{v}\right)+\underline{\underline{T}}:\left(\nabla\underline{v}\right)-\underline{f_b}\cdot\underline{v}\right]d\Omega=0$$

$$-\int_{\Omega} \nabla\cdot\left(\underline{\underline{T}}\cdot\underline{v}\right)d\Omega+\int_{\Omega} \underline{\underline{T}}:\left(\nabla\underline{v}\right)d\Omega-\int_{\Omega} \underline{f_b}\cdot\underline{v}d\Omega=0$$

Because

$$\int_{\Omega} \nabla\cdot\underline{v}d\Omega=\int_{\partial\Omega}\underline{v}\cdot\underline{n}d\mathrm{A}$$

$$\int_{\Omega} \nabla\cdot\left(\underline{\underline{T}}\cdot\underline{v}\right)d\Omega=\int_{\partial\Omega}\left(\underline{\underline{T}}\cdot\underline{v}\right)\cdot\underline{n}d\mathrm{A}$$

So

$$-\int_{\Omega} \left(\underline{\underline{T}}\cdot\underline{v}\right)\cdot\underline{n}d\Omega+\int_{\Omega} \underline{\underline{T}}:\left(\nabla\underline{v}\right)d\Omega-\int_{\Omega} \underline{f_b}\cdot\underline{v}d\Omega=0$$

$$-\int_{\partial\Omega}\underline{v}\cdot\underline{t}d\mathrm{A}+\int_{\Omega} \underline{\underline{T}}:\left(\nabla\underline{v}\right)d\Omega-\int_{\Omega} \underline{f_b}\cdot\underline{v}d\Omega=0$$

$$-\int_{\partial\Omega}\underline{v}\cdot\underline{f_t}d\mathrm{A}+\int_{\Omega} \left[\underline{\underline{\underline{\underline{c^E}}}}:\underline{\underline{S}}+\underline{\underline{\underline{e}}}^T\cdot\nabla V\right]:\left(\nabla\underline{v}\right)d\Omega-\int_{\Omega} \underline{f_b}\cdot\underline{v}d\Omega=0$$

$$-\int_{\partial\Omega}\underline{v}\cdot\underline{f_t}d\mathrm{A}+\int_{\Omega} \nabla\underline{v}:\underline{\underline{\underline{\underline{c^E}}}}:\nabla\underline{u}d\Omega+\int_{\Omega} \nabla\underline{v}:\underline{\underline{\underline{e}}}^T\cdot\nabla Vd\Omega-\int_{\Omega} \underline{f_b}\cdot\underline{v}d\Omega=0$$

$$-\int_{\partial\Omega}\underline{f_t}\cdot\underline{t}d\mathrm{A}+\int_{\Omega} \nabla\underline{v}:\underline{\underline{\underline{\underline{c^E}}}}:\nabla\underline{u}d\Omega+\int_{\Omega} \nabla\underline{v}:\underline{\underline{\underline{e}}}^T\cdot\nabla Vd\Omega-\int_{\Omega} \underline{v}\cdot\underline{f_b}d\Omega=0$$

Weak form

$$\nabla\cdot\underline{D}=q_b$$

$$\nabla\cdot\left[\underline{\underline{\underline{e}}}:\underline{\underline{S}}-\underline{\underline{\varepsilon^S}}\cdot\nabla V\right]=q_b$$

$$\int_{\Omega} \left[\nabla\cdot\underline{D}-q_b\right]wd\Omega=0$$

Because

$$\nabla\cdot\left(\underline{D}w\right)=\left(\nabla\cdot\underline{D}\right)w+\underline{D}\cdot\left(\nabla w\right)$$

$$\left(\nabla\cdot\underline{D}\right)w=\nabla\cdot\left(\underline{D}w\right)-\underline{D}\cdot\left(\nabla w\right)$$

So

$$\int_{\Omega} \left[\nabla \cdot \underline{D} - q_b\right] w d\Omega = 0$$

$$\int_{\Omega} \left[\nabla \cdot \left(\underline{D} w\right) - \underline{D} \cdot (\nabla w) - q_b w\right] d\Omega = 0$$

$$\int_{\Omega} \nabla \cdot \left(\underline{D} w\right) d\Omega - \int_{\Omega} \underline{D} \cdot \nabla w d\Omega - \int_{\Omega} q_b w d\Omega = 0$$

$$\int_{\partial\Omega} \underline{D} w \cdot \underline{n} d\mathrm{A} - \int_{\Omega} \underline{D} \cdot \nabla w d\Omega - \int_{\Omega} q_b w d\Omega = 0$$

$$\int_{\partial\Omega} w \underline{D} \cdot \underline{n} d\mathrm{A} - \int_{\Omega} \nabla w \cdot \underline{D} d\Omega - \int_{\Omega} w q_b d\Omega = 0$$

$$\int_{\partial\Omega} w \underline{D} \cdot \underline{n} d\mathrm{A} - \int_{\Omega} \nabla w \cdot \left[\underline{\underline{\underline{e}}} : \underline{\underline{S}} + \underline{\underline{\varepsilon^S}} \cdot \underline{E}\right] d\Omega - \int_{\Omega} w q_b d\Omega = 0$$

$$\int_{\partial\Omega} w \underline{D} \cdot \underline{n} d\mathrm{A} - \int_{\Omega} \nabla w \cdot \left[\underline{\underline{\underline{e}}} : \underline{\underline{S}} - \underline{\underline{\varepsilon^S}} \cdot \nabla V\right] d\Omega - \int_{\Omega} w q_b d\Omega = 0$$

$$\int_{\partial\Omega} w \underline{D} \cdot \underline{n} d\mathrm{A} - \int_{\Omega} \nabla w \cdot \underline{\underline{\underline{e}}} : \underline{\underline{S}} d\Omega + \int_{\Omega} \nabla w \cdot \underline{\underline{\varepsilon^S}} \cdot \nabla V d\Omega - \int_{\Omega} w q_b d\Omega = 0$$

$$-\int_{\partial\Omega} w q_t d\mathrm{A} - \int_{\Omega} \nabla w \cdot \underline{\underline{\underline{e}}} : \underline{\underline{S}} d\Omega + \int_{\Omega} \nabla w \cdot \underline{\underline{\varepsilon^S}} \cdot \nabla V d\Omega - \int_{\Omega} w q_b d\Omega = 0$$

$$-\int_{\partial\Omega} w q_t d\mathrm{A} - \int_{\Omega} \nabla w \cdot \underline{\underline{\underline{e}}} : \nabla \underline{u} d\Omega + \int_{\Omega} \nabla w \cdot \underline{\underline{\varepsilon^S}} \cdot \nabla V d\Omega - \int_{\Omega} w q_b d\Omega = 0$$

So we get the two weak form equations

$$-\int_{\partial\Omega} \underline{v} \cdot \underline{f_t} d\mathrm{A} + \int_{\Omega} \nabla \underline{v} : \underline{\underline{\underline{\underline{c^E}}}} : \nabla \underline{u} d\Omega + \int_{\Omega} \nabla \underline{v} : \underline{\underline{\underline{e}}}^T \cdot \nabla V d\Omega - \int_{\Omega} \underline{v} \cdot \underline{f_b} d\Omega = 0$$

$$-\int_{\partial\Omega} w q_t d\mathrm{A} - \int_{\Omega} \nabla w \cdot \underline{\underline{\underline{e}}} : \nabla \underline{u} d\Omega + \int_{\Omega} \nabla w \cdot \underline{\underline{\varepsilon^S}} \cdot \nabla V d\Omega - \int_{\Omega} w q_b d\Omega = 0$$

Let

$$\underline{v} = \{v\}$$

$$\underline{u} = \{u\}$$

$$\underline{t} = \{t\}$$

$$\nabla\underline{v} = [D_u]\{v\}$$

$$\nabla\underline{u} = [D_u]\{u\}$$

$$\underline{\underline{\underline{\underline{c^E}}}} = [c^E]$$

$$\underline{\underline{\underline{e^T}}} = [e]^T$$

$$\underline{f} = \{f\}$$

$$\nabla w = [D_V]w$$

$$\nabla V = [D_V]V$$

$$\underline{\underline{\varepsilon^S}} = [\varepsilon^s]$$

With these symbol

$$-\int_{\partial\Omega}\{v\}^T\{f_t\}d\mathrm{A} + \int_{\Omega}([D_u]\{v\})^T[c^E]([D_u]\{u\})d\Omega + \int_{\Omega}([D_V]\{v\})^T[e]^T([D_V]V)d\Omega - \int_{\Omega}\{v\}^T\{f_b\}d\Omega = 0$$

$$-\int_{\partial\Omega}wq_t dA - \int_{\Omega}([D_V]w)^T[e]([D_u]\{u\})d\Omega + \int_{\Omega}([D_V]w)\,[\varepsilon^S]([D_V]V)d\Omega - \int_{\Omega}wq_b d\Omega = 0$$

Let

$$\{u\} = [\phi_u]\{a\}$$

$$\{v\} = [\phi_u]\{b\}$$

$$V = [\phi_V]\{c\}$$

$$w = [\phi_V]\{d\}$$

And then

$$-\int_{\partial\Omega}\{v\}^T\{f_t\}d\mathrm{A}+\int_{\Omega}([D_u]\{v\})^T[c^E]([D_u]\{u\})d\Omega+\int_{\Omega}([D_u]\{v\})^T[e]^T([D_V]V)d\Omega$$
$$-\int_{\Omega}\{v\}^T\{f_b\}d\Omega=0$$

$$-\int_{\partial\Omega}([\phi_u]\{b\})^T\{f_t\}d\mathrm{A}+\int_{\Omega}\big([D_u]([\phi_u]\{b\})\big)^T[c^E]([D_u][\phi_u]\{a\})d\Omega$$
$$+\int_{\Omega}\big([D_u]([\phi_u]\{b\})\big)^T[e]^T([D_V][\phi_V]\{c\})d\Omega-\int_{\Omega}([\phi_u]\{b\})^T\{f_b\}d\Omega$$
$$=0$$

$$-\int_{\partial\Omega}wq_t dA-\int_{\Omega}([D_V]w)^T[e]([D_u]\{a\})d\Omega+\int_{\Omega}([D_V]w)^T\,[\varepsilon^S]([D_V]V)d\Omega-\int_{\Omega}wq_b d\Omega=$$
$$=0$$

$$-\int_{\partial\Omega}([\phi_V]\{d\})^T q_b dA-\int_{\Omega}([D_V][\phi_V]\{d\})^T[e]([D_u][\phi_u]\{a\})d\Omega$$
$$+\int_{\Omega}([D_V][\phi_V]\{d\})\,[\varepsilon^S]([D_V][\phi_V]\{c\})d\Omega-\int_{\Omega}([\phi_V]\{d\})^T q_b d\Omega==0$$

Rearrange the two above equations

$$-\int_{\partial\Omega}([\phi_u]\{b\})^T\{f_T\}d\mathrm{A}+\int_{\Omega}\big([D_u]([\phi_u]\{b\})\big)^T[c^E]([D_u][\phi_u]\{a\})d\Omega$$
$$+\int_{\Omega}\big([D_u]([\phi_u]\{b\})\big)^T[e]^T([D_V][\phi_V]\{c\})d\Omega$$
$$-\int_{\Omega}([D_u][\phi_u]\{b\})^T\{f_b\}d\Omega=0$$

$$-\int_{\partial\Omega}([\phi_V]\{d\})^T q_t dA-\int_{\Omega}([D_V][\phi_V]\{d\})^T[e]([D_u][\phi_u]\{a\})d\Omega$$
$$+\int_{\Omega}([D_V][\phi_V]\{d\})\,[\varepsilon^S]([D_V][\phi_V]\{c\})d\Omega-\int_{\Omega}([\phi_V]\{d\})^T q_b d\Omega=0$$

$$\{b\}^T\big[[K_{uu}]\{a\}+[K_{uV}]\{c\}-\{F\}\big]=0$$

$$\{d\}^T\big[[K_{Vu}]\{a\}+[K_{VV}]\{c\}-\{Q\}\big]=0$$

Where

$$[K_{uu}] = \int_{\Omega} ([D_u][\phi_u])^T [c^E]([D_u][\phi_u]) d\Omega$$

$$[K_{uV}] = \int_{\Omega} ([D_u][\phi_u])^T [e]^T ([D_V][\phi_V]) d\Omega$$

$$\{R\} = \int_{\partial\Omega} [\phi_u]^T \{f_t\} d\mathrm{A} + \int_{\Omega} [\phi_u]^T \{f_b\} d\Omega$$

$$[K_{Vu}] = \int_{\Omega} ([D_V][\phi_V])^T [e]([D_u][\phi_u]) d\Omega$$

$$[K_{VV}] = -\int_{\Omega} ([D_V][\phi_V])^T [\varepsilon^S]([D_V][\phi_V]) d\Omega$$

$$\{Q\} = -\int_{\partial\Omega} ([\phi_V])^T q_t \, dA - \int_{\Omega} ([\phi_V])^T q_b \, d\Omega$$

# Appendix B. Material Properties of Aluminum Nitride

The material properties of AlN that we used for all FEM simulation are as shown in the following:

- Stiffness matrix

$$[c] = \begin{bmatrix} 3.45 & 1.25 & 1.20 & 0 & 0 & 0 \\ 1.25 & 3.45 & 1.20 & 0 & 0 & 0 \\ 1.20 & 1.20 & 3.95 & 0 & 0 & 0 \\ 0 & 0 & 0 & 1.18 & 0 & 0 \\ 0 & 0 & 0 & 0 & 1.18 & 0 \\ 0 & 0 & 0 & 0 & 0 & 1.10 \end{bmatrix} \left(10^{11}\, {}^{N}\!/_{m^2}\right)$$

- Piezoelectric stress matrix

$$[e] = \begin{bmatrix} 0 & 0 & 0 & 0 & -0.48 & 0 \\ 0 & 0 & 0 & -0.48 & 0 & 0 \\ -0.58 & -0.58 & 1.55 & 0 & 0 & 0 \end{bmatrix} \left({}^{C}\!/_{m^2}\right)$$

- Piezoelectric strain matrix

$$[d] = \begin{bmatrix} 0 & 0 & 0 & 0 & -4.068 & 0 \\ 0 & 0 & 0 & -4.068 & 0 & 0 \\ -2.646 & -2.646 & 5.532 & 0 & 0 & 0 \end{bmatrix} \left(10^{-12}\, {}^{m}\!/_{V}\right)$$

- Dielectric matrix

$$[\varepsilon] = \begin{bmatrix} 8.0 & 0 & 0 \\ 0 & 8.0 & 0 \\ 0 & 0 & 9.5 \end{bmatrix} \left(10^{-11}\, {}^{F}\!/_{m}\right)$$

- Breakdown electric field

$$E_B = 1400\, {}^{kV}\!/_{cm}$$

# References

1. A. S. Pensado, A. A. H. Padua, M. J. P. Comunas, and J. Fernandez, “Viscosity and density measurement for carbon dioxide + pentaerythritol ester lubricant mixtures at low lubricant”, The Journal of Supercritical Fluids, Vol. 44, Issue 2, pp. 172-185, 2008.
2. E. M. Berends, O. S. L. Bruinsma, and G. M. van Rosmalen, “Nucleation and growth of fine crystals from supercritical carbon dioxide”, Journal of Crystal Growth, Vol. 128, Issue 1-4, pp. 50-56, 1993.
3. R. Jagannathan and G. C. Irvin, “Nanofluids: A New Class of Materials Produced from Nanoparticles Assemblies”, Advanced Functional Materials, Vol. 15, Issue 9, pp. 1501-1510, 2005
4. R. Jagannathan and R. V. Mehta, “Continuous, Atmospheric Process to Create Organic Clusters and Nanostructured, Functional Films”, Advanced Functional Materials, Vol. 16, Issue 5, pp. 633-639, 2006
5. R. Jagannathan, G. Irvin, T. Blanton, and S. Jagannathan, “Organic Nanoparticles: Preparation, Self-Assembly, and Properties”, Advanced Functional Materials, Vol. 16, Issue 6, pp. 747-753, 2006
6. K. W. Oh and C. H. Ahn, “A review of microvalves”, Journal of Micromechanicals and Microengineering, Vol. 16, No. 5, pp. R13-39, 2006.
7. S. T. Terry, J. H. Jerman, and J. B. Angell, “A Gas Chromatographic Air Analyzer Fabricated on a Silicon Wafer”, IEEE Transactions on Electron Devices, Vol. ED-26, No. 12, pp. 1880-1885, 1979.
8. K. Yanagisawa, H. Kuwano, and A. Tago, “Electromagetically driven microvalve”, Microsystem Technologies, Vol. 2, No. 1, pp. 22-25, 1995.
9. K. I. Arai and T. Honda, “Micromagnetic actuator”, Robotica, vol. 14, pp. 477-481, 1996.
10. D. J. Sadler, K. W. Oh, C. H. Ahn, S. Bhansali, and H. T. Henderson, “A new magnetically actuated microvalve for liquid and gas control application”, The 10th International Conference on Solid-State Sensor and Actuator (Transducers ‘99), pp. 1812-1815, 1999.
11. M. Capanu, J. G. Boyd, and P. J. Hesketh, “Design, Fabrication, and Testing of a Bistable Electromagnetically Actuated Microvalve”, Journal of Microelectromagnetical Systems, Vol. 9, No, 2, pp. 181-189, 2000.
12. K. Sato and M. Shikida, “An electrostatically actuated gas valve with an s-shape film element”, J. Micromech. Microeng., Vol. 4, No. 4, pp. 205-209, 1994.
13. M. Shikida, K. Sato, S. Tanaka, T. Kawamura, and Y. Fujuisaki, “Electrostatically Driven Gas Valve with High Conductance”, Journal of Microelectromechanical Systems, Vol. 3, No. 2, pp. 76-80.
14. C. Goll, W. Bacher, B. Bustgens, D. Maas, R. Ruprecht, and W. K. Schomburg, “An electrostatically actuated polymer microvalve equipped with a movable membrane electrode”, Vol. 7, Issue 3, pp. 224-226, 1997.

15. J. K. Robertson and K. D. Wise, "A low pressure micromachined flow modulator", Sensors and Actuators, Vol. 71, Issue 1-2, pp. 98-106, 1998
16. J. Schaible, J. Vollmer, R. Zengerle, H. Sandmaier, and T. Strobelt, "Electrostatic microvalves in silicon with 2-way function for industrial applications", The 11th International Conference on Solid-State Sensor and Actuators, 2001.
17. W. V. D. Wijngaart, H. Ask, P. Enoksson, G. Stemme, "A high-stroke, high-pressure electrostatic actuator for valve applications", Sensor and Actuators A, Vol. 100, Issue 2-3, pp. 264-271, 2002.
18. L. Yobas, M. A. Muff, F. J. Lisy, and D. M. Durand, "A Novel Bulk-Micromachined Electrostatic Microvalve with a Curved-Compliant Structure Applicable for a Pneumatic Tactile Display", Journal of Microelectromechanical Systems, Vol. 10, No.2, pp. 187-196, 2001
19. L. Yobas, D. M. Durand, G. G. Skebe, F. J. Lisy, and M. A. Huff, "A Novel Integrable Microvalve for Refreshable Braille Display System", Journal of Microelectromechanical Systems, Vol. 12, No.3, pp. 252-263, 2003.
20. X. Yang, A. Holke, S. A. Jacobson, J. H. Lang, M. A. Schmidt, S. D. Umans, "A Electrostatic, On/Off Microvalve Designed for Gas Fuel Delivery for the MIT Microengine", Journal of Microelectromechanical Systems, Vol. 13, No. 4, pp. 660-668, 2004.
21. D. Petrov, W. Lang and W. Benecke, "A nickel electrostatic curved beam actuator for valve applications", Procedia Engineering, Vol. 5, pp. 1409-1412, 2010.
22. H. Jerman, "Electrically-Activated, Normally-Closed Diaphragm Valves", Solid-State Sensors and Actuators, Transducers '91, pp. 1045-1048, 1991.
23. P. W. Barth, "Silicon Microvalve for Gas Flow Control", Solid-State Sensors and Actuators, 1995 and Eurosensors IX., Transducers '95, pp. 276-279, 1995.
24. X. Yang, C. Grosjean, Y.-C. Tai, and C-M. Ho, "A MEMS thermopneumatic silicone rubber membrane valve", Sensors and Actuators A, Vol. 64, Issue 1, pp. 101-108, 1998.
25. A. Ruzzu, K. Bade, J. Fahrenberg, and D. Maas, "Positioning system for catheter tips based on an active microvalve system", Journal of Micromechanics and Microengineering, Vol. 8, No. 2, pp. 161-164, 1998.
26. X. Yang, C. Grosjean, and Y.-C. Tai, "Design, Fabrication, and Testing of Micromachined Silicone Rubber Membrane Valves", Journal of Microelectromechanical Systems, Vol. 8, No. 4, pp. 393-402, 1999
27. D. Baechi and R. Buser, "Suspension Handling System", Sensors and Actuators B: Chemical, Vol. 63, Issue 3, pp. 195-200, 2000
28. D. Baechi, J. Dual, and R. Buser, "A high density microchannel network with integrated valves and photodiodes", Micro Electro Mechanical Systems, 2001, pp. 463-466, 2001.
29. A. Luque and J. M. Quero, "High pressure valves in MEMS: theory and applications", Industrial Electronics Society, IEEE 2002 28th Annual Conference, Vol. 4, pp. 3057-3061, 2002.

30. C. A. Rich, and K. D. Wise, "A High-Flow Thermopneumatic Microvalve with Improved Efficiency and Integrated State Sensing", Journal of Microelectromechanical Systems, Vol. 12, No. 2, pp. 201-208, 2003
31. S. Tomonari, H. Yoshida, M. Kamakura, K. Yoshida, K. Kawahito, M. Saitoh, H. Kawada, S. juodkazis, and H. Misawa, "Efficient Microvalve Driven by a Si-Ni Bimorph", Jpn. J. Appl. Phys., Vol. 42, Part 1, No. 7A, pp. 4593-4597, 2003.
32. J. –H. Kim, K.-H. Na, C. J. Kang, D. Jeon, Y.-S. Kim, "A disposable thermopneumatic-actuated microvalve stacked with PDMS layers and ITO-coated glass", Microelectronic Engineering, Vol. 73-74, pp. 864-869, 2004
33. H. Takao, K. Miyamura, H. Ebi, M. Ashiki, K. Sawada, and M. Ishida, "A MEMS microvalve with PDMS diaphragm and two-chamber configuration of thermo-pneumatic actuator for integrated blood test system on silicon", Sensors and Actuators A, Vol. 119, Issue 2, pp. 468-475, 2005.
34. A. Luque, J. M. Quero, C. Hibert, P. Fluckiger, and A. M. Ganan-Calvo, "Integrable silicon microfluidic valve with pneumatic actuation", Sensors and Actuators A: Physical, Vol. 118, Issue 1, pp. 144-151, 2005.
35. A. M. Cardenas-Valencia, J. Dlutowski, J. Bumgarner, C. Munoz, W. Wang, R. Popuri, and L. Langebrake, "Development of various designs of low-power MEMS valves for fluidic applications", Sensors and Actuators A: Physical, Vol. 136, Issue 1, pp. 374-384, 2007.
36. K. A. Shaikh, S. Li, and C. Liu, "Development of a Latchable Microvalve Employing a Low-Melting-Temperature Metal Alloy", Journal of Microelectromechanical Systems, Vol. 17, No. 5, pp. 1195-1203, 2008
37. T. Watanabe and H. Kuwano, "A microvalve matrix using piezoelectric actuators", Microsystem Technologies, Vol. 3, No. 3, pp. 107-111, 1997.
38. I. Charkraborty, W. C. Tang, D. P. Bame, and T. K. Tang, "MEMS micro-valve for space applications", Sensors and Actuators A: Physical, Vol. 83, Issue 1-3, pp. 188-193, 2000.
39. D. C. Roberts, N. W. Hagood, Y.-H. Su, H. Li, and J. A. Carretero, "Design of a Piezoelectrically-Driven Hydraulic Amplification Microvalve for High Pressure, High Frequency Applications", Smart Structures and Materials 2000: Smart Structures and Integrated Systems, Vol. 3985, pp. 615-628, 2000.
40. D. C. Roberts, O. Yaglioglu, J. Carretero, Y.-H. Su, L. Saggere, N. W. Hagood, "Modeling, Design, and Simulation of a Piezoelectrically Driven Microvalve for High Pressure, High Frequency Applications", Smart Structures and Materials 2001: Smart Structures and Integrated Systems, Vol. 4327, pp. 366-380, 2001.
41. J. L. Steyn, H. Q. Li, D. C. Roberts, K. T. Turner, O. Yaglioglu, Y.-H. Su, M. A. Schmidt, S. M. Spearing, and N. W. Hagood, "Hydraulic amplification devices for microscale actuation", Solid-State Sensors, Actuators and Microsystems, pp. 50-53, 2002.

42. H. Ernst, M. Willmann, T. Goettsche, J. Kohnle, H. Sandmaier, and R. Zengerle, “Microvalves for implantable microdosage systems”, Proceedings of the Second Joint EMBSBMES Conference, pp. 1840-1841, 2002.
43. E.-H. Yang and C. Lee, “Piezoelectrically Actuated Microvalves for Micropropulsion Applications”, Proceedings of 2002 ASME International Mechanical Engineering Congress and Exposition, pp. 449-453, 2002.
44. D. C. Roberts, H. Li, J. L. Steyn, O. Yaglioglu, S. M. Spearing, M. A. Schmidt, and N. W. Hagood, “A piezoelectric microvalve for compact, high-frequency, high-differential pressure micropumping systems”, Journal of Microelectromechanical Systems, Vol. 12, No. 1, pp. 81-92, 2003.
45. R. Duggirala, I.-S. Son, and A. Lal, “A pyroelectric-piezoelectric valve for integrated microfluidics”, Transducers ’03, Solid-State Sensors, Actuators and Microsystems, Vol. 2, pp. 1554-1557, 2003.
46. N.-T. Nguyen and T.-Q. Truong, “A fully polymeric micropump with piezoelectric actuator”, Sensors and Actuators B: Chemical, Vol. 1, Issue 1, pp. 137-143, 2004.
47. H. Q. Li, D. C. Roberts, J. L. Steyn, K. T. Turner, O. Yaglioglu, N. W. Hagood, and M. A. Schmidt, “Fabrication of a high frequency piezoelectric microvalve”, Sensors and Actuators A: Physical, Vol. 111, Issue 1, pp. 51-56, 2004.
48. E.-H. Yang, C. Lee, J. Mueller, and T. George, “Leak-tight piezoelectric microvalve for high-pressure gas micropropulsion”, Journal of Microelectromechanical Systems, Vol. 13, No. 5, pp. 799-807, 2004.
49. T. Goettsche, J. Kohnle, M. Willmann, H. Ernst, S. Spieth, R. Tischler, S. Messner, R. Zengerle, and H. Sandmaier, “Novel approaches to particle tolerant valves for use in drug delivery systems”, Sensors and Actuators A: Physical, Vol. 118, Issue 1, pp. 70-77, 2005.
50. H. Zhao, K. Stanely, Q. M. J. Wu, and E. Czyzewska, “Structure and characterization of a planar normally closed bulk-micromachined piezoelectric valve for fuel cell applications”, Sensors and Actuators A: Physical, Vol. 120, Issue 1, pp. 134-141, 2005.
51. H. Kim, C. In, G. Yoon, and J. Kim, “A slim microvalve driven by PZT films”, Sensors and Actuators A: Physical, Vol. 121, Issue 1, pp. 162-171, 2005
52. P. V. M. Ramanamurthy, R. Aherns, and S. Karmalkar, “Piezoelectric microvalve”, India Journal of Pure and Applied Physics, Vol. 45, pp. 278-281, 2007.
53. J. M. Park, R. P. Taylor, A. T. Evans, T. R. Brosten, G. F. Nellis, S. A. Klein, J. R. Feller, L. Salerno, and Y. B. Gianchandani, “A piezoelectric microvalve for cryogenic applications”, Journal of Microelectromechanical Systems, Vol. 18, No. 1, pp. 1-10, 2008.
54. X. Wu, S.-H. Kim, C.-H. Ji, and M. G. Allen, “A piezoelectrically-driven high flow rate axial polymer microvalve with solid hydraulic amplification”, Micro Electro Mechanical Systems, 2008, MEMS 2008, pp. 523-526, 2008.
55. M. Sobocinski, J. Juuti, H. Jantunen, and L. Golonka, “Piezoelectric unimorph valve assembled on an LTCC substrate”, Sensors and Actuators A: Physical, Vol. 149, Issue 2, pp. 315-319, 2009.

56. J. Mueller, “A Review and Applicability Assessment of MEMS-Based Microvalve Technologies for Microspacecraft Propulsion”, Micropropulsion for Small Spacecraft, Progress in Astronautics and Aeronautics, Vol. 187, AIAA, Chap. 19, pp 449- 476, 2000.
57. A. Safari and E. K. Akdogan, *Piezoelectric and Acoustic Materials for Transducers Applications*, 1st Edition, Springer, 2010.
58. F. Mohammadi, A. L. Kholkin, B. Jadidian, and A. Safari, “High-displacement spiral piezoelectric actuators”, Applied Physics Letters, Vol. 75, Issue 16, pp. 2488-2490, 1999.
59. C. Niezrecki, D. Brei, S. Balakrishnan, and A. Moskalik, “Piezoelectric Actuation: State of the Art”, The Shock and Vibration Digest, Vol. 33, No. 4, pp. 269-280, 2001.
60. A. Dogan, J. Tressler, and R. E. Newnham, “Solid-state ceramic actuator designs”, Journal of IAAA, Vol. 39, No. 7, pp. 1354-1362, 2001.
61. K. Nasser, D. J. Leo, and H. H. Cudney, “Compact Piezohydraulic Actuation System”, Smart Structures and Materials 2000: Industrial and Commercial Applications of Smart Structures Technologies, Vol. 3991, pp. 312-322, 2000.
62. D. Brei, “Design and development of a new class of piezoelectric actuators for force improvement”, Active Materials and Smart Structures, Vol. 2427, pp.343-356, 1995.
63. A. T. Crumm and J. W. Halloran, “Fabrication of microconfigured multicomponent ceramics”, Journal of the American Ceramic Society, Vol. 81, Issue 4, pp.1053-1057, 1998.
64. T. Kakashi, T. Ohmi, N. Ohya, N. Kawahara, and T. Hattori, “A Compact and Quick-Response Dynamic Focusing Lens”, Sensors and Actuators A: Physical, Vol. 70, Issue 1-2, pp. 92-97, 1998.
65. J. W. Clement, D. Brei, and A. J. Moskalik, “Bench-top characterization of an active rotor blade flap system incorporating c-block actuators”, 39th AIAA/ASME/ASCE/AHS/ASC Structures, Struc-tural Dynamics, and Materials Conference and Exhibit, pp. 2857-2869, 1998.
66. S. Kawakita, T. Isogai, N. Ohya, and N. Kawahara, “Multi-layered piezoelectric bimorph actuator”, 1997 International Symposium on Micromechatronics and Human Science, pp. 73-78, 1997.
67. A. J. Moskalik and D. Brei, “Force-deflection behavior of piezoelectric C-block actuator arrays”, Smart Materials and Structures, Vol. 8, No. 5, pp.531-543, 1999.
68. A. J. Moskaliak and D. Brei, “Quasi-static behavior of individual c-block piezoelectric actuators”, Journal of Intelligent Material Systems and Structures, Vol. 8, No. 7, pp. 571-587, 1997.
69. J. D. Ervin and D. Brei, “Recurve piezoelectric-strian-amplifying actuator architecture”, IEEE/ASME Transactions on Mechatronics, Vol. 3, No. 4, pp. 293-301, 1998.
70. J. Jiang and E. Mockensturm, “A motion amplifier using an axially driven buckling beam: i. design and experiments”, Nonlinear Dynamics, Vol. 43, No. 4, pp. 391-409, 2006.

71. A. Dogan, J. F. Fernandez, K. Uchino, and R. E. Newnham, "The "Cymbal" electromechanical actuator", , Proceedings of the Tenth IEEE International Symposium on Applications of Ferroelectrics, Vol.1, Issue 18-21, pp.213-216, 1996.
72. A. Dogan, K. Uchino, and R. E. Newnham, "Composite piezoelectric transducer with truncated conical endcaps "cymbal"", IEEE Transactions on Ultrasonics, Ferroelectrics and Frequency Control, Vol. 44, No. 3, pp. 597-605, 1997.
73. B. J. Pokines and E. Garcia, "A smart material microamplification mechanism fabricated using LIGA", Smart Materials and Structures, Vol. 7, No. 1, pp. 105-112, 1998.
74. J.-M. Breguet, R. Perez, A. Bergander, C. Schmitt, R. Clavel, and H. Bleuler, "Piezoactuators for motion control from centimeter to nanometer", 2000 IEEE/RSJ International Conference on Intelligent Robots and Systems, Vol. 1, pp. 492-497, 2000.
75. C.-L. Sun, S. S. Guo, W. P. Li, Z. B. Xing, G. C. Liu, and X. Z. Zhao, "Displacement amplification and resonance characteristics of the cymbal transducers", Sensors and Actuators A: Physical, Vol. 121, Issue 1, pp. 213-220, 2005.
76. A. Naganawa, S. Mori, H. Tada, Y. Shibuya, G. Obinata, and K. Ouchi, "Finite element method analysis and control of micro actuator with piezoelectric element for spinstand", Microsystem Technologies, Vol. 11, No. 8-10, pp.606-611, 2005.
77. J. Juuti, K. Kordas, R. Lonnakko, V.-P. Moilanen, and S. Leppavuori, "Mechanically amplified large displacement piezoelectric actuators", Sensors and Actuators A: Physical, Vol. 120, Issue 1, pp.225-231, 2005.
78. T.-M. Lee, Y. H. Seo, K.-H. Whang, and D.-S. Choi, "Study of the lateral piezoelectric actuator with actuation range amplifying structure", Key Engineering Materials, Vols. 326-328, pp. 289-292, 2006.
79. N. J. Gonway, Z. J. Traina, and S.-G. Kim, "A strain amplifying piezoelectric MEMS actuator", Journal of Micromechanicals and Microengineering, Vol. 17, No. 4, pp. 781-787, 2007.
80. H. Zhou and B. Henson, "Analysis of a diamond-shaped mechanical amplifier for a piezo actuator", The International Journal of Advanced Manufacturing Technology, Vol. 32, No. 1-2, pp. 1-7, 2007.
81. Y. Sugawara, K. Onitsuka, S. Yoshikawa, Q. Xu, R. E. Newnham, and K. Uchino, "Metal-ceramic composite actuators", Journal of the American Ceramic Society, Vol. 75, Issue 4, pp. 996-998, 1992
82. K. Onitsuka, A. Dogan, J. F. Tressler, Q. Xu, S. Yoshikawa, and R. E. Newnham, "Metal-ceramic composite transducer, the "Moonie"", Journal of Intelligent Material Systems and Structures, Vol. 6, No. 4, pp.447-455, 1995.
83. J. Garcia-Bonito, M. J. Brennan, S. J. Elliott, A. David, and R. J. Pinnington, "A novel high displacement piezoelectric actuator for active vibration control", Smart Materials and Structures, Vol. 7, No. 1, pp. 31-42, 1998.
84. W. P. Robbins, D. L. Polla, and D. E. Glumac, "High-displacement piezoelectric actuator utilizing a meander-line geometry- part I: experimental characterization", IEEE

Transactions on Ultrasonics Ferroelectrics and Frequency Contorl, Vol. 38, No. 5, pp.454-460, 1991.

85. D. K. Samak and I. Chopra, “Design of high force, high displacement actuators for helicopter rotors”, Smart Structures and Materials, Vol. 5, No. 1, pp. 58-67, 1996.
86. R. Le Letty, F. Claeyysen, N. Lhermet, and P. Bouchilloux, “A New Amplified Piezoelectric Actuator for Precise Positioning and Active damping”, Proc. SPIE Vol. 3041, p. 496-504, SmartStructures and Materials 1997: Smart Structures and Integrated Systems, 1997.
87. R. Chandra and I. Chopra, “Actuation of Trailing Edge Flap in a Wing Model Using a Piezostack Device”, Journal of Intelligent Material Systems and Structures, Vol. 11, No. 5, pp.328-342, 2000.
88. C. C. M. Wu, D. Lewis, and S.-E. E. Park, “High authority telescoping actuators with single crystal piezoelectric materials”, Smart Structures and Materials 2000: Industrial and Commercial Applications of Smart Structures Technologies, Vol. 3991, pp. 304-311, 2000.
89. P. W. Alexander, D. Brei, W. Miao, J. W. Halloran, R. L. Gentilman, G. E. Schmidt, P. T. McGuire, and J. R. Hollenbeck, “Fabrication and experimental characterization of $d_{31}$ telescopic piezoelectric actuators”, Journal of Materials Science, Vol. 36, No. 17, pp. 4231-4237, 2001.
90. Y. H. Seo, D.-S. Choi, J.-H. Lee, T.-J. Je, and K.-H. Whang, “Laterally driven thin film PZT actuator with high-aspect-ratio silicon beam for stroke amplification”, Sensors and Actuators A: Physical, Vol. 127, Issue 2, pp. 302-309, 2006.
91. X. Jiang, W. B. Cook, and W. S. Hackenberger, “Cryogenic Piezoelectric Actuator”, Astronomical and Space Optical Systems, Proceedings of the SPIE, Vol. 7439, pp. 74390Z, 2009.
92. S. Egusa and N. Iwasawa, “Poling characteristics of PZT/epoxy piezoelectric paints”, Ferroelectrics, Vol. 145, Issue 1, pp. 45-60, 1993.
93. Y. Takahiro, K. Masako, and S. Norikazu, “Influence of poling conditions on the piezoelectric properties of PZT ceramics”, Journal of Material Science: Materials Electronics, Vol. 11, No. 5, pp. 425-428, 2000.
94. T. M. Kamel and G. de With, “Poling of hard ferroelectric PZT ceramics”, Journal of the European Ceramic Society, Vol. 28, Issue 9, pp. 1827-1838, 2008.
95. Q. M. Zhang, J. Zhao, K. Uchino, and J. Zheng, “Change of the weak-field properties of $Pb(ZrTi)O_3$ piezoceramics with compressive uniaxial stresses and its links to the effect of dopants on the stability of the polarizations in the materials”, Journal of Materials Research, Vol. 12, No. 1, pp.226-234, 1997.
96. D. Fang and C. Li, “Nonlinear electric-mechanical behavior of a soft PZT-51 ferroelectric ceramic”, Journal of Material Science, Vol. 34, No. 16, pp.4001-4010, 1999.

97. C.-Y. Lin and N. W. Hagood, “Compressive depolarization of PZT piezoelectric materials under high electromehanical driving levels”, In Smart Structure and Materials 2000: Active Materials: Behavior and Mechanics, Vol. 3992, pp. 114-125, 2000.
98. T. Liu and C. S. Lynch, “Orientation dependence of nonlinearity and hysteresis in PZN-4.5%PT single crystals II: bipolar electromechanical response”, Journal of intelligent Material Systems and Structures, Vol. 17, No.11, pp.953-957, 2006.
99. M. J. Sinclair, “A High Force Low Area MEMS Thermal Actuator”, Inter Society Conference on Thermal Phenomena, 2000.
100. K. G. McConnell and P. S. Varoto, *Vibration Testing: Theory and Practice*, Wiley-Interscience, pp. 140-150, 1995.
101. G. Piazza, P.J. Stephanou, J.P. Black, R.M. White and A. P. Pisano, "Single-Chip Multiple-Frequency RF Microresonators based on Contour-Mode and FBAR Technologies," 2005 IEEE Ultrasonic Symposium, Rotterdam, Issue.18-21, pp. 1187-1190, 2005.
102. G. F. Iriarte, F. Engelmark, and I. V. Katardjiev, “Reactive sputter deposition of highly oriented AlN film at room temperature”, Journal of Materials Research, Vol. 17, Issue 6, pp. 1469-1475,2002
103. G. F. Iriarte, F. Engelmark, M. Ottosson, and I. V. Katardjiev, “Influence of deposition parameters on the stress of magnetron sputter-deposited AlN thin films on Si(100) substrate”, Vol. 18, Isssue 2, pp.423-432, 2003
104. Q. X. Guo, K. Yahata, T. Tanaka, M. Nishio, and H. Ogawa, “Low-temperature growth of aluminum on sapphire substrates”, Journal of Crystal Growth, Vol. 257, Issue 1-2, pp. 123-128, 2003
105. S.-H. Lee, K. H. Yoon, D.-S. Cheong, and J.-K. Lee, “Relationship between residual stress and structural properties of AlN films deposited by r.f. reactive sputtering”, Thin Solid Films, Vol. 435, Issue 1-2, pp. 193-198, 2003.
106. C.-L. Huang, K-W. Tay, and L. Wu, “Aluminum nitride films deposited under various sputtering parameters on molybdenum electrodes”, Solid-State Electronics, Vol. 49, Issue 2, pp. 219-225, 2005.
107. W.-K. Liu, K.-W. Tay, S.-C. Kuo, and M.-J. Wu, “Fabrication of piezoelectric AlN thin film for FBARS”, Science in China Series G: Physics Mechanics and Astronomy, Vol. 52, No. 2, pp. 226-232, 2009.
108. V. V. Feimetsger, P. N. Laptev, and S. M. Tanner, “Innovative technique for tailoring intrinsic stress in reactively sputtered piezoelectric aluminum nitride films”, Journal of Vacuum Science & Technology A, Vol. 27, Issue 3, pp. 417-422, 2009.
109. S. Mehta and G. Sharma, “A single-pass, in-situ planarization process utilizing TEOS for double-poly, double-metal CMOS technologies”, 1989 VMIC conference, pp. 80 – pp. 88, 1989.
110. G. B. Raupp and T. S. Cale, “Step Coverage Prediction in Low-Pressure Chemical Vapor Deposition”, Chemistry of Materials 1989, *1* (2), pp 207–214.

111. D. Yu, D. Favreau, E. Martin, and A. Manocha, “Step coverage study of PETEOS Deposition for Intermetal Dielectric Applications”, VLSI Multilevel Interconnection Conference, pp. 166 – pp. 172, 1990.
112. C. Chang, T. Abe, and M. Esashi, “Trench filling characteristics of low stress/TEOS/ozone oxide deposited by PECVD and SACVD”, Microsystem Technologies, Vol. 10, Issue 2, pp. 97 – pp. 102, 2004.
113. C. E. Viana, N. I. Morimoto, and O. Bonnaud, “Annealing effects in the PECVD $SiO_2$ thin films deposited using TEOS, Ar and $O_2$ mixture”, Microelectronics Reliability, Vol. 40, Issue 4-5, pp. 613-616, 2000.
114. V. V. Felmetsger and P. N. Laptev, “AC reactive sputtering of highly c-axis oriented AlN films for electro-acoustic devices”, Tegal Corporation.
115. T. Kamohara, M. Akiyama, N. Ueno, K. Nonaka, and H. Tateyama, “Growth of highly c-axis-oriented aluminum nitride thin films on molybdenum electrodes using aluminum nitride interlayers”, Journal of Crystal Growth, Vol. 275, Isu. 3-4, pp. 383-388, 2005.
116. T. Kamohara, M. Akiyama,N. Ueno, K. Nonaka, and N. Kuwano, "Local epitaxial growth of aluminum nitride and molybdenum thin films in fiber texture using aluminum nitride interlayer", Applied Physics Letters, Vol. 89, Issue 7, 2006
117. K.–W. Tay, C.-L. Huang, and L. Wu, “Highly c-axis oriented thin AlN films deposited on gold seed layer for FBAR devices”, Journal of Vacuum Science & Technology B: Microelectronics and Nanometer Structures, Vol. 23, Issue 4, pp. 1474-1479, 2009
118. R. S. Naik, R. Reif, J. J. Lutsky, and C. G. Sodini, "Low-Temperature Deposition of Highly Textured Aluminum Nitride by Direct Current Magnetron Sputtering for Applications in Thin-Film Resonators", Journal of Vacuum Science & Technology A, Vol. 149, Is. 2, pp. 691-696, 1999.
119. H.-C. Lee, J.-Y. Park, K.-H. Lee, and J.-U. Bu, "Preparation of highly textured Mo and AlN films using a Ti seed layer for integrated high-Q film bulk acoustic resonators", Journal of Vacuum Science & Technology B: Microelectronics and Nanometer Structures, Vol. 22, Issue. 3, pp. 1127-1133, 2004
120. T. Riekkinen , A. Nurmela, J. Molarius, T. Pensala, P. Kostamo, M. Ylilammi, S. van Dijken, "Influence of the seed layer on structural and electro-acoustic properties of sputter deposited AlN resonators", Thin Solid Films, Vol. 517, Issue 24, pp. 6588-6592, 2009
121. M. Akiyama, N. Ueno, H. Tateyama, K. Nagao, and T. Yamada, "Preparation of highly oriented aluminum nitride thin films on molybdenum bottom electrodes using metal interlayers", Journal of Materials Science, Vol. 40, No. 5, pp. 1159-1162, 2005
122. C.-L. Wei, Y.-C. Chen, C.-C. Cheng, and K.-S. Kao, "Solidly mounted resonators consisting of a molybdenum and titanium Bragg reflector", Applied Physics A: Materials Science & Processing, Vol. 90, No. 3, pp. 501-506, 2008

123. H. Khatri and S. Marshillac, “The effect of deposition parameters on radiofrequency sputtering molybdenum thin films”, Journal of Physics: Condensed Matter, Vol. 20, No. 5, pp. 1-5, 2008.
124. A. O. Ong and F. E. H. Tay, “Motion Characterizations of Lateral Micromachined Sensor Based on Stroboscopic Measurements”, IEEE Sensor Journal, Vol. 7, No. 2, pp. 163-171, 2007.
125. http://www.testing-expo.com/europe/05txeu_conf/pres/steger.pdf